Interfacial Magnetic Phenomena and Topotactic Phase Transformations in Perovskite Oxide Thin Film

By

MINGZHEN FENG

DISSERTATION

Submitted in partial satisfaction of the requirements for the degree of

DOCTOR OF PHILOSOPHY

in

Materials Science & Engineering

in the

OFFICE OF GRADUATE STUDIES

of the

UNIVERSITY OF CALIFORNIA

DAVIS

Approved:

Yayoi Takamura, Chair

Roopali Kukreja

Seung Sae Hong

Committee in Charge

2023

Interfacial Magnetic Phenomena and Topotactic Phase Transformation in Perovskite Oxide Thin Film

ABSTRACT

Perovskite oxides, with the ABO_3 structure where the A cations are typically alkaline earth or rare earth elements and B cations are transition metals, have attracted significant attention due to their potential applications in spintronics, magnetic devices, and neuromorphic computing. These materials exhibit a wide range of functional properties, including ferromagnetism, metal-to-insulator transitions, and controllable phase transformations, which arise from the intricate interplay of spin, charge, lattice, and orbital degrees of freedom. Importantly, perovskite oxides demonstrate a remarkable sensitivity to external stimuli such as external magnetic fields, lattice strain, and ion migrations, allowing for precise control over their emerging magnetic and electronic properties. This characteristic distinguishes them from metallic systems, offering unique path for the design and manipulation of functional materials with tailored properties. As a result, perovskite oxides hold great promise for the development of advanced electronic and magnetic devices with enhanced performance and functionality.

Controlling interfacial magnetic phenomena between hard and soft ferromagnetic (FM) layers in heterostructures plays a key role in next generation spintronic and magnetic memory devices. In this dissertation, the tuning of interfacial properties through control of the thin film strain and layer thickness in $La_{2/3}Sr_{1/3}CoO_3$ (LSCO)/ $La_{2/3}Sr_{1/3}MnO_3$ (LSMO) bilayers are discussed. Soft x-ray magnetic spectroscopy was performed to study the valence states and bonding configurations of the transition metal ions as well as the magnetic exchange coupling of the bilayers. Magnetocrystalline anisotropy and exchange bias were further explored in

LSCO/LSMO bilayers grown on $NdGaO_3$ substrates, where soft x-ray linear dichroism spectra highlighted the differing electron occupancy along the two in-plane directions of the LSMO layer with increasing LSCO layer thickness.

Investigating the potential of ion migration-induced alteration on functional properties has become a prominent research focus in the rapidly evolving field of neuromorphic computing. Perovskite oxides, including cobaltites (LSCO), manganites (LSMO), and ferrites ($La_{0.7}Sr_{0.3}FeO_3$, LSFO), have emerged as prime candidates for their remarkable characteristics, such as high oxygen vacancy conductivity, relatively low oxygen vacancy formation energy, and the strong interplay between magnetic and electronic properties with oxygen stoichiometry. This dissertation delves into the evolution of physical properties exhibited by LSCO, LSMO, and LSFO thin films when subjected to highly reducing environments, specifically H_2 and vacuum conditions. In the cobaltite systems, the introduction of H_2 leads to the formation of oxygen-deficient phases at lower temperatures compared to vacuum annealing but remain in the perovskite phase without phase transitions at higher hydrogenation temperatures. The manganites, on the other hand, require more reduced conditions under vacuum annealing to achieve a mixed phase of brownmillerite and Ruddlesden-Popper phases. Notably, the ferrite films maintain their oxygen-deficient perovskite phase even when subjected to the most reducing conditions but shows significant differences in their electronic properties. The strong correlation between crystal structure and the magnetic/electronic properties underscores the potential of leveraging ion migration as a foundation for emerging applications such as neuromorphic computing.

ACKNOWLEDGEMENTS

I would like to express my profound gratitude to my advisor, Dr. Yayoi Takamura, for her unwavering support, guidance, and mentorship throughout my Ph.D. research journey. Dr. Takamura has been a responsible, kind, and approachable mentor who not only supervised my research project but also always ready to offer valuable suggestions and assistance. When I arrived at UC Davis with limited scientific writing skills and the ability to present my research to the public, she offered valuable suggestions in refining my manuscript, enhancing the logical flow, and improving the clarity of my work. Her mentorship has greatly boosted my confidence in presenting my research at the Qualifying Exam (QE) and conferences, as well as in honing my scientific writing skills. The pandemic was a challenging period for all of us, with campus closures and the imposition of shelter-in-place orders. Dr. Yayoi Takamura extended tremendous support to me on research progress and daily life, with genuine concern for our physical and mental well-being.

I extend my sincere appreciation to Dr. Roopali Kukreja and Dr. Seung Sae Hong for their vital roles as members of my QE and dissertation committees. Their invaluable guidance and input significantly contributed to the success of each of my research projects. Furthermore, I am grateful for their training and guidance regarding the use of laboratory equipment. I also had the privilege of engaging in fruitful collaborations with students from their respective research groups, including Rahul Jangid, Jugal Mehta, Scott Smith (from Dr. Roopali Kukreja's group), and Jieyang Zhou (from Dr. Seung Sae Hong's group).

During my four and a half years as a member of the Takamura Research Group (TRG), internal collaborations and friendships are essential in my Ph.D. journey. I wish to express my heartfelt thanks to all current and former TRG members for their invaluable help and enlightening discussions during my time at UC Davis. Dr. Alex Kane, with his wealth of experience, provided me with training in PLD and consistently offered guidance on data analysis. Nolan Ahlm's expertise in Python coding provided me with efficient methods for analyzing beamline data. Dr. I-Ting Chiu, not only a dependable lab mate but also one of my closest friends at UC Davis, played a significant part in introducing me to equipment operation and data analysis procedures. She patiently answered my questions and added a fun element to our shared experiences, including our travels to National Parks and Alaska. I am grateful to Dayne Sasaki for being an excellent companion during beamtime shifts, initiating interesting conversations that made night shifts much fun, and for his expertise in handling Bruker and computer hardware issues. Ishmam Nihal and Hudson Shih consistently posed insightful questions and provided fresh perspectives, which greatly enriched my understanding of the concepts learned during my time at Davis. I also extend my appreciation to the other TRG members I collaborated with: Tanaya Sahoo, Asrafuzzaman, Ryan Fillhouer, and Andrew Layton.

In addition to my colleagues, I am indebted to the talented staff scientists at national labs with whom I had the privilege to collaborate. The research projects in this dissertation cannot be completed properly without their guidance and help in beamline set up and data analyzing. I extend my gratitude to Dr. Padraic Shafer, Dr. Alpha N'Diaye, Dr. Christoph Klewe at the Advanced Light Source, and Dr. Apurva Mehta at the Stanford Synchrotron Radiation Lightsource.

I would like to acknowledge the exceptional collaborators I have worked with, including Junjie Li, Dr. Ivan Schuller, Dr. Shenli Zhang, Dr. Giulia Galli, Dr. Alexandre Pofelski, and Dr. Yimei Zhu, all of whom contributed significantly to the projects in Quantum Materials for Energy Efficient Neuromorphic Computing (Q-MEEN-C), an Energy Frontier Research Center funded by the U.S. Department of Energy (DOE).

I am also grateful to my friends at UC Davis: Jieyang Zhou, I-Ting Chiu, Peifen Lyu, Yunju Chang, and Zhongrui Liu, for their companionship throughout my time at Davis. Lastly, I am at a loss for words to fully convey my deep gratitude to my parents, Lifang Lu and Jianqiang Feng. Their enduring love, unwavering guidance, and generous financial support have been the bedrock upon which I built my path toward this degree.

Table of Contents

Chapter 1

Introduction

1.1 Perovskite Oxides

Complex oxides, a class of materials with diverse functional properties such as ferromagnetism [1,2], controllable phase transformation [3,4], metal-to-insulator transitions [5–7] and superconducting [8,9]. These properties arise from the interplay of spin, charge, lattice, and orbital degrees of freedom, making complex oxides highly responsive to external stimuli compared to metallic systems. Perovskite oxides, a subset of complex oxides, exhibit a wide range of functional properties and have attracted significant interest. Thin film deposition techniques have enabled the fabrication of perovskite thin films and heterostructures with atomic precision [10,11], allowing for the exploration of unique interfacial behaviors which are absent from the constituent materials. Perovskite oxide thin films hold promise for applications in memory/logic devices [12,13], neuromorphic computing [14,15], and spintronics [16,17]. The study of perovskite thin films not only contributes to fundamental physics research but also offers potential for practical device applications.

1.1.1 Perovskite structures

Perovskite oxides are a class of materials where the crystalline structure plays a critical role in determining their properties. Minor changes in stoichiometry or atomic arrangement can lead to the emergence or suppression to functional properties. The typical chemical formula for

perovskite oxides is ABO_3. The idealized unit cell is cubic as shown in **Figure 1.1(a)**, with A-cations (usually alkaline earth or rare earth elements) occupying corners of the cubic, B-cations (usually transition metals) residing in the body center, and oxygen ions filling the face centers of the cubic unit cell.

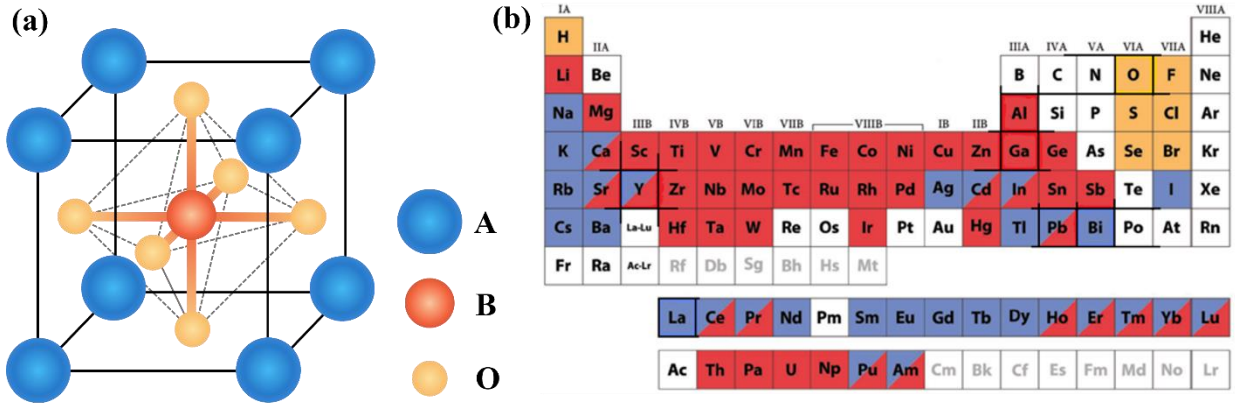

Figure 1.1 (a). Idealized perovskite oxide crystal structure with chemical formula ABO_3. (b). The periodic table [18] with marked elements that can be accommodated into perovskite oxide structure. Elements marked in blue can be substituted at the A-site, red can be incorporated at the B-site, orange can occupy the face center positions within the structure.

The relationship between cation size and crystal structure in perovskites is indicated by the Goldschmidt tolerance factor (*t*), as shown in **Eqn. (1.1)** [19], where r_A, r_B and r_O refer to the ionic radii of A, B, and O ions, respectively. The ideal cubic structure of perovskites requires proper relative sizes of the A- and B-site cations. When the ratio between A-O bonds and B-O bonds changes, structural distortions can occur, which include octahedral tilting, unit cell size changing, and the formation of non-cubic crystal symmetries [20].

$$t = \frac{r_A + r_O}{\sqrt{2}\,(r_B + r_O)} \tag{1.1}$$

Table 1.1 summarizes the relationship between the Goldschmidt tolerance factors (*t*) and the corresponding crystal structures. The preservation of the perovskite structure relies on careful selection of A- and B-site cations. Furthermore, the octahedral rotations can be precisely manipulated by choosing appropriate cations for incorporation at the A and B sites. These rotations impact the bond angles and lengths, influencing the degree of overlap between the electron clouds of transition metal *3d* orbitals and oxygen *2p* orbitals, leading to different occupancy of energy states. Additionally, the substitution or doping of A-site cations allows for the tuning of the valence state of B-cations, which introduces potential charge transfers and significantly influences the functional properties of perovskite materials. The control through chemical substitutions on the A- and B-sites as well as oxygen stoichiometry provides extensive freedom to modify phase/structure of the materials, thus influencing the functional properties of perovskite oxides [21,22].

Table 1.1 Goldschmidt tolerance factors (*t*) and the corresponding crystal structures.

Goldschmidt Tolerance Factor (*t*)	**Crystal Structure**
$t < 0.7$	Trigonal or Non-perovskite
$0.7 \leq t < 0.9$	Orthorhombic or Rhombohedral
$0.9 \leq t \leq 1$	Cubic
$t > 1$	Hexagonal or Tetragonal

The periodic table in **Figure 1.1(b)** shows the wide range of different elements that can be hosted on each lattice site, including the substitution of chalcogens and halogens for oxygen, though in this research we focus on oxide-based compounds. Due to the fact that different ions exist in the

perovskite structure, the stability and symmetry of the perovskite lattice are influenced not only by the sizes of the cations and anions but also by the attractive and repulsive forces between them. Therefore, the interactions between charge, orbital, spin, and lattice degrees of freedom, along with the ability to host a wide range of elements, contribute to the rich behavior of perovskite oxides.

1.1.2 Crystal Field Splitting

In the perovskite structure, the oxygen ions form an octahedral coordination around the central transition metal ion. The transition metal ion typically has partially filled 3*d* orbitals, which are responsible for its magnetic behavior. In a perfect spherical field, these 3*d* orbitals would be degenerate - they have the same energy level as shown in **Figure 1.2**. However, the presence of surrounding oxygen ions breaks this degeneracy. The 3*d* orbitals of the transition metal ion can be divided into two sets: the e_g orbitals and the t_{2g} orbitals. The e_g orbitals consist of d_{z^2} and $d_{x^2-y^2}$ orbitals, which have lobes aligned along the crystallographic axes as shown in **Figure 1.3**. The energy of d_{z^2} and $d_{x^2-y^2}$ orbitals is raised due to the stronger interactions with the oxygen's *2p* orbitals. On the other hand, the t_{2g} orbitals (d_{xy}, d_{yz}, and d_{xz}) have lobes aligned at 45 degrees to the crystallographic axes and have weaker interactions with oxygen *2p* orbitals, leading to lower energy levels compared to the e_g orbitals.

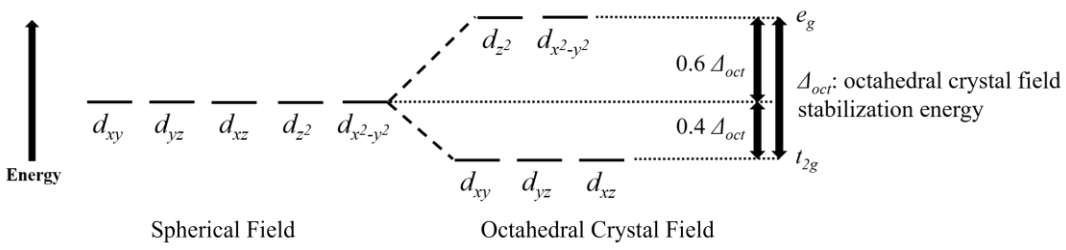

Figure 1.2 Crystal field splitting of the transition metal ion in perovskite oxides.

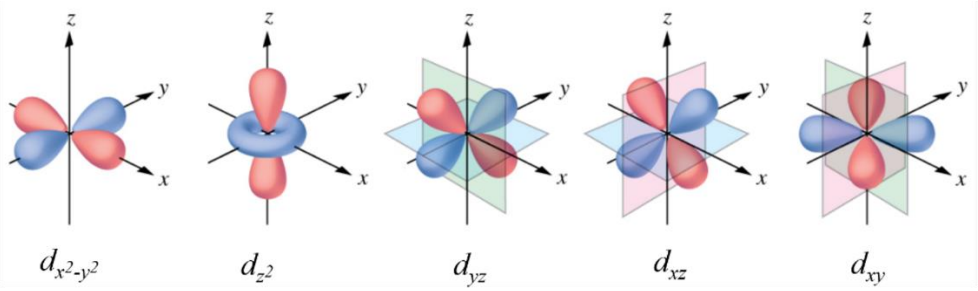

Figure 1.3 *3d* orbital electron distributions.

The energy difference between the e_g and t_{2g} orbitals results in the crystal field splitting and it's presented by octahedral crystal field stabilization energy (CFSE, Δ_{oct}) as shown in **Figure 1.2**. The magnitude of this splitting is affected by various factors, such as the nature of the transition metal ions, the strength of the ligand-field (how closely the oxygen ions are coordinated to the metal), and the ionic radii of the metal and oxygen ions. In turn, this crystal field splitting influences the electronic and magnetic properties of the perovskite oxide [23,24]. When electrons occupy the orbitals in ascending order of energy, different spin states can arise, namely high-spin, intermediate-spin, or low-spin states, depending on the interplay between the CFSE and the spin/Hund's pairing energy (which represents the energy cost of placing a second electron into a half-filled d-orbital). In a high-spin configuration, where CFSE is relatively low compared to the spin pairing energy, electrons preferentially occupy the t_{2g} and e_g orbitals before pairing with the other spin. The unpaired electrons result in a high magnetic moment and potential ferromagnetic (FM) behavior. In contrast, in a low-spin configuration, where CFSE is larger than spin pairing energy, all the t_{2g} orbitals will be filled with up and down spin electrons first before filling the e_g orbitals, leading to fewer unpaired electrons and a lower magnetic moment.

Factors such as epitaxial strain and Jahn-Teller distortion could affect the crystal field splitting [25,26]. When a perovskite oxide thin film has the lattice mismatch to the substrate material, the thin film experiences epitaxial strain, the relative positions of the transition metal ion and oxygen ions may change, altering the local symmetry around the transition metal ion. This change in symmetry can lead to modifications in the crystal field splitting. For instance, compressive strain in the *xy* plane would decrease the metal-oxygen bond distances in the *x* and *y* directions, increasing the electrostatic interactions between the *3d* orbitals of the transition metal ion and the oxygen *2p* orbitals. As a result, $d_{x^2-y^2}$ has higher energy than the d_{z^2} orbital. Similarly, d_{xy} has higher energy relative to the d_{xz} and d_{yz} orbitals. In contrast, tensile strain in the *xy* plane can have the opposite effect, resulting higher energy of the d_{z^2} orbital.

The Jahn-Teller distortion is commonly observed in transition metal ions with partially filled *d*-orbitals (with the configurations high-spin $3d^4$, low-spin $3d^7$ or $3d^9$) in perovskite oxides. For example, in $LaMnO_3$ where Mn^{3+} is in $3d^4$ electron configuration [27]. The electron in the e_g energy level can either occupy the $d_{x^2-y^2}$ or d_{z^2} orbital. Therefore, the Mn^{3+} ions can be considered to be Jahn-Teller active due to the equal-energy filling possibilities. In this case, a spontaneous distortion could occur to lower the energy of one set of degenerate orbitals while raising the energy of the other set, resulting in a stabilization of the system.

1.1.3 Magnetism in Perovskites

Ferromagnetism in metallic materials arises from quantum mechanical exchange interactions between neighboring atoms [28]. The electron occupancy obeys Fermi-Dirac statistics, where the Coulomb repulsion is stronger when electrons have larger spatial overlap or occupy the same

orbital. Additionally, the Pauli exclusion principle dictates that electrons in the same orbital must have opposite spins. By combining these principles, aligning electron spins in a parallel manner minimizes electrostatic energy. This arrangement prevents electrons from sharing the same orbital, also increasing the distance between electron distributions, thus reducing repulsion. The direct exchange mechanism explains how electrons interact magnetically between adjacent metallic atoms. However, as the strength of the direct exchange interactions decreases exponentially as a function of the atomic distance, it cannot explain the magnetism arising from the transition metal ions in perovskite oxides due to the larger distance between adjacent B cations. The intermediary oxygen ions further prevent the direct interactions between the neighboring B-site ions. As a result, the magnetism in perovskites was explained by *indirect* exchange mechanisms: Goodenough – Kanamori – Anderson rules, where the FM and antiferromagnetic (AFM) properties are determined by the orbital filling of the two transition metal cations between the B - O - B covalent bonds. Based on the type of the interactions, double exchange and super-exchange are discussed below:

A. Double exchange

The double exchange mechanism [29] is a fundamental process that elucidates the FM behavior observed in perovskite oxides. As shown in **Figure 1.4** [30], this mechanism involves the interaction between the $3d_{z^2}$ orbitals of a high spin Mn^{3+} ($3d^4$) ion and a Mn^{4+} ($3d^3$) ion via the $2p_z$ orbital of an O^{2-} ion. During this process, an electron from the oxygen $2p$ orbital hops into an unoccupied e_g orbital of the neighboring Mn^{4+} ion, while the corresponding hole in the oxygen $2p$ orbital is filled by an electron from the Mn^{3+} e_g orbital. As a result, the parallel alignment of spins in the Mn ions results in the emergence of ferromagnetism. This alignment

also leads to a reduction in overall energy by minimizing the electrostatic repulsion between Mn and oxygen orbitals. Furthermore, the electron hopping between neighboring ions not only confers metallic conducting behavior to the thin film but also instigates the metal-to-insulator transition (MIT) at the Curie temperature (T_c). The interplay of double exchange and hopping dynamics gives rise to the intriguing magnetic and conducting properties exhibited by perovskite oxide systems.

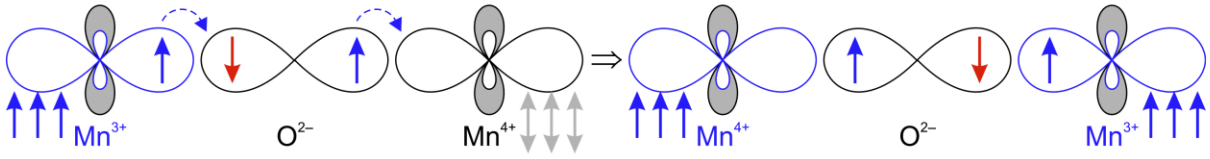

Figure 1.4 FM double exchange between the 3*d* orbitals of adjacent Mn^{3+} and Mn^{4+} cations via the $2p_z$ orbital of an O^{2-} ion.

B. *Super-exchange*

Super-exchange is a significant type of exchange interaction in perovskite oxides, leading to either FM or AFM properties. An instance of FM superexchange interactions is depicted in **Figure 1.5** (a), where the partially filled e_g orbitals of high spin Co^{2+} ($3d^7$) and Mn^{4+} ($3d^3$) ions in a double perovskite La_2CoMnO_6 are involved [31]. To satisfy the Pauli Exclusion Principle, an electron with down spin from the oxygen 2*p* orbital pairs with an electron with up spin from the e_g orbital of Co^{2+} ions, leaving the electron with up spin in O^{2-} to bond with the Mn^{4+} ion.

Another scenario involves super-exchange interactions is between identical ions, exemplified by high spin Fe^{3+} ($3d^5$) ions with 180° bond angle in $LaFeO_3$ (see **Figure 1.5** (b)). In this case, the

oxygen spins align antiparallel to both Fe ions, whose orbitals are all half-filled, resulting in an antiparallel alignment between adjacent Fe ions. A notable outcome of super-exchange interactions is the localization of electrons due to the partial covalent nature of the bonds between the metal cations and oxygen anion instead of the real electron hopping process in double exchange. Therefore, the 180º exchange between two half-filled or two empty orbitals is usually AFM and insulating [30].

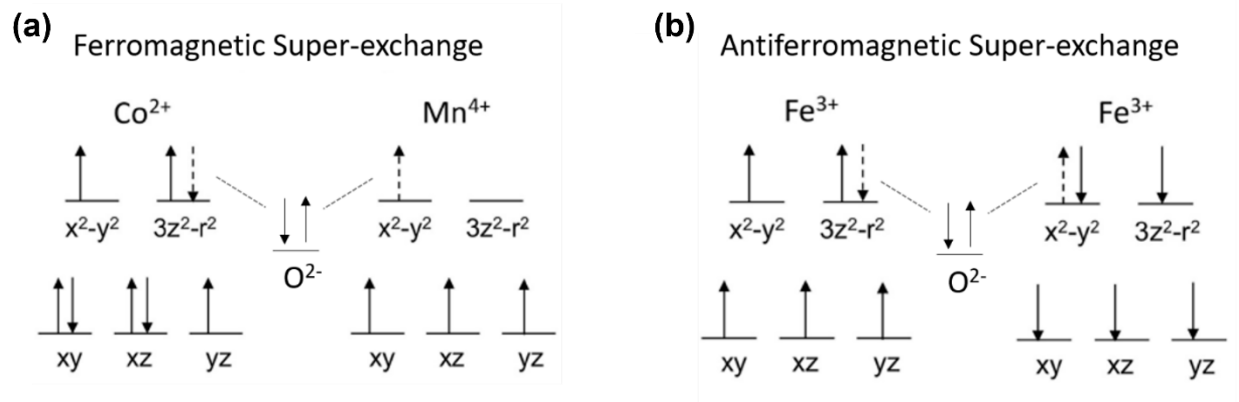

Figure 1.5 (a). FM super-exchange between the 3*d* orbitals of adjacent Co^{2+} and Mn^{4+} cations (b). AFM super-exchange between the 3*d* orbitals of adjacent Fe^{3+} cations with 180º Fe-O-Fe bond angle.

Such double exchange and super-exchange interactions, mediated by the oxygen ions, play a vital role in determining the magnetic properties of perovskite oxides, and their understanding is essential for advancing applications in magnetic and spintronic devices.

1.1.4 $La_{1-x}Sr_xCoO_3$

$La_{1-x}Sr_xCoO_3$ has attracted significant attention in the field of novel memory applications, next-generation ionic devices, and solid oxide fuel cells [32–35]. It is formed by substituting

strontium (Sr) for lanthanum (La) in the perovskite structure of $LaCoO_3$. The varying Sr composition, denoted by 'x', allows for the tuning of its magnetic and electronic properties, making it a versatile material with potential applications in various fields.

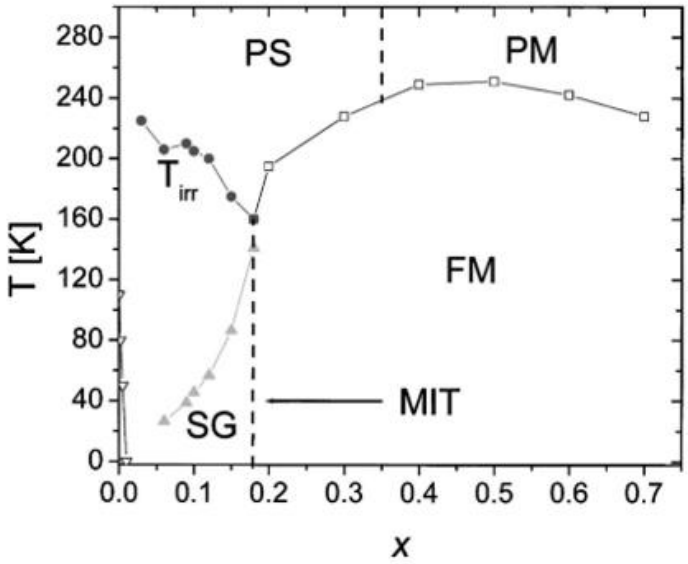

Figure 1.6 Phase diagram of bulk $La_{1-x}Sr_xCoO_3$ [2]. Notation on the plot: SG: spin glass; PS: paramagnetic semiconductor; PM: paramagnetic metal; FM: ferromagnetic metal; MIT: metal-to-insulator transition; T_{irr}: irreversibility temperature.

Figure 1.6 presents the phase diagram of bulk $La_{1-x}Sr_xCoO_3$ [2], where the parameter x denotes the doping concentration of Sr ions. T_{irr} is the irreversibility temperature, representing the temperature at which the deviation occurs between the zero field-cooled (ZFC) and field-cooled (FC) magnetization vs. temperature (M vs. T) curves. The metal-to-insulator transition (MIT) is observed at the Sr doping level of x = 0.18. A specific region known as the spin-glass (SG) regime emerges for x values below 0.18, characterized by the occurrence of magnetoelectronic phase separation (MEPS). This MEPS phenomenon results in the formation of small FM clusters

within an AFM insulating matrix [35]. As x increases beyond 0.18, the FM clusters gradually grow, ultimately leading to the formation of a percolation network and the long-range FM/metallic behavior [36,37]. The FM clusters are attributed to the double exchange interactions between Co^{3+}- O - Co^{4+} ions, whereas the AFM matrix arises from the super-exchange interactions of Co^{3+}- O - Co^{3+} and Co^{4+}- O - Co^{4+} ions [2]. Moreover, it has been discovered that the MEPS phenomena persist in $La_{1-x}Sr_xCoO_3$ thin films with x > 0.18 when the film thickness is below a critical threshold [38]. In this dissertation, the focus was on $La_{1-x}Sr_xCoO_3$ with x = 1/3 due to its FM properties observed below T_c of approximately 240 K.

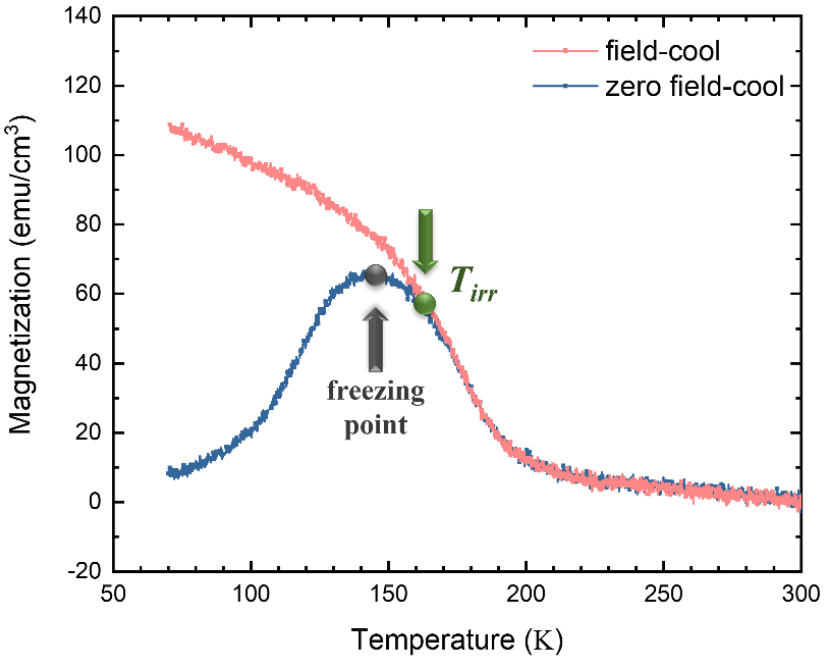

Figure 1.7 Field-cooled (pink) and zero field-cooled (blue) magnetization vs. temperature curves of a 12 nm thick LSCO thin film grown on a LAO substrate. Freezing temperature (grey) and the irreversibility temperature (T_{irr}) are marked on the plot.

Figure 1.7 presents exemplary M vs. T curves obtained from a 12 nm thick single layer of $La_{2/3}Sr_{1/3}CoO_3$ (LSCO) grown on a $LaAlO_3$ (LAO) substrate. The pink curve represents the FC case, where a 0.08 T magnetic field was applied in the in-plane [001] direction during cooling. In contrast, the blue curve represents the ZFC process, with no magnetic field applied. The freezing temperature is indicated by the grey arrow, while the irreversibility temperature (T_{irr}) is marked by the green arrow. In the ZFC case, below the freezing temperature, the FM regions exhibit a disordered state, with spins oriented parallel to each other in a short range but the small FM clusters are ordered randomly from one another due to the local AFM anisotropy induced by the identical Co ions, leading to spin glass behavior. As the temperature rises above the freezing point, thermal energy becomes sufficient to randomize the FM moments, resulting in a decrease in magnetization. Conversely, in the FC case, the spins all align with the magnetic field direction during cooling, leading to a standard FM M vs. T curve. The observed behaviors in the M vs. T curves provide valuable insights for further understanding and engineering magnetic properties of LSCO thin film.

In addition to its magnetic properties, $La_{1-x}Sr_xCoO_3$ holds great promise as a potential candidate for neuromorphic computing [15], owing to its high oxygen vacancy conductivity and relatively low oxygen vacancy formation energy [39]. The versatility of its functionality can be effectively controlled by adjusting both anion and cation concentrations. The ABO_3 perovskite structure exhibits remarkable topotactic phase transformations, leading to diverse perovskite-related phases. These transformations involve the formation of oxygen-deficient perovskite (OD-P, $ABO_{3-\delta}$), Grenier (GN, $ABO_{2.7}$), brownmillerite (BM, $ABO_{2.5}$), and square planar (SP, ABO_2) phases by the loss of oxygen ions, as well as Ruddlesden-Popper (RP, $A_{n+1}B_nO_{3n+1}$, n=integer)

phases through the loss of both oxygen ions and B-site cations, as illustrated in **Figure 1.8** [14,21,40,41]. In a previous study [41], Dr. I-Ting Chiu *et al.* investigated the evolution of physical properties in LSCO thin films exposed to highly reducing environments. The resulting crystalline RP phase was found to involve the loss of both oxygen anions and cobalt cations upon annealing, leading to isolated Co ions or Co nanoparticles. This understanding of the perovskite phase transformations holds significant implications for tailoring and designing materials with enhanced functionalities for neuromorphic computing.

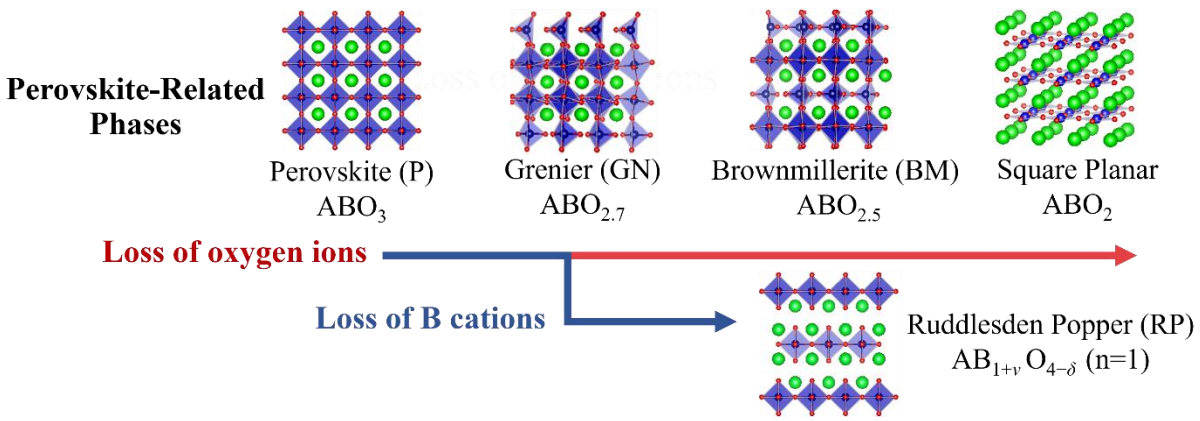

Figure 1.8 Perovskite oxide phase transformations by losing oxygen ions and B-site cations.

1.1.5 $La_{1-x}Sr_xMnO_3$

$La_{1-x}Sr_xMnO_3$ is a highly promising material for magnetic applications due to its tunable crystal structure, electrical, and magnetic properties by varying the doping level of Sr, as depicted in **Figure 1.9** [42]. When $x < 0.5$, $La_{1-x}Sr_xMnO_3$ resides in the FM regime, where one of its remarkable attributes is the colossal magnetoresistance (CMR) effect. The CMR effect allows $La_{1-x}Sr_xMnO_3$ to exhibit a significant change in electrical resistivity by orders of magnitude when subjected to a magnetic field. This property makes $La_{1-x}Sr_xMnO_3$ highly valuable for

magnetic sensing and memory applications. Similar to $La_{1-x}Sr_xCoO_3$, within the FM region, the double exchange interactions between Mn^{3+} and Mn^{4+} ions dominate the magnetic properties. In this dissertation, $La_{1-x}Sr_xMnO_3$ thin film with x = 1/3 was utilized as this composition falls within the metallic and FM phase region at temperatures below T_c, providing an ideal material for exploring and harnessing its intriguing magnetic properties for various magnetic device applications.

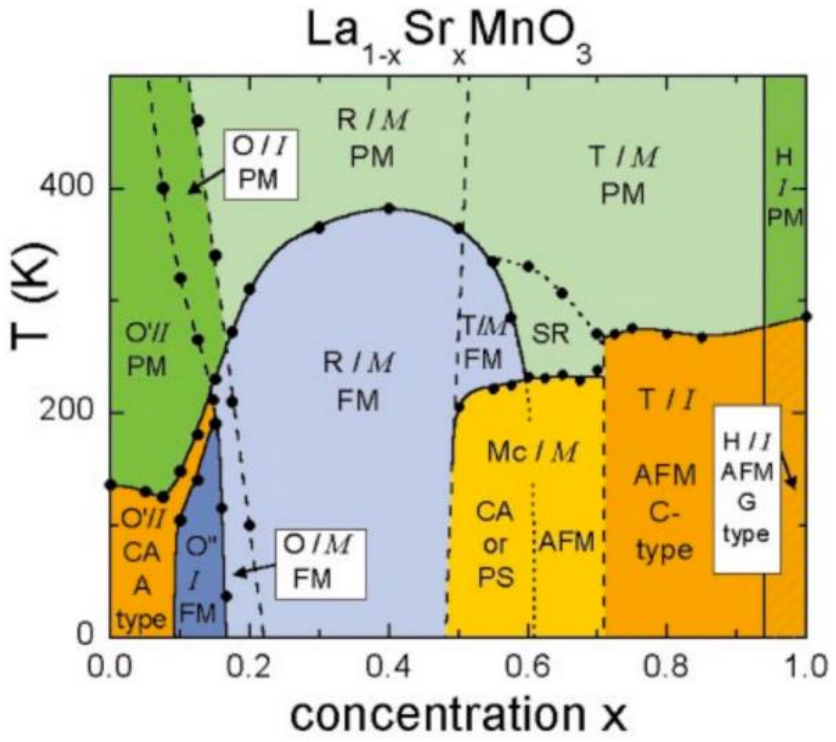

Figure 1.9 Phase diagram of $La_{1-x}Sr_xMnO_3$ [42]. Crystal structure notations on the plot: O': Jahn-Teller distorted orthorhombic; O: orthorhombic; O": orbital-ordered orthorhombic; R: rhombohedral; T: tetragonal; Mc: monoclinic; H: hexagonal. Magnetic structure notations: PM: paramagnetic; SR: short-range order; CA: canted antiferromagnetic; FM: ferromagnetic; PS: phase separated. Notations of electronic state: I: insulating; M: metallic.

As another promising candidate capable of undergoing topotactic phase transformation, a previous study has demonstrated that the incorporation of an epitaxial oxygen getter layer can induce an oxygen vacancy ordered superlattice in buried $La_{0.7}Sr_{0.3}MnO_3$ (LSMO) films. This induced structure has been identified as the brownmillerite phase [4]. The discovery of such phase transformations opens up new avenues for tailoring and engineering the properties of LSMO films, offering exciting prospects for their utilization in advanced electronic and magnetic device applications.

1.1.6 $La_{1-x}Sr_xFeO_3$

For $LaFeO_3$, 3*d* orbitals of Fe^{3+} ions give rise to G-type AFM/insulating property (see the structure in **Figure 1.10** (a) and the phase diagram in **Figure 1.10** (b)) with a Néel temperature (T_N) of 750 K [43,44]. Substitution of Sr on the A-site adds a hole to the hybridized Fe 3*d* and O 2*p* states [45], resulting in increased electrical conductivity and a decreased T_N [46,47]. In $La_{1-x}Sr_xFeO_3$ thin films, the AFM domains typically lie along <100> crystallographic directions but cant out of the plane of the film by ~30° [48]. The AFM spin axis can also be affected by factors such as substrate orientations, strain state, and film thickness [49–52].

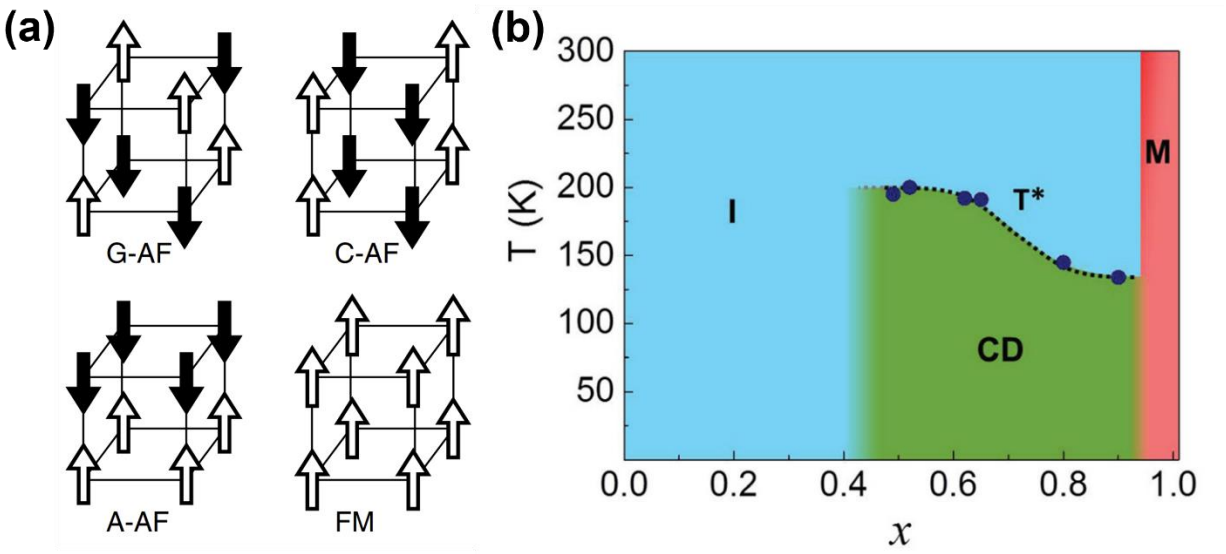

Figure 1.10 (a). Arrangements of A, C, and G-type AFM ordering, as well as FM ordering. The white and black arrows represent magnetic moments oriented upwards and downwards, respectively. (b). Electronic phase diagram of $La_{1-x}Sr_xFeO_3$. Notations on the plots: I: insulating phase (blue); CD: charge disproportionation phase (green); M: metallic phase (red); T*: transition temperature from I to CD phase [44].

$La_{1-x}Sr_xFeO_3$ thin films have garnered significant interest due to their intriguing AFM/insulating properties, which makes them potential candidates for spintronic devices, including magnetic sensors, memory elements, and spin valves [53,54]. Their robustness to external field perturbations offers advantages over FM spintronics. Furthermore, the study of $La_{1-x}Sr_xFeO_3$ thin films has extended to investigating interfacial phenomena, particularly magnetoelectric coupling, which holds promise for advancing novel electronic and magnetic devices [50,55]. Spin-flop coupling at $La_{1-x}Sr_xMnO_3/La_{1-x}Sr_xFeO_3$ interfaces has also been heavily investigated as a potential way to control the orientation of the Néel vector [50,51]. Additionally, $La_{1-x}Sr_xFeO_3$'s oxygen vacancy conduction and excellent ionic transport properties have led to exploration as a

promising material for solid oxide fuel cells and electrocatalyst, where it could contribute to improved energy conversion and storage technologies [56,57].

1.2 Exchange Bias Effect

Exchange bias (EB) is an effect extensively investigated in FM/AFM heterostructures [28,58–61] due to its wide range of promising applications in diverse devices. Exchange-spring magnets are composed of a two-phase distribution of hard- and soft-magnetic grains that have potential applications as permanent magnets [62–64], spin valves [17,65], and magnetic recording read heads [66,67]. Hard magnetic layer usually refers to the AFM materials or FM materials with high coercivity (H_c) while soft magnetic layer refers to the FM material with low H_c. For metal FM bilayers, the hard FM layer is rigid with high anisotropy that pins the magnetic moments of the soft FM layer at the interface [62]. The hallmark of EB is a horizontal shift of magnetic hysteresis loops, either in the direction opposite to the biasing or field cooling direction (negative EB) [68–70], or along with it (positive EB) [71–74]. **Figure 1.11** presents a schematic diagram of a typical exchange-biased hysteresis loop and the corresponding spin configurations of an FM-AFM bilayer [60]. The exchange bias effect arises from the pinning effect exerted by the AFM layer on the FM layer at the interface. Below T_N, a significantly larger magnetic field is required to completely flip the spin orientation of the FM layer to align with the applied field direction. This leads to a horizontal shift of the hysteresis loop.

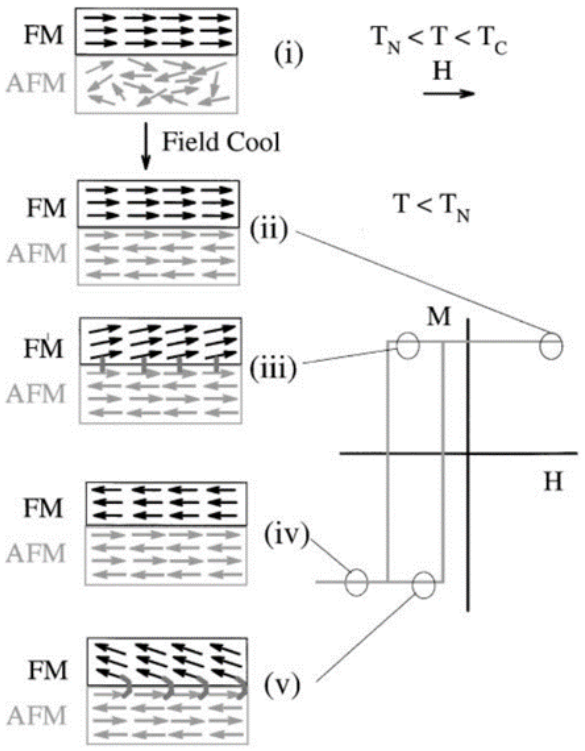

Figure 1.11 Schematic diagram of the spin configuration of an FM-AFM bilayer at different stages (i)-(v) of an exchange biased hysteresis loop [60].

While extensively studied in AFM and FM metals and alloys, magnetic perovskite oxides exhibit unique tunability owing to interactions between charge, orbital, spin, and lattice degrees of freedom [75–78], giving rise to effects such as charge transfer, spin reconstruction, orbital occupancy and strain at the interface [79]. Those unique characteristics have led to the discovery of EB not only in FM/AFM heterostructures but also at interfaces between hard and soft FM layers within perovskite oxides [75,76,80,81]. The exploration of EB in these oxide materials opens up exciting prospects for developing novel magnetic devices with enhanced functionalities and tailor-made properties.

Among perovskite oxides, LSCO and LSMO are promising candidates for investigating the EB effect. LSCO is known for its FM properties with a high H_c [82], making it suitable as a hard magnetic layer. On the other hand, LSMO exhibits lower H_c, rendering it a soft FM layer [83]. In previous studies, bilayers of LSCO/LSMO were epitaxially grown on $(LaAlO_3)_{0.3}(Sr_2AlTaO_6)_{0.7}$ (LSAT) substrates, where LSMO constituted the top layer with a fixed thickness of 6 nm. The LSCO layer thickness varied from 2 to 12 nm [75,76,80,81]. **Figure 1.12** (a) displays the two-step magnetic hysteresis loop obtained for a bilayer with 8 nm LSCO [76]. The shape of the loop indicates the existence of soft and hard FM layers. The inset figure schematically illustrates the magnetic structure of the bilayer. Starting from the bottom, a non-FM LSCO layer exists at the LSCO/substrate interface, followed by a bulk-like hard FM LSCO layer dominated by a mixture of Co^{3+} and Co^{4+} ions. At the LSCO/LSMO interface, a soft FM LSCO layer is observed, characterized by Co^{2+} ions. Importantly, the formation of the soft LSCO layer is only observed when the LSCO layer thickness is below a critical value, which resulting from the charge transfer in the form of $Mn^{3+} + Co^{3+} \rightarrow Mn^{4+} + Co^{2+}$. **Figure 1.12** (b) illustrates the biased minor loops of the bilayer. The vertical shift of the minor loop arises from the magnetization of the hard LSCO layer, which remains oriented along the initial biasing field direction. Meanwhile, the lateral shift is attributed to the soft LSCO and LSMO layer, which becomes pinned by the underlying hard LSCO layer. This two-step hysteresis behavior, along with the distinct magnetic configurations, highlights the intriguing EB effect observed in the LSCO/LSMO bilayer system and its potential relevance for magnetic device applications.

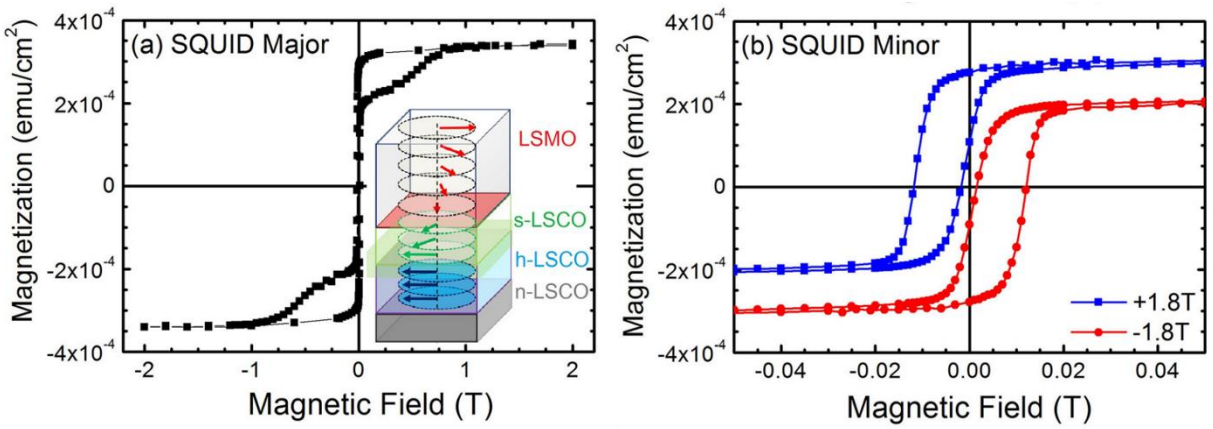

Figure 1.12 Major hysteresis loop (a) and biased minor loop (b) for LSCO/LSMO bilayer with 8 nm LSCO [76].

1.3 Outlook

This dissertation is structured around two primary components, which are built upon previous studies and results. In the first part, we focused on the EB effect of LSCO/LSMO bilayers grown on LSAT substrates, as investigated in previous research. However, several fundamental questions remain unanswered in this area. Specifically, we seek to understand how film strain and the substrate material's structure influence the EB effect and the electron configurations of the bilayer. In the second part, based on the results of phase transformations of LSCO under vacuum annealing, we further explore how other annealing environments impact this transformation. Additionally, we aim to investigate whether similar phase transformations can be observed in other perovskite oxides under vacuum annealing conditions. Chapter 2 provides an in-depth overview of the various techniques used to synthesize and characterize the properties of the perovskite oxides studied in the subsequent chapters. In Chapter 3, we analyze the magnetic properties of LSCO/LSMO bilayers grown on different substrates to assess the effects of strain state by varying the LSCO layer thickness. Building upon this, Chapter 4 delves deeper into the

investigation of the magnetic anisotropy of LSCO/LSMO bilayers and its relationship with the EB effect. Moving forward, Chapter 5 is devoted to exploring the phase transformations of LSCO thin films under hydrogenation and investigating their corresponding functional properties. Subsequently, Chapter 6 discusses the phase transformations and functional properties of two other perovskite oxides, LSMO and $La_{0.7}Sr_{0.3}FeO_3$ (LSFO), under the same vacuum annealing conditions as LSCO in a previous study, enabling a comparative analysis. Finally, in Chapter 7, we present the conclusions drawn from the findings of this dissertation and outline potential future research directions.

Chapter 2

Experimental Techniques

This chapter presents a comprehensive overview of the experimental techniques employed in the research conducted for this dissertation. Thin film synthesis was accomplished using pulsed laser deposition (PLD), and the structural characteristics, including film thickness, density, roughness, and lattice parameters, were measured through x-ray reflectivity (XRR), high-resolution x-ray diffraction (HR-XRD) and reciprocal space maps (RSMs). Bulk magnetic properties were determined using vibrating sample magnetometry (VSM) from Quantum Design. The electrical transport properties of the films were assessed using a Lakeshore cryogenic probe station. Soft x-ray absorption (XA) and x-ray magnetic circular dichroism (XMCD) spectroscopy provide element-specific electronic and magnetic information for thin film featuring multiple magnetic ions. X-ray linear dichroism (XLD) analysis allowed for insights into the structural or magnetic ordering asymmetry and 3*d* orbital occupancy of the B-site ions within the perovskite oxide thin film.

2.1 Pulsed Laser Deposition

2.1.1 Introduction

Pulsed laser deposition (PLD) stands as a versatile and widely employed physical vapor deposition technique for the precise fabrication of thin films. The primary components of a PLD system comprise a vacuum system, an ultraviolet laser (e.g., KrF excimer laser with λ = 248 nm

in this study), target materials, and a substrate on the heater plate as depicted in **Figure 2.1** (a). By focusing a high-intensity laser beam onto the target in the deposition chamber, sublimation and partial ionization of the target surface occur, generating the ablation plume (refer to real plume image in **Figure 2.1** (b)). This plume encompasses various atomic, ionic, and molecular species, transported through the chamber and deposited onto the substrate, positioned approximately 5-10 cm from the target in the path of the plume. The substrate, affixed to a heater plate capable of reaching elevated temperatures, is often rotated to ensure uniform film growth. The ability to maintain the stoichiometry of the target material during the deposition process, along with other advantages (simplicity, versatility, rapid growth, high film quality and cost-effectiveness) compared to other thin film growth techniques such as molecular beam epitaxy and sputtering [84], making PLD particularly suitable for complex oxide materials and multi-element compounds [10,11].

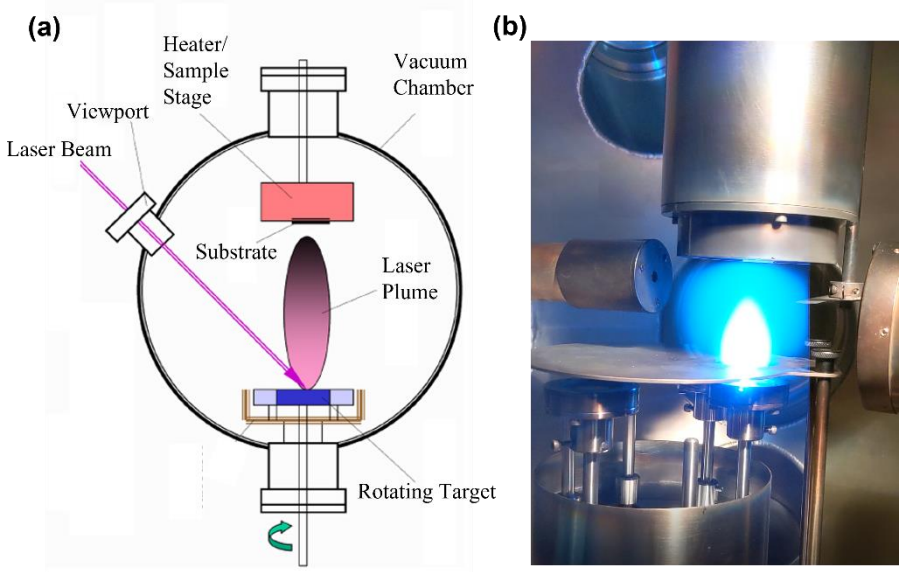

Figure 2.1 (a) Schematic of a standard PLD chamber [85]. (b). Captured image of the laser striking the target material, displaying the real plume during deposition.

2.1.2 Parameters to control

Several crucial parameters can be precisely controlled to optimize thin film quality on several factors that related to crystalline thin film nucleation and growth, including laser energy density, O_2 pressure, substrate temperature, target-substrate distance, and laser pulse repetition rate. Achieving optimal growth conditions and producing high-quality films often involves a trial-and-error approach. Details of each parameter and its impact on thin film quality are discussed below:

A. Laser energy density

Achieving the appropriate laser energy density is critical for the successful creation of the plume and ensuring stoichiometric material transfer from the target to the substrate. However, excessive laser energy can result in the generation of significant particulates, which can degrade the quality of the thin film. For perovskite targets, a typical laser energy density of around 1 J/cm^2 is often sufficient to ablate all the chemical species within the target [86–88]. Nonetheless, variations in laser energy density may arise based on different target materials. To control the laser energy density, a common approach is to optimize the laser spot size on the target by adjusting the focusing lenses on the beam path. By changing the laser spot size, both the energy density and the amount of material ablated from the target during one pulse can be regulated, thereby influencing the film growth rate. Larger laser spot sizes increase the number of incident chemical species impinging on the substrate surface, leading to a faster growth rate. Conversely, smaller spot sizes enable precise thickness control of sublayers in superlattice systems, making them particularly useful for fine-tuning film properties and achieving tailored thin film structures.

B. O_2 pressure

The presence of oxygen gas during deposition serves multiple purposes. Firstly, it prevents the formation of oxygen vacancies in the perovskite oxides, which is vital for maintaining their stoichiometry and the desired magnetic/electronic properties due to the indirect exchange interactions between B-site ions. Secondly, the oxygen gas assists in creating the plasma plume during the laser ablation process [89]. Excessive plasma kinetic energy can be detrimental to the substrate surface, resulting in films with rough interfaces and reduced crystallinity [90]. By promoting atomic collisions, the oxygen gas reduces the kinetic energy of the chemical species within the plume that impinge on the substrate during deposition. Therefore, it is essential to strike a balance between sufficient oxygen incorporation and reducing plasma kinetic energy. Performing the deposition in an oxygen deficient environment can be an effective way to create oxygen-deficient phase purposely [91].

C. Substrate temperature

Substrate temperature significantly influences film quality. Sufficiently high temperatures facilitate surface diffusion of deposited ions, leading to high-quality films. However, extremely high temperatures can result in interdiffusion between layers, hindering the formation of films with well-defined chemical interfaces. Therefore, optimizing substrate temperature requires considering both surface diffusion and interdiffusion to obtain thin films with exceptional structural quality [92–94].

D. Target-substrate distance

The distance between the substrate and target can also be varied to optimize the energy of arriving species. The visible plume size and shape are determined by the chosen oxygen gas pressure and the laser spot size, the distance is selected to ensure the plume tip is focused on the

substrate surface. In the projects of this dissertation, the target-substrate distance is fixed at 1.75 inches.

E. Laser pulse repetition rate

The laser pulse repetition rate can be used to control island growth on substrate orientations with high surface energy. For instance, films grown on (110)-oriented perovskite substrates may form facets that orient preferentially along the <001> family of directions, leading to rougher films with potentially degraded functional properties. Adjusting the laser repetition rate or decreasing the temperature limits the system's ability to reach thermodynamic equilibrium and can overcome this effect, allowing for layer-by-layer growth for higher energy film orientations and obtaining non-equilibrium and metastable results [95,96].

In conclusion, the intricate interplay of growth parameters in PLD requires careful optimization to achieve high-quality films. The laser energy density, oxygen gas pressure, substrate temperature, and laser repetition rate, play critical roles in obtaining films with desired properties and structural characteristics. In this dissertation, the thin film thickness is mainly controlled by adjusting the number of laser pulses while keeping other parameters the same.

2.1.3 Thin film growth mode

By manipulating the deposition parameters, the deposition process can lead to three primary modes of thin film growth, which are determined by a delicate balance of three surface energies, as illustrated in **Figure 2.2** [97]: γ_s, γ_i and γ_F, which corresponding to the energy between the substrate and atmosphere, energy between film and substrate, energy between the film and atmosphere, respectively. The contact angle between the film and substrate is defined as θ. The

three growth modes are known as island growth (Volmer–Weber mode), layer-by-layer growth (Frank–van der Merwe mode), and layer plus island growth (Stranski–Krastanov mode).

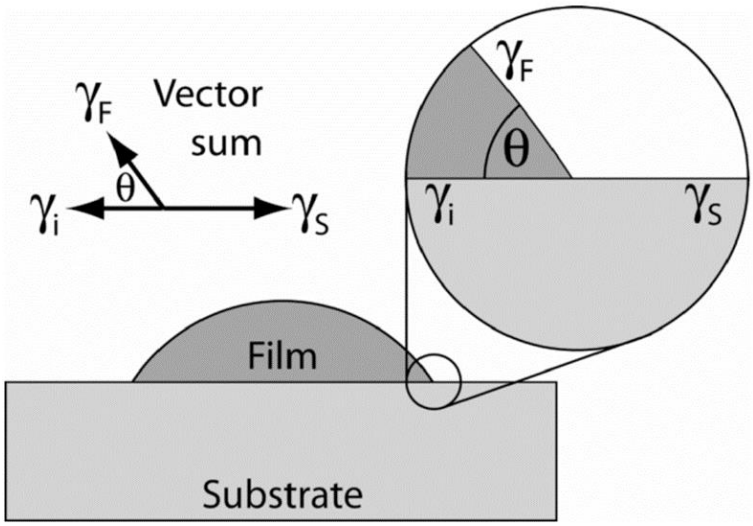

Figure 2.2 The geometry of an island of film on a substrate surface showing the contact angle (θ) and surface energies (γ_F: energy between the film and atmosphere; γ_i: energy between the film and substrate; γ_s: energy between the substrate and atmosphere) [98].

In the island growth mode, the contact angle $\theta > 0$, gives

$$\gamma_s < \gamma_i + \gamma_F * \cos\theta \tag{2.1}$$

The adatoms deposited on the substrate surface are more attracted to each other, leading to the formation of clusters or islands as shown in **Figure 2.3** (a) [99]. These islands grow independently and exhibit three-dimensional morphology, resulting in rough surfaces and interfaces of the film, creating difficulties of measuring the thickness and interfacial areas of heterostructures.

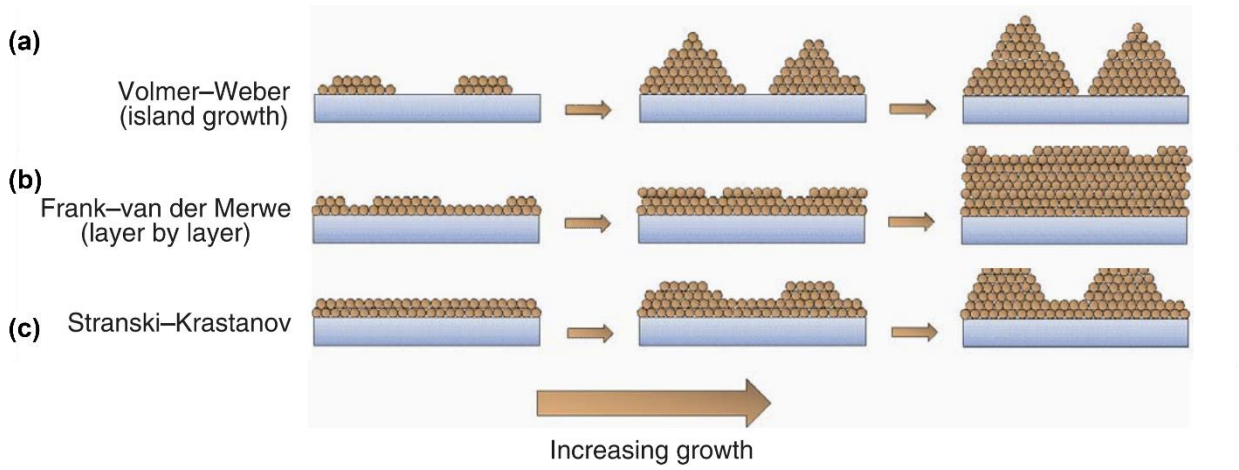

Figure 2.3 Three growth mode in thin film deposition: (a) island growth; (b) layer by layer growth; (c) Stranski-Krastanov growth, a combination of island growth and layer-by-layer growth [99].

Conversely, in the layer-by-layer growth mode as shown in **Figure 2.3** (b), the adatoms preferentially align and form smooth monolayers on the substrate surface rather than creating islands. This mode of growth generally results in two-dimensional growth with a well-defined and uniform monolayer arrangement. Layer-by-layer growth requires that the nucleated regions during film growth spread evenly and coalesce into a single layer, which requires a contact angle θ = 0 or 180° ($\cos\theta = 1$) and satisfies

$$\gamma_s \geq \gamma_i + \gamma_F \tag{2.2}$$

The third mode, known as the Stranski–Krastanov mode, represents an intermediate between island and layer-by-layer growth, as depicted in **Figure 2.3** (c). In this mode, one or more monolayers form on the substrate before islands start growing atop these initial layers. The islands exhibit distinctive three-dimensional characteristics, while the underlying layers exhibit two-dimensional growth. This mode is typically observed when increasing the film thickness: at the early stage, the film is fully strained on the substrate, resulting in uniform monolayers.

However, as the film thickness increases, the lattice strain can be relieved by forming dislocations or vacancies. This relaxation of misfit strain provides opportunities for island growth [100].

The growth mode in thin films is influenced by several factors, as discussed in **Section 2.1.2**, with surface energies playing significant roles. Consequently, achieving the desired epitaxial thin film requires fine control of the deposition parameters to ensure the expected morphology, structure, and functional properties of the deposited film.

2.2 Structural Characterization

The functional properties of complex oxide thin films are closely related to their crystal structure, making the characterization of the crystalline structure essential. X-ray diffractometer is a powerful non-destructive experimental technique used to determine the crystal structures of thin films. In this dissertation, several structural characterizations of the thin films were performed using a Bruker D8 Discover four-circle diffractometer, which is a versatile x-ray diffractometer capable of various analyses. The setup of the Bruker D8 Discover involves an x-ray generator with a copper anode that produces characteristic x-rays ($K_{\alpha 1}$, $K_{\alpha 2}$, *and* K_{β}). The x-rays are then filtered by a parabolic Goebel mirror to produce a mutually parallel beam containing only K_{α} x-rays. Slits on the incident beam path help to balance the x-ray intensity and select the collimated x-ray beam with high angular resolution. The sample stage allows for movement in x, y, z directions and rotation in Phi and Chi directions, enabling precise positioning of the thin film for measurement. **Figure 2.4** displays a representation of an x-ray diffractometer used in this dissertation. For high-resolution X-ray diffraction (HR-XRD) and reciprocal space mapping

(RSM) measurements, a Ge (220) two-bounce monochromator is introduced in the incident beam path to eliminate $K_{\alpha 2}$ radiation and achieve high angular resolution. In this configuration, the x-ray tube remains fixed while the detector and sample can move. The detailed fundamental mechanisms of the structural characterizations will be discussed in this section.

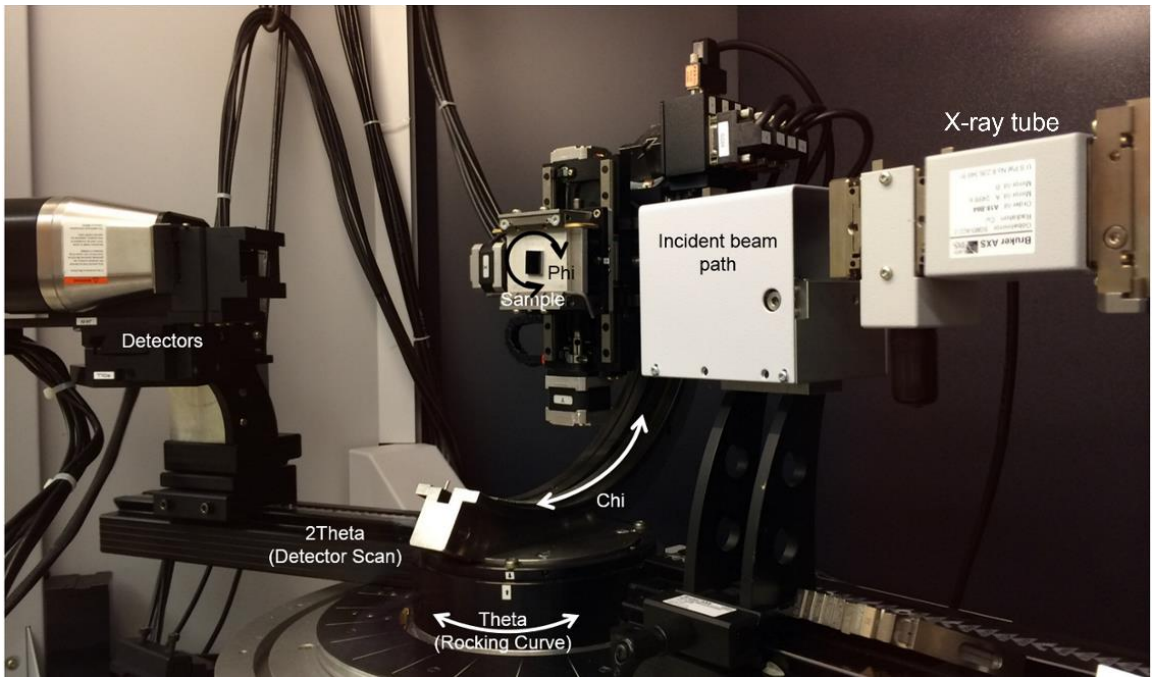

Figure 2.4 Bruker D8 Discover diffractometer

2.2.1 X-Ray Reflectivity

XRR is a powerful thin film surface characterization technique used to obtain information including film thickness, density, and roughness [101]. The fundamental principle of XRR is based on Snell's Law:

$$\frac{n_a}{n_f} = \frac{cos(\theta_2)}{cos(\theta_1)} \tag{2.3}$$

The above equation describes the relationship between the refractive indices of atmosphere (n_a),

film (n_f), substrate (n_s) and angles (θ_1 and θ_2). The geometry of a XRR measurement schematically shows in **Figure 2.5**.

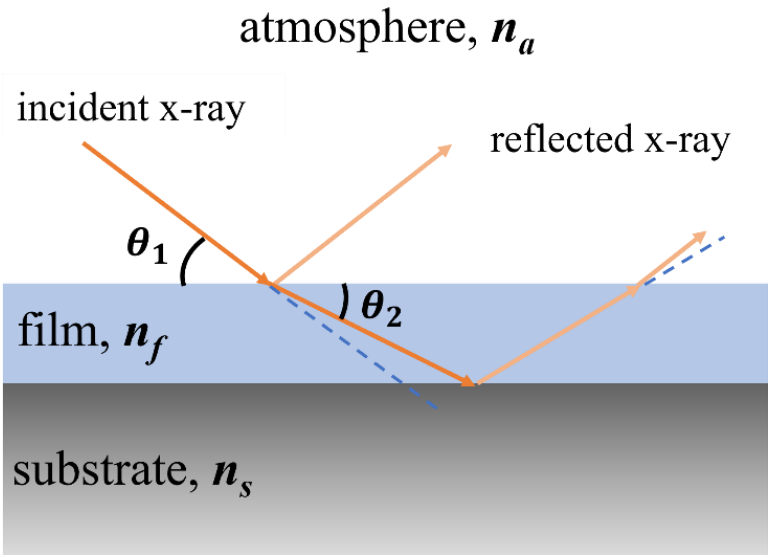

Figure 2.5 Geometry of a typical XRR measurement that based on Snell's law. n_a, n_f and n_s are the refractive indices of atmosphere, film and substrate. θ_1 is the angle between incident x-ray and the film surface, θ_2 is the angle between refracted x-ray and the film surface.

During an XRR measurement, when the angle between the incident x-ray and the film surface exceeds a critical value (θ_c), the x-rays can penetrate through the film and reflect from the film-substrate interface. This reflected part of the beam experiences a phase difference with the beam reflected from the film surface, resulting in constructive and destructive interference. The interference appears as intensity oscillations (known as thickness fringes) in the XRR curve with a period proportional to the film thickness. Thus, by analyzing the periodicity of the oscillations, valuable information about the film thickness can be obtained. Thicker films exhibit shorter periodicity while thinner film shows larger periodicity. The roughness of the film-substrate

interface and the film surface can also be determined from the decay rate of the XRR curve. A faster decay indicates larger roughness while smoother surface/interface gives slower decay of the XRR curve.

Moreover, the critical angle θ_c in XRR is related to the material's density by $\theta_c = \sqrt{2\delta}$ [101], where δ is a function proportional to the material's density, ρ [102]. In XRR curve fitting, the critical angle analysis allows for the extraction of material density information. However, challenges arise when there is a minimal density difference between the film and the substrate, resulting in shallow thickness fringes in the XRR curve. In such cases, obtaining accurate thickness information from the curve fitting becomes difficult. This situation can also occur in heterostructures with layers having similar densities, where the individual layer thicknesses become indistinguishable. As a result, precise determination of layer thicknesses becomes more complex and requires careful consideration and advanced experimental techniques to ensure accurate results, which will be discussed in the following section.

In **Figure 2.6**, the XRR curve of a LSCO film grown on a $SrTiO_3$ (STO) substrate is presented. The curve was acquired using the Bruker D8 Discover diffractometer, and the raw data was subjected to fitting analysis using GenX software [103]. This fitting process allowed us to extract crucial information, including film thickness, roughness, and density, which are summarized in **Table 2.1** along with the corresponding fitting parameters. It is important to exercise caution and expertise in evaluating the reasonability of the fitting parameters, considering the understanding and expectations of the film properties. This careful analysis ensures that the obtained results are accurate and reliable for further interpretation and understanding of the thin film's structural

characteristics.

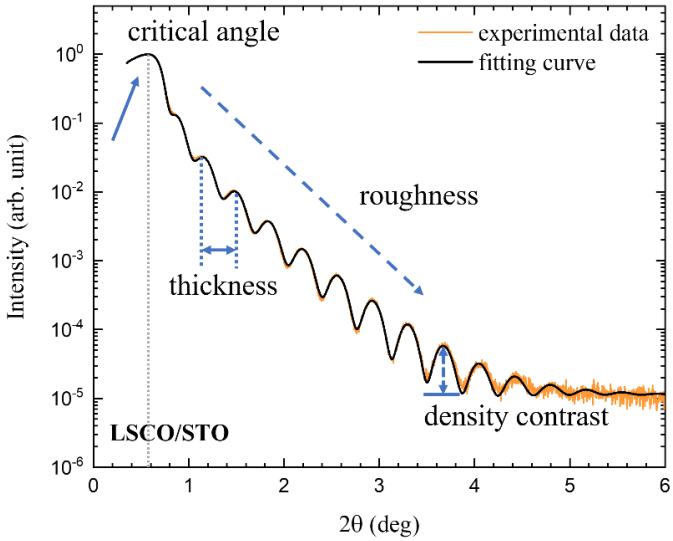

Figure 2.6 Experimental (orange) and fitted (black) curve of a 23 nm LSCO film on an STO substrate. Notations of critical angle, thickness, roughness and density contrast are marked on the plot.

Table 2.1. XRR fitting parameters of a single layer LSCO/LSAT shown in **Figure 2.6**

Layer	Thickness (nm)	Roughness (nm)	Density (g/cm^3)
LSCO	23.27	0.66	6.66
STO substrate	-	0.25	Bulk value

2.2.2 Resonant X-Ray Reflectivity

As discussed in the preceding section, differentiating between the thicknesses of individual layers becomes challenging in campus-based x-ray diffractometry, particularly when the layers

possess similar densities, leading to minimal layer contrasts that are difficult to observe [104]. To address this issue and obtain more precise structural parameters for multilayers or superlattices, reflectivity profiles can be measured at the resonance edges of atoms in each specific layer using synchrotron radiation with tunable energy.

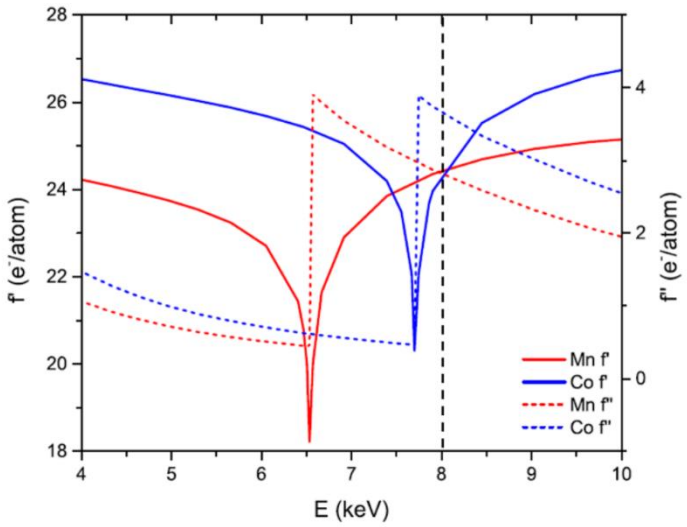

Figure 2.7 Scattering factor (f') and absorption factor (f'') of metallic Mn and Co as a function of photon energy [105].

The reflection of x-rays is governed by the scattering length density (SLD) of the material being analyzed. The SLD is influenced by both the chemical and electronic densities, with x-rays interacting with the electron distribution within the material. This dependence on electron distribution is determined by element-specific atomic scattering factors, f' and f'', which govern the scattering and absorption of individual atoms, respectively [106]. Notably, the f' value exhibits a strong dependence on x-ray energy, resulting in an abrupt decrease at absorption edges as shown in **Figure 2.7** [105]. In contrast, the f'' value sharply increases at the absorption energy. When considering RXRR spectra, both real and imaginary parts of the scattering factor are taken

into account. As a result, the RXRR technique provides heightened sensitivity to the chemical contrast between thin films and substrates that have similar densities.

2.2.3 X-Ray Diffraction

Characterizing the crystallographic structure and lattice parameters of epitaxial thin films is of paramount importance for understanding their properties and functionality. While XRR is a valuable technique for thin film characterization, it is insensitive in providing crystallographic information. For such purposes, x-ray diffraction (XRD) measurements are essential.

When epitaxial thin films are grown on single-crystalline substrates with different crystal structure or lattice constants, the in-plane lattice parameters of the film align with those of the substrate, causing deformation of the thin film crystal structure and potential changes in the out-of-plane lattice constant. In XRD, when x-rays interact with a lattice plane of the thin film, constructive interference occurs according to Bragg's Law:

$$2d_{hkl}\, sin\, \theta \;=\; n\lambda \tag{2.4}$$

This equation relates the incidence and reflection angles of x-rays (θ) to the atomic plane spacing (d_{hkl}) between the (*h k l*) crystal planes in the lattice. Here, *n* is an integer representing the order of the diffraction peak, and λ is the wavelength of the incoming x-rays. In campus-based x-ray diffractometer, λ is the wavelength of Cu $K_{\alpha 1}$ (λ = 1.5406 Å). **Figure 2.8** shows the basic geometry used to derive the diffraction condition described by Bragg's Law [107].

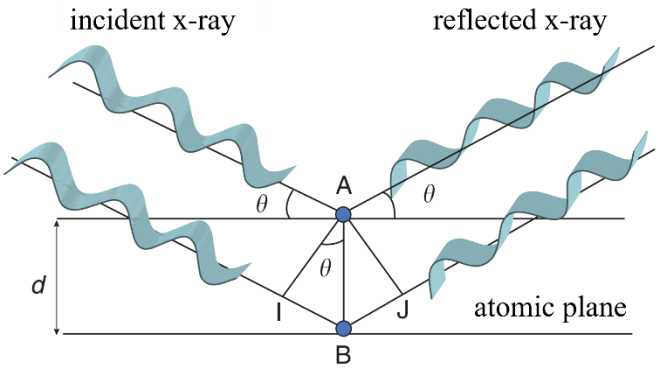

Figure 2.8 X-ray diffraction illustrated between two crystallographic planes, demonstrating Bragg's Law [107]. The horizontal lines represent atomic planes with an atomic spacing marked as '*d*.' The incident angle between the x-ray beam and the crystal plane is denoted as θ.

Symmetric ω-2θ scans, commonly known as theta-two theta (TTH) scans are employed to determine the out-of-plane lattice constants. In TTH scans, for planes parallel to the film surface ω will deviate away from half of 2θ due to the miscut of the substrate surface so that the diffraction planes are not exactly parallel to the sample surface. TTH scans give information of diffraction peaks corresponding to both film and substrate, accompanied by Kiessig fringes, arising from the same phenomenon as in XRR, as exemplified in **Figure 2.9** for LSCO thin film on STO substrate. The LSCO film peak appears broader and less intense compared to the STO substrate peak due to finite size effects. The sharp substrate peak indicates a well-defined crystalline phase with minimal *d*-spacing variations. Several important quantities can be extracted from these scans, such as the out-of-plane lattice parameter, which can be calculated using Bragg's Law. By comparing the result against the bulk lattice parameter, the strain values of the thin film can be extracted.

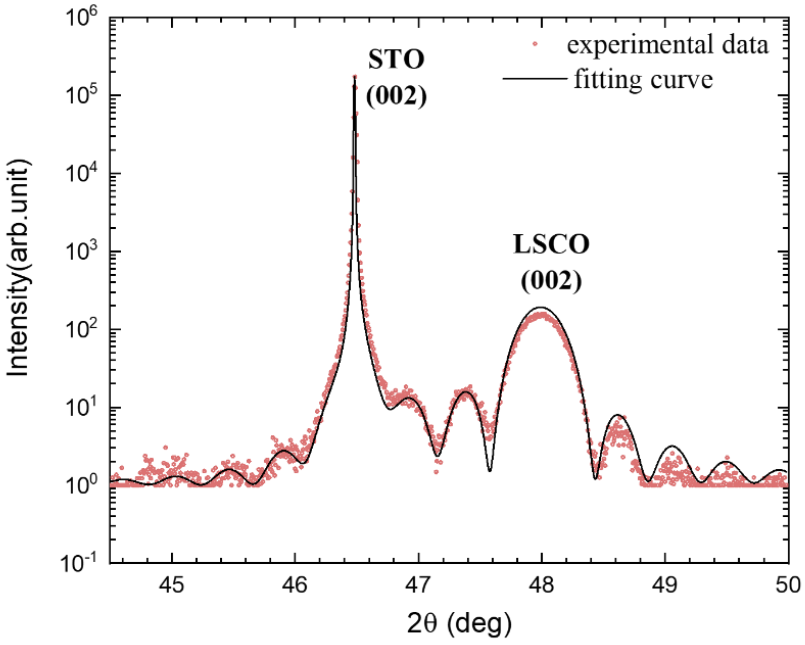

Figure 2.9 Experimental data (pink) and fitted curve (black) of a LSCO thin film on an STO substrate (same sample as shown in **Figure 2.6**). The sharp peak around 45° is the (002) STO substrate peak, the broad peak with highest intensity around 48° is the (002) LSCO film peak, the rest of the lower broad peaks are Kiessig fringes.

Additionally, well-defined Kiessig fringes signify structural coherence and smooth interfaces within the film. These fringes result from constructive interference, which becomes shallower or even disappears if there are significant variation in *d*-spacing throughout the film thickness. For instance, in thin films grown on $LaAlO_3$ (LAO) substrates, Kiessig fringes are often challenging to observe due to twin structure of LAO that causes rougher interfaces. The Kiessig fringes can also be employed to determine the total film thickness in a manner similar to XRR modeling.

Besides TTH scans, rocking curve scans can also provide information about the film quality. The measurements of rocking curves involve fixed the detector position (2θ) and scanning ω

(also known as rocking) around the peak. Sharp rocking curves indicate high structural purity of single-crystalline materials, while broadening of the curves suggests the presence of mosaicity and defects such as dislocations so that the planes participating in diffraction have some variations in the angle of their surface normals. By comparing the full width at half maximum of the film and substrate peak rocking curves, the structural quality of the film relative to the substrate can be assessed.

2.2.4 Reciprocal Space Maps

While symmetric TTH scans provide valuable information about crystalline quality and out-of-plane lattice parameters, they are insufficient in revealing the relationship between the in-plane lattice parameters of the film and substrate. To obtain this information, which indicates the quality of epitaxial growth, asymmetric scans are needed. These scans involve measuring diffraction from crystallographic planes that intersect one of the in-plane directions. This measurement requires more complex combinations of ω and 2θ positions, as ω and 2θ are no longer coupled, as in the case of symmetric TTH scans. In addition, chi and phi angles as shown in **Figure 2.4** need to be optimized to get to the right diffraction conditions.

The reciprocal lattice, a Fourier transform of the real-space lattice, plays an essential role in interpreting diffraction conditions and identifying crystal structures. The reciprocal lattice is defined by primitive reciprocal lattice vectors $\boldsymbol{a^*}$, $\boldsymbol{b^*}$, and $\boldsymbol{c^*}$. Points in reciprocal space correspond to atomic planes in real space that are perpendicular to the reciprocal lattice vector $\boldsymbol{G}$, where $\boldsymbol{G_{hkl}} = h * \boldsymbol{a}^* + k * \boldsymbol{b}^* + l * \boldsymbol{c}^*$. An RSM measures a selected region in reciprocal space designed to encompass both the substrate and film peaks. Asymmetric RSM can provide valuable

strain state information for the film, by characterizing both in-plane and out-of-plane components. When a film is grown on a substrate with a lattice mismatch, it can be fully relaxed with its bulk structure (**Figure 2.10** (a)), fully and uniformly strained (**Figure 2.10** (b)) or misoriented to the lattice planes of the substrate (**Figure 2.10** (c)). The total volume of the film is not constant before and after deformation. The relationship between in-plane and out-of-plane strain can be described using Poisson's ratio (v):

$$v = 1/(1 - 2 * \frac{\varepsilon_{xx}}{\varepsilon_{zz}}) \tag{2.5}$$

where ε_{xx} and ε_{zz} are the in-plane and out-of-plane strain of the film. It was reported that for epitaxially strained hole-doped cobaltite and typical manganite thin films, the Poisson's ratio is ~1/3 [108–110] that yields $\varepsilon_{xx} = -\varepsilon_{zz}$.

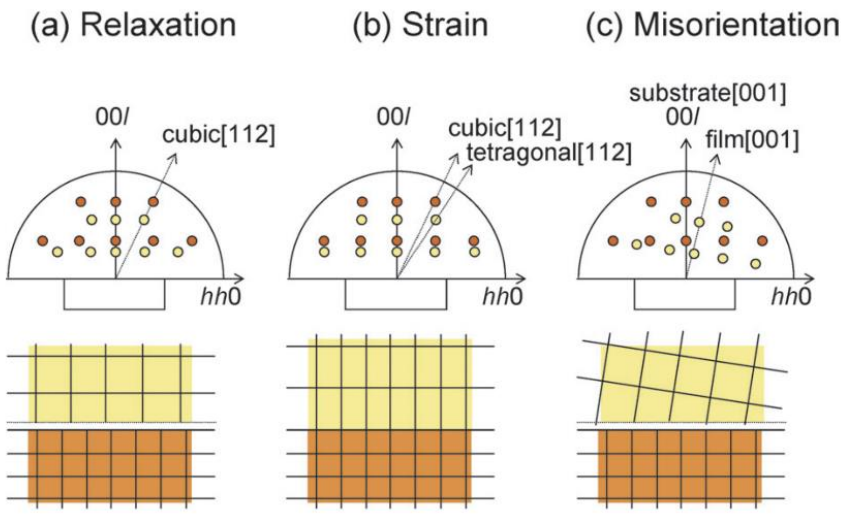

Figure 2.10 Three scenarios of reciprocal lattice configuration between thin film and substrate based on the strain states of the film [111]. Area shaded in yellow represents lattices of the thin film, orange region represents substrate.

The orange and yellow dots in the semicircle in **Figure 2.10** represent lattice planes in reciprocal space. For a fully relaxed film, the points are located along a line connecting the substrate and film reciprocal lattice points through original point (0 0 0), while fully strained film exhibiting vertical alignment with the substrate reciprocal lattice point.

2.3 Bulk Magnetic Characterization

The bulk magnetic properties of thin films in this dissertation were characterized using a vibrating sample magnetometer (VSM). A simplified diagram of the VSM chamber and its components is depicted in **Figure 2.11**. The thin film samples were securely attached to a non-magnetic rod (quartz) using double-sided tape and Teflon seal tape. During the measurements, the sample rod vibrated at a known frequency in the presence of an applied magnetic field (H), generated typically by an electromagnet with uniform pole faces. As the sample vibrated, the oscillating magnetic field induced an electromotive force in the coils, resulting in a current that was directly proportional to the magnetization of the sample [112]. An example of a fully enclosed VSM system is the Quantum Design VersaLab, which operates with helium gas and allows for the generation of magnetic fields up to 3 T and temperatures as low as 50 K.

The VSM technique encompasses two standard tests: magnetization vs. temperature (M vs. T) and magnetization vs. magnetic field (magnetic hysteresis loops, M vs. H). The M vs. T curve provides valuable insights into the magnetic transitions of the thin films as a function of temperature. During this measurement, a small magnetic field is applied to align the magnetic moments. For FM thin films, the measured magnetization exhibits a distinct change at the Curie temperature (T_c), typically determined as the maximum of the first derivative of $|dM/dT|$. It is

essential to avoid applying magnetic fields beyond the value that could align the FM moments above T_c, as this may obscure the determination of transition points.

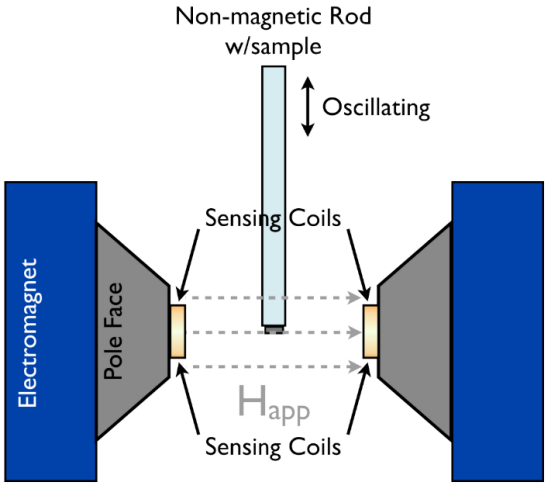

Figure 2.11 Schematic of a VSM chamber and the components in a Quantum Design VersaLab [113].

The magnetic hysteresis loop measurement explores the thin film's response to an externally applied magnetic field, providing crucial parameters such as the saturation magnetization (M_s) when all magnetic moments align parallel to the field, the remnant magnetization (M_r) which is the magnetization at zero magnetic field, and the coercive field (H_c) at which the magnetization reduces to zero after saturation. While VSM is a powerful and widely used technique for bulk magnetic properties, it has inherent limitations when studying multilayers and superlattices since it cannot distinguish between the magnetization contributions of individual layers. VSM is also more likely to be affected by any FM contaminations in the films and substrates. Therefore, complementary techniques like x-ray magnetic circular dichroism (XMCD) are employed for element-specific measurements, as will be discussed in detail in section 2.5.1.

2.4 Electrical Transport Characterization

The electrical properties of perovskite oxide thin films are closely related to the crystal structure and magnetic properties of the thin film and are highly sensitive to external stimuli, such as magnetic field and temperature, thus providing information of Curie temperature (T_c) for FM thin film and metal-to-insulator transition point. The sheet resistance (R_s, in Ω) of thin film is commonly measured using the four-point probe van der Pauw method, which allows for the determination of the resistivity (ρ, in Ω*m), assuming that the current flows only along the in-plane directions of the thin film and has no perpendicular components. The relationship between the ρ and R_s is given by the equation:

$$\rho = R_s * t \tag{2.6}$$

where t is the thickness of the film in meters.

An example set up of the van der Pauw method is shown in **Figure 2.12** where A, B, C and D are the four metal contacts (usually gold, aluminum, or silver paste) that connect to the wires. During the measurements, a voltage is applied across two adjacent contacts (AB), and the current between the other two contacts (CD) is measured. Similarly, a voltage is applied to edge CD, and the current is measured at edge AB. The average of the resistance measurements can be calculated as:

$$R_1 = (R_{AB-CD} + R_{CD-AB}) / 2 \tag{2.7}$$

A similar measurement can be performed across the other set of sample edges (DA and BC), where the averaged resistance is:

$$R_2 = (R_{DA-BC} + R_{BC-DA}) / 2 \tag{2.7}$$

The sheet resistance (R_s) can be solved by the equation below [114]

$$e^{-\pi \frac{R_1}{R_S}} + e^{-\pi \frac{R_2}{R_S}} = 1 \tag{2.8}$$

To use the van der Pauw method, several requirements must be met: 1. the sample must be homogeneous and have a uniform thickness; 2. The sample thickness should be orders of magnitude smaller than the sample width and length; 3. The metal contact area should be at least an order of magnitude smaller than the sample surface area.

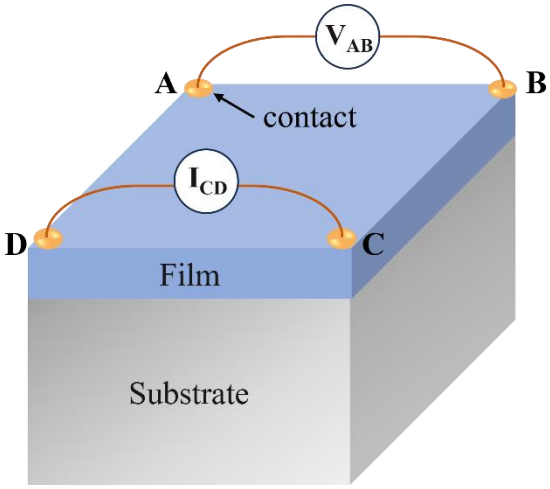

Figure 2.12 A set up of the four-point probe van der Pauw method for resistivity measurements of a thin film sample. A, B, C and D are the four contacts by depositing a small amount of metal (gold or aluminum) or by attaching silver paste at the corners. In this example, a volage is applied between edge AB (V_{AB}) and the current is measured between DC (I_{CD}), the resistance is represented by R_{AB-CD}.

2.5 Soft X-Ray Absorption Spectroscopy

X-ray absorption (XA) spectroscopy emerges as an essential tool for investigating the local electronic structure of perovskite oxide thin films [25,115]. This technique is particularly

invaluable for the analysis of challenging cases, such as ultra-thin layers and thin film heterostructures, where obtaining properties through alternative methods is challenging.

The XA measurement process involves precisely tuning a monochromated x-ray beam to an energy range that can effectively excite core electrons within the sample. The transmitted x-ray beam subsequently experiences a measurable reduction in intensity, which is quantified as the absorption coefficient μ. Mathematically, this coefficient is expressed as the difference between the intensity of the incident beam (I_0) and the transmitted beam (I_t), and it is defined by:

$$\mu = -\frac{ln\left(\frac{I_t}{I_0}\right)}{x} \tag{2.9}$$

Here, x symbolizes the thickness of the sample.

Figure 2.13 (a) shows the XA process, where the x-ray induces the excitation of a core electron (originating from *K* or *L* energy levels) in an atom. This electron is then elevated to an unoccupied energy level (in *L* or *M* energy levels), or it may be ejected from the atom entirely. This event creates a vacancy at a lower energy level, which is subsequently filled by an electron descending from a higher energy state. The energy associated with this transition is released either in the form of an x-ray with equivalent energy (fluorescence detection) or through the generation of an Auger electron. These Auger electrons, in turn, lead to the creation of numerous secondary electrons as they traverse the sample. These electrons are detected and collected to generate the total electron yield (TEY) XA spectrum of the sample. It is important to note that the TEY method is surface sensitive, with the electron sampling depth limited to 5-10 nanometers [116] as shown in **Figure 2.13** (b), and requires the thin film samples to possess good conductivity for electron transport. To acquire insights spanning the entire thickness of the

sample, luminescence yield (LY) detection is commonly employed. In this approach, defects within the substrate function as x-ray detectors and convert x-ray intensity into visible light [117]. Notably, certain substrate types yield better LY signals compared to others. For instance, substrates like LAO and LSAT exhibit better performance than STO substrates at room temperature and around 80 K, which are the temperatures commonly employed for measuring magnetic perovskite thin films.

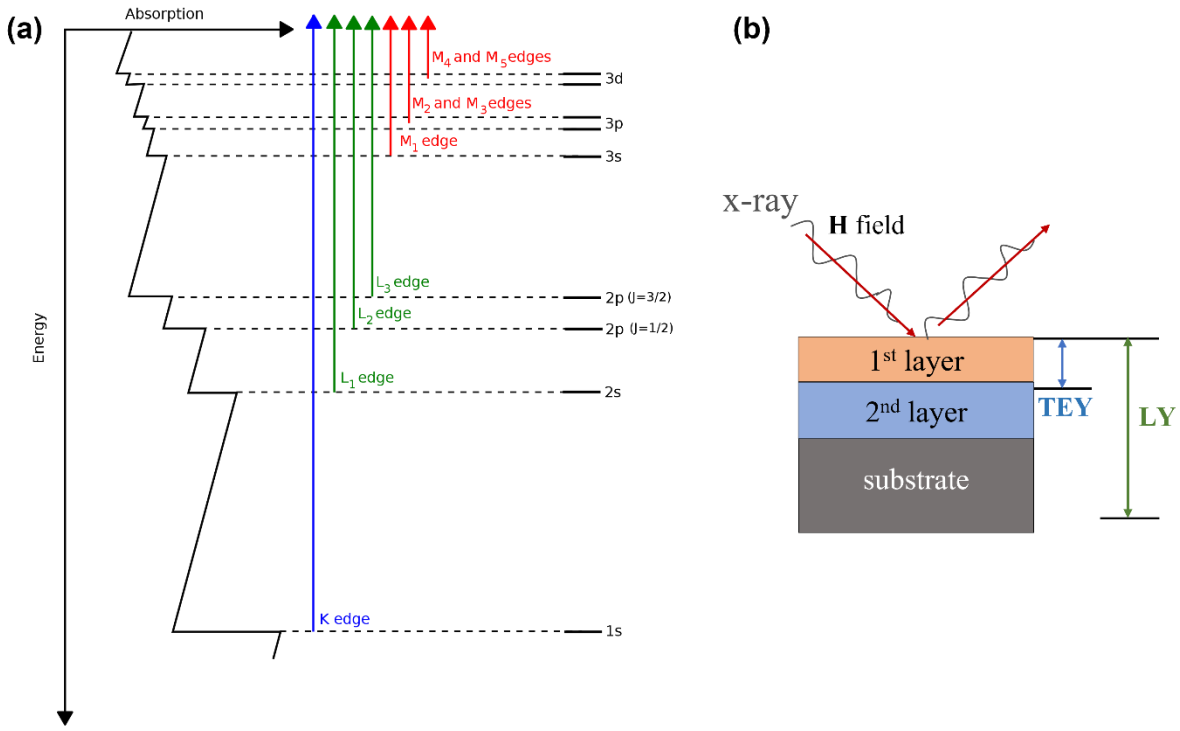

Figure 2.13 (a). Excitation of electrons between *K*, *L*, *M* energy levels and the corresponding x-ray absorption edges [118] (b). Diagram of TEY and LY probing depth on a bilayer thin film sample. The magnetic field (**H**) is parallel to the x-ray in this example.

Synchrotron x-ray radiation is a preferred choice for XA investigations due to its advantageous features, including the high signal-to-noise ratio and tunable energy range. Synchrotrons operate

by injecting high-energy electrons into a storage ring, with bend magnets guiding the electrons along circular paths. The resultant synchrotron radiation is directed towards distinct beamlines tailored to specific scientific goals. Within this context, certain beamlines leverage radiation generated by bend magnets, as exemplified by BL6.3.1 at the Advanced Light Source (ALS) at Lawrence Berkeley National Laboratory. Additionally, the potential of elliptically polarizing undulators (EPUs) is harnessed, as seen in BL4.0.2 at ALS. The advantages of EPUs include: (1) enhanced control over photon polarization, making them particularly advantageous for capturing x-ray magnetic circular dichroism (XMCD) spectra from samples with minimal magnetization; (2) high x-ray flux and better energy resolution; (3) the ability to perform x-ray linear dichroism (XLD)/x-ray magnetic linear dichroism (XMLD) due to the ability to rotate the orientation of the x-ray E-vector to any arbitrary direction. Comparisons with established reference spectra provide valuable insights into the valence states and bonding environments of cations within individual layers.

2.5.1 X-Ray Magnetic Circular Dichroism

The XMCD spectrum is the difference between two XA spectra acquired using oppositely circularly polarized x-rays [119]. This measurement can be conducted by alternating the helicity of the circularly polarized x-rays while maintaining the magnetic field direction (the applied field should be large enough to saturate the sample), or by reversing the direction of the field while sustaining constant x-ray helicity. **Figure 2.14** (a) shows a single-electron excitation process between the 2*p* and 3*d* energy states [119]. The spin-orbit coupling results in the division of the 2*p* level into two energy levels: $2p_{1/2}$ and $2p_{3/2}$. A circularly polarized photon propels a spin-polarized electron from the 2*p* level (traditionally, μ^+ signifies right-polarized light, and μ^-

denotes left-polarized light) into the vacancies within the 3*d* band. The band diagram in **Figure 2.14** (a) shows the availabilities of unoccupied states above the Fermi energy (E_F). Subsequently, the vacancies created at the 2*p* energy level is filled by an electron descending from a higher energy state. This mechanism mirrors a conventional XA process but is influenced by the circular polarization of the x-rays, allowing electron transitions in ferromagnetic (FM) materials to be contingent upon the incoming photon's polarization.

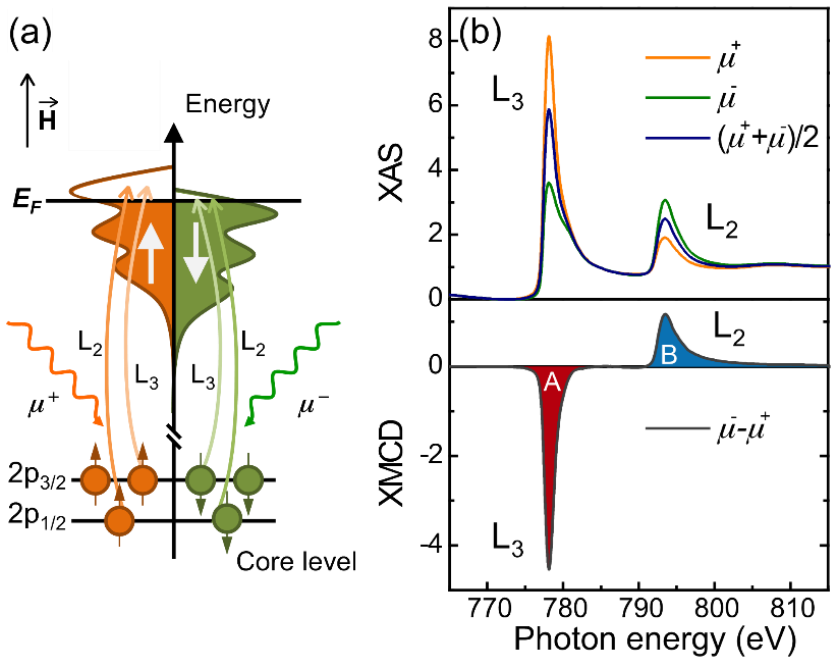

Figure 2.14 (a) Single-electron excitation process between 2*p* and 3*d* energy states of a magnetic material (b) XA/XMCD spectra at the Co $L_{2,3}$-edge. μ^+ is the right polarized x-ray, μ^- is the left polarized x-ray [119].

In **Figure 2.14** (b), the L_3 and L_2 peaks correspond respectively to the transitions from $2p_{3/2}$ and $2p_{1/2}$ to the 3*d* unoccupied energy levels. The intensity of these peaks is governed by the number of electrons transitioning to the 3d unoccupied states. In magnetic materials, one spin band

experiences an energy shift relative to the other, leading to an asymmetry in the available states above E_F between the spin-up and spin-down configurations. The discrepancy between the left and right polarized XA spectra forms the basis of the XMCD spectra. The intensity of the XMCD spectra provides insight into the magnitude of magnetization of the probed element. Furthermore, the spectral line shape of XMCD imparts supplementary information concerning the corresponding magnetically active ions.

2.5.2 X-Ray Linear Dichroism

While XMCD stands as a powerful tool for probing FM materials, its capabilities are limited when it comes to investigating AFM ordering. Therefore, XMLD emerges as an important technique that capable of understanding AFM ordering within a material. By utilizing linearly polarized x-ray beams, XMLD spectroscopy unveils a wide spectrum of asymmetries present within a sample, including crystal-field effects, FM anisotropy, orbital ordering, and the intricate electronic distribution surrounding AFM moments [23,120]. To exclusively probe AFM asymmetries, a setting of two polarization vectors (***E***-vector) along crystallographic directions is employed. One polarization vector aligns along the AFM spin axis, while the other stands perpendicular to it. This experimental setup ensures that the subtle AFM interactions are effectively captured.

An example of XA/XMLD spectroscopy of $LaFeO_3$ at Fe L_2-edge is shown in **Figure 2.15** (a) and (b) [48]. **Figure 2.15** (c) schematically shows the experimental geometry of the XMLD measurements, where the blue arrow represents the ***E***-vector of the x-ray, which is perpendicular to the direction of the x-ray. The XMLD spectrum is derived from the difference between p-

polarized and s-polarized x-rays, where "p" denotes that the E-vector aligns parallel to the plane of incidence, and "s" signifies that the E-vector aligns perpendicular to the plane of incidence.

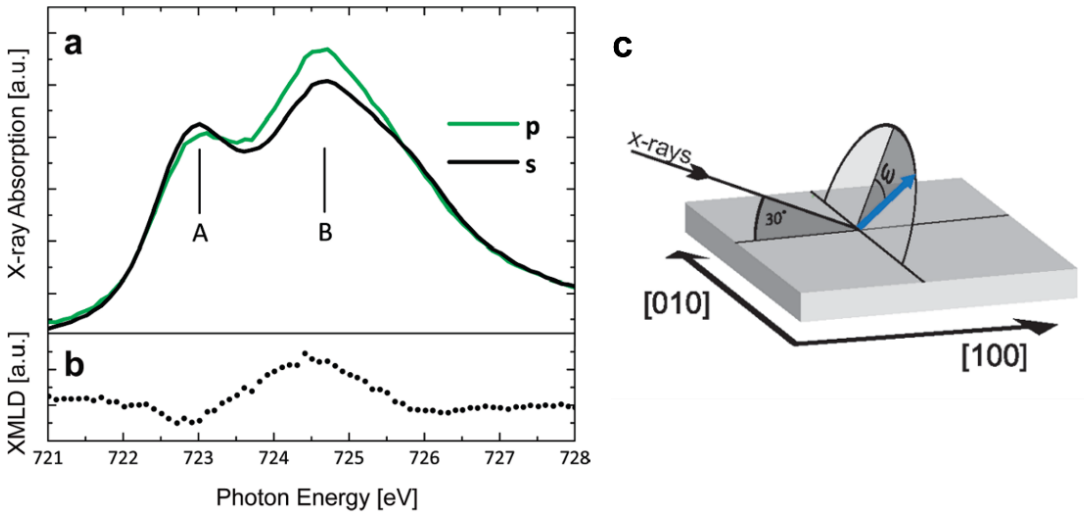

Figure 2.15 (a) XA spectrum of the Fe L_2-edge measured with s- and p-polarized x-rays, respectively. (b) XMLD signal defined as the difference spectrum of the two spectra in (a). (c) Schematic of the XMLD experimental geometry [48].

In addition to its application in probing AFM ordering, another example of XLD is in investigating the electron occupancy of 3*d* orbitals for transition metal ions [121,122], which helps a deeper understanding of the impact of strain and it also shows direct relationship with magnetic anisotropy in FM materials.

In summary, Chapter 2 concluded the thin film growth techniques and mechanisms for complex oxides as well as the thin film characterizations including film quality, crystal structure and functional properties that have been measured and discussed in the following chapters.

Chapter 3

Strain- and thickness-dependent magnetic properties of epitaxial $La_{0.67}Sr_{0.33}CoO_3/La_{0.67}Sr_{0.33}MnO_3$ bilayers

3.1 Introduction

Over the past few decades, extensive research has been conducted on transition-metal oxides with the *ABO_3* perovskite structure due to their fascinating electronic and magnetic properties, such as metal-insulator transitions, colossal magnetoresistance, and superconductivity [123–125]. This rich behavior arises due to interactions between the charge, orbital, spin, and lattice degrees of freedom [126]. In epitaxial thin films, lattice strain and interfacial phenomena greatly differ from those in bulk materials. Thus, tuning these parameters can be effective means to modify the electronic and magnetic properties, as well as lead to emergent phenomena which can be harnessed for next generation spintronic devices and magnetic random access memory [13,16,26,35,38,83,127,128]. For example, when ferromagnetic (FM) $La_{0.5}Sr_{0.5}CoO_3$ thin films (thickness < 30 nm) are grown under compressive strain on $LaAlO_3$ (LAO) substrates, they demonstrate an enhancement of the Curie temperature (T_c) by ~ 50 K compared to thin films grown under tensile strain on $SrTiO_3$ (STO) substrates. In another work, Liao *et al.* demonstrated that the magnetic easy axis of FM LSMO thin films grown on (110)-oriented $NdGaO_3$ (NGO) substrates could be rotated in the film plane by an angle of 90° by the insertion of one unit cell of a STO buffer layer. It is believed that this effect results from the coupling of the *BO_6* octahedra

across the interfaces of this heterostructure [13]. In addition, Kan *et al.* demonstrated that magnetic anisotropy can be tuned by controlling the oxygen coordination environment at $SrRuO_3/Ca_{0.5}Sr_{0.5}TiO_3$ interfaces [129]. The Ru-O-Ti bond angle between the corner-shared TiO_6 and RuO_6 octahedra at the interface increased as the number of $Ca_{0.5}Sr_{0.5}TiO_3$ monolayers increased, resulting in a monoclinic-to-tetragonal structural transition in the $SrRuO_3$ layer.

Interfacial phenomena have also been investigated in an all-perovskite exchange spring system composed of $La_{0.67}Sr_{0.33}CoO_3$ (LSCO) and $La_{0.67}Sr_{0.33}MnO_3$ (LSMO) layers with large and small coercivities, respectively [35,75,76,80,81]. Soft x-ray magnetic spectroscopy showed that the LSCO/LSMO interface was characterized by magnetically active Co^{2+} ions which coupled magnetically to the soft FM LSMO layer [75]. For LSCO thicknesses < 5 nm, the hysteresis loops showed only a single magnetic switching event, despite being composed of two chemically distinct layers. As the LSCO thickness (t_{LSCO}) increased, the concentration of Co^{2+} ions in the interfacial layer gradually decreased [80] and a hard LSCO layer formed below it. As a result, exchange spring behavior was observed where the hard LSCO layer biased the composite soft layer, leading to a horizontal shift of the hysteresis loops in a direction opposite of the original biasing field [75,76]. In this case, the hard/soft magnetic interface existed within the LSCO layer rather than at the LSCO/LSMO chemical interface. Such unique exchange coupling behavior provides potential applications in next generation spintronic and magnetic memory devices. In this prior work, the bilayers were grown on $(LaAlO_3)_{0.3}(Sr_2AlTaO_6)_{0.7}$ (LSAT) substrates with $a^0a^0a^0$ tilt pattern [130] where both layers exist under minimal lattice strain ($\varepsilon_{LSCO} = 0.9\%$, $\varepsilon_{LSMO} = -0.2\%$) [76], where the biaxial strain was defined as $\varepsilon = (a_{strained}-a_{bulk})/a_{bulk}$. While the effect of lattice strain on perovskite oxide thin films has been studied systematically as a function

of parameters such as film thickness and magnitude/sign of lattice mismatch [13,26,83,127,128,131], the impact of strain and octahedral tilts on interfacial phenomena in heterostructures such as the LSCO/LSMO system remains largely unexplored.

In this chapter, epitaxial LSCO/LSMO bilayers were grown on two different substrates, (110)-oriented NGO and (001)-orientated LAO substrates. NGO has orthorhombic (o) symmetry with the $a^-a^-c^+$ tilt pattern in Glazer notation [130]. The (110)-oriented NGO substrate can be redefined as a pseudocubic (pc) unit cell with slightly rectangular in-plane lattice (a_{pc}=3.855 Å, b_{pc}=3.863 Å) and c_{pc}=3.855 Å at room temperature using a $(110)_o \parallel (001)_{pc}$ and $(002)_o \parallel (100)_{pc}$ transformation [132]. Thus, this growth surface shares similar lattice constants with (001)-oriented LSAT substrate (a=b=c=3.868 Å) but offers a different octahedral tilt pattern from our previous studies [75,76,80,81]. In contrast, LAO has a rhombohedral structure with the $a^-a^-a^-$ tilt pattern and a_{pc} = 3.791 Å at room temperature [133]. The LSCO layer exists under in-plane tensile strain (0.7%) on NGO substrates but experiences compressive strain (-1.0%) on LAO substrates. In contrast, the LSMO layer is nearly un-strained (-0.1%) on NGO substrates but experiences a large compressive strain (-2.0%) on LAO substrates. Both LSCO and LSMO share the same rhombohedral $a^-a^-a^-$ tilt pattern as LAO [35,127,134], however, the lattice mismatch between the film and substrate can lead to a tetragonal distortion of the pseudocubic unit cell, as well as alter the octahedral tilt patterns observed in the films. The resulting structural differences in the LSCO/LSMO bilayers lead to notable differences in their magnetic spin/electronic structures and bulk magnetic properties. For bilayers grown on both substrates, a non-magnetic layer characterized by Co^{3+} ions existed at the LSCO/substrate interface with a thickness below 2 nm. Above this layer, magnetically active Co^{2+} ions that strongly couple to the LSMO layer were

observed below a critical LSCO thickness. This critical thickness was 2 nm and 4 nm for bilayers on LAO and NGO substrates, respectively. Above this critical thickness, the LSCO layers on LAO substrates were characterized by mixed Co^{3+}/Co^{4+} ions with soft FM properties, and both LSMO and LSCO layers displayed a strong LSCO thickness dependence. In contrast, when grown on NGO substrates, a hard FM LSCO layer was observed with mixed Co^{3+}/Co^{4+} ions and only the magnetic properties of the LSCO layer varied with LSCO thickness. These results enable us to develop a deeper understanding of the interconnected strain- and thickness-dependent magnetic and electronic properties at perovskite oxide interfaces.

3.2 Experimental Methods

Epitaxial LSCO/LSMO bilayers were deposited by pulsed laser deposition on (110)-oriented NGO and (001)-oriented LAO substrates. All layers were grown using a KrF excimer laser (λ = 248 nm), with 1.0 J/cm^2 laser energy and 1 Hz laser repetition rate. The substrate temperature was held at 700 ℃ and the oxygen pressure was 0.3 Torr. Samples were slowly cooled to room temperature in 300 Torr O_2 to ensure proper oxygen stoichiometry. The LSCO layers were grown first directly on the substrate with varying thickness, and the topmost LSMO layers had a fixed thickness of 6 nm. The growth order was determined based on our previous study that no exchange spring behavior existed when the LSMO layer was grown first, due to the quick accommodation of epitaxial strain in the LSMO sublayer [35]. Bilayers grown on NGO substrates are referred to as samples CxM6-N (x = 2 to 10, referring to the LSCO layer thickness in nm) and similarly, bilayers grown on LAO substrates are referred to as samples CxM6-L. Reference samples of a single-layer LSMO thin film with 6 nm thickness and LSCO thin films with thicknesses ranging from 2 to 10 nm were grown on both substrates.

Structural characterization was performed using resonant x-ray reflectivity (RXRR) at Beamline 2-1 of the Stanford Synchrotron Radiation Lightsource (SSRL) and high-resolution x-ray diffraction (XRD) using a Bruker D8 Discover 4-circle diffractometer. RXRR measurements were carried out at 8000 eV, as well as the Co *K*-edge (7723 eV) and Mn *K*-edge (6553 eV). The transition metal *K*-edge energies were determined by performing Kramers-Kronig transformations on the x-ray absorption near edge structure energy spectra and correspond to energies where the real part of atomic scattering factor, *f'*, is a minimum. As a result, the RXRR spectra have increased sensitivity to the chemical contrast between all the deposited layers and substrates which have similar densities [104]. An off-resonant measurement with 8000 eV was also taken due to the similar energy to Cu-K_α x-rays which are widely used in lab diffractometers. The thickness, roughness, and density of each layer was determined by fitting the RXRR profiles using GenX software [103] and the strain states of the layers were obtained by reciprocal space maps (RSM) and by fitting the XRD curves using Leptos software [135].

Bulk magnetic properties were investigated at 80 K using the vibrating sample magnetometer (VSM) of a Quantum Design VersaLab system. The magnetic field was applied along the in-plane $[100]_{pc}$ direction for samples on LAO substrates and along in-plane $[001]_o$ direction for samples on NGO substrates. The diamagnetic background from the LAO substrates and large paramagnetic background from the NGO substrates were subtracted from the raw data. The magnetization of the bilayers was normalized by the surface area and reported as areal magnetization (emu/cm^2). Soft x-ray absorption (XA) and x-ray magnetic circular dichroism (XMCD) spectra were acquired at the Co and Mn *L*-edges at 80 K using Beamline 4.0.2 of the Advanced Light Source (ALS) in total electron yield (TEY) and luminescence yield (LY) modes.

Due to the finite escape depth of secondary electrons, TEY mode is most sensitive to the top 5-10 nm of the sample surface, and therefore probes the entire LSMO layer and only the LSCO layer at the LSCO/LSMO interface [136]. In contrast, LY mode detects the conversion of x-rays into visible light in the substrate after transmitting through the entire LSCO and LSMO layers, and thus provides the averaged information through the whole film thickness [117]. XMCD spectra were calculated as the difference between two jointly normalized XA spectra collected with right (I_{RCP}) and left (I_{LCP}) circularly polarized x-rays [119]. Specifically, I_{RCP} and I_{LCP} were scaled by a constant value (α) so that their averaged spectrum spans the range 0 to 1; then XMCD intensities were calculated as $\alpha(I_{RCP} - I_{LCP})$. Note that this convention yields XMCD intensity values ~2 times that of asymmetry values calculated as $(I_{RCP} - I_{LCP})/ (I_{RCP} + I_{LCP})$. In these measurements, a 0.3 T magnetic field was applied parallel to the incident X-ray beam which was 60° from the surface normal with its in-plane projection parallel to the $[100]_{pc}$ direction for bilayers on LAO substrates and along in-plane $[001]_o$ direction for bilayers on NGO substrates. It should be noted that for bilayers grown on NGO substrates, the Co- and Mn-edge XMCD LY spectra are not reported due to the extremely low luminescence yield [137].

3.2 Results and Discussion

A. Structural characterization

Figure 3.1 (a) shows the RXRR curves for bilayer C8M6-L as an example and **Table 3.1** lists the parameters derived from the best fits. The three spectra were fit simultaneously to one structural model. A thin carbon capping layer was added to the fitting model due to sample exposure to x-rays in air. The layer thickness, roughness, and scattering length density (SLD) were determined by fitting the RXRR spectra using the GenX program. These best fits indicate that the LSMO

and LSCO layers are better represented as two distinct layers which sum to the expected total thicknesses. The interface/surface layers have slightly lower density than the main layers and the interfacial roughness is below 6 Å. The fitting results agree with our previous studies on LSCO/LSMO bilayers [75,80,81].

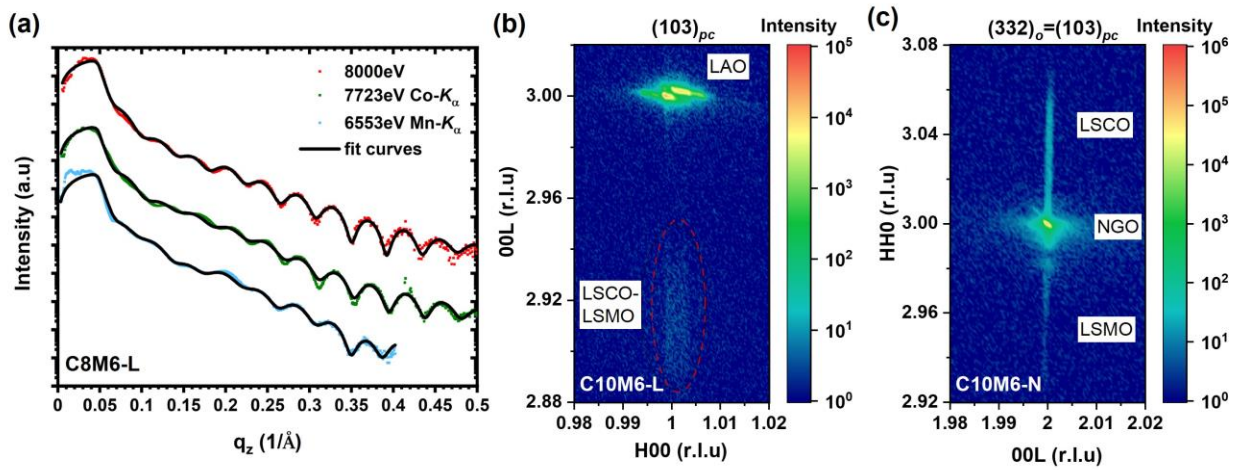

Figure 3.1 (a). RXRR spectra for bilayer C8M6-L. Colored symbols are experimental data and black curves are fits corresponding to the parameters listed in **Table 3.1**. RSMs for bilayer C10M6 on (b) LAO substrates (film peaks are marked with the red dotted circle) and (c) NGO substrates around the $(103)_{pc}$ reflections.

Table 3.1 Fit parameters for XRR spectra for bilayer C8M6-L

Layer	Thickness (nm)	Roughness (nm)	Co-edge SLD (10^{-6} Å^{-2})	Mn-edge SLD (10^{-6} Å^{-2})
Carbon layer	2.38	0.52	11-0.008i	9-0.1i
LSMO surface	2.41	0.54	47-4i	42-5i
LSMO	3.95	0.39	47-4i	44-5i
LSCO interface	3.13	0.57	47-4i	49-4i
LSCO	5.14	0.50	48-5i	50-5i
LAO	-	1.38	As bulk	As bulk

Figure 3.2 (a) and (b) show XRD ω-2θ scans taken around the $(002)_{pc}$ LAO and $(220)_o$ NGO substrate peaks, respectively. Due to the twin structure [138] of the LAO substrate, the overall film quality is slightly degraded compared to the bilayers grown on the NGO substrates. With the pseudocubic transformation, the NGO $(220)_o$ peak corresponds to a $(002)_{pc}$ peak. LSCO and LSMO layers are under compressive strain on LAO substrates, therefore, both layers appear at lower 2θ angles compared to the substrate peak. On NGO substrates, the LSMO layer exists under compressive strain while the LSCO layer is under tensile stain, so the film peaks appear on either side of the NGO substrate peak. Due to the overlap between the two film peaks and the substrate peak, it is difficult to denote clear film peak positions and thus the full ω-2θ scans were fit using Leptos software [135]. The fit curves are shown in black and the calculated *c/a* ratios are plotted in the insets. The fitting results show that the tetragonal distortion (quantified as *c/a* ratios) for the LSCO and LSMO layers on LAO substrates are $(c/a)_{LSCO}$=1.03 and $(c/a)_{LSMO}$=1.05, respectively, and neither change appreciably with LSCO thickness. This $(c/a)_{LSMO}$ value is in good agreement with literature data for a single layer LSMO film on LAO substrate [139]. On NGO substrates, $(c/a)_{LSMO}$ varies between 1.01 and 1.015, which is slightly larger than the value reported for a single layer LSMO film ($(c/a)_{LSMO}$ = 1.005 [140] and 1.01 [26]). This result suggests that the presence of both the NGO substrate and the underlying LSCO layer affect the octahedral tilt pattern/angles and tetragonal distortion of the LSMO layer [35]. For the LSCO layer, the $(c/a)_{LSCO}$ value for the thicker bilayers matches well with that of a single layer LSCO film, and a trend of lattice expansion is observed for the thinner bilayers.

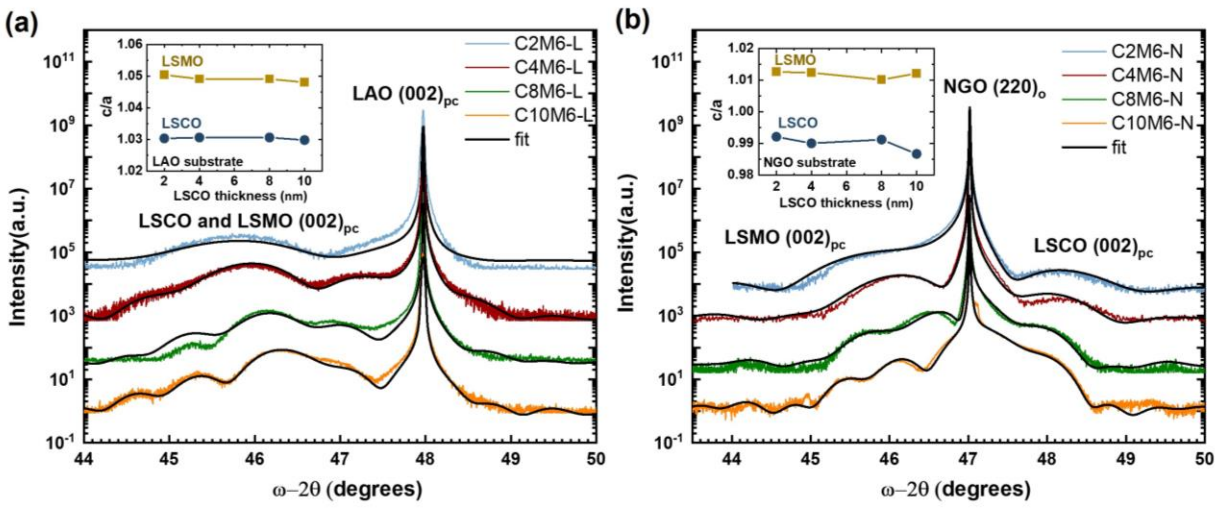

Figure 3.2 XRD ω-2θ scans of bilayers on (a) LAO substrates and (b) NGO substrates. Fit curves are shown in black. Curves are vertically shifted for clarity. The inset figures show *c/a* ratios of the LSCO and LSMO layers vs. t_{LSCO}.

B. Bulk magnetic properties

The magnetic properties of the LSCO/LSMO bilayers with varying LSCO thickness grown on LAO and NGO substrates are plotted in **Figure 3.3** (a) and (b). All bilayers on LAO substrates [**Figure 3.3** (a)] do not show distinct magnetic switching events despite the fact that distinct chemical layers were confirmed by the XRD and RXRR measurements. It should be noted that VSM bulk magnetic hysteresis loops may not clearly distinguish between two FM layers switching independently with similar coercivity. Starting with bilayer C4M6-L, the coercive field (H_c) of the bilayers gradually increases with increasing LSCO layer thickness (0.073 T for bilayer C2M6-L, 0.025 T for bilayer C4M6-L, 0.061 T for bilayer C8M6-L, 0.078 T for bilayer C10M6-L). These H_c values are smaller than single layer LSCO films on LAO substrates (0.03T for C4-L, 0.14T for C8-L and 0.16T for C10-L) and slightly larger than the single layer LSMO

film (0.013T for M6-L) as shown in **Figure 3.4**. The areal saturation magnetization (M_s) (as shown in **Figure 3.5** (a)) as well as the loop squareness (defined as remanent magnetization, M_r, divided by M_s, as shown in **Figure 3.5** (b)) for the thicker bilayers increase with LSCO thickness, though these increases are not systematic. Bilayer C2M6-L is an outlier with an areal M_s similar to that of bilayer C10M6-L despite its smaller LSCO thickness, suggesting a higher magnetic moment of its FM ions. Furthermore, the C10M6-L hysteresis loop shows an additional hard phase component compared to bilayer C2M6-L despite their similar H_c values.

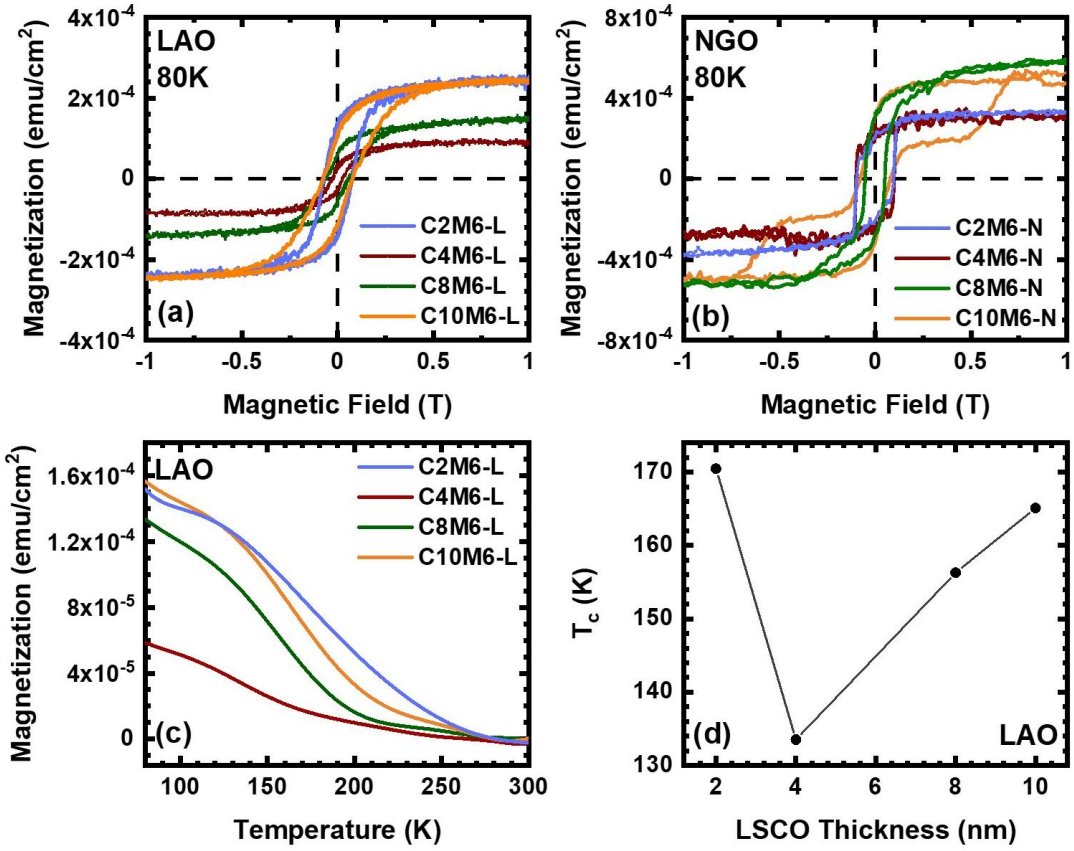

Figure 3.3 Magnetic hysteresis loops for LSCO/LSMO bilayers with varying t_{LSCO} grown on (a) LAO and (b) NGO substrates. (c). *M(T)* curves for bilayers on LAO substrates upon warming process after 800 Oe field cooling. (d). Curie temperature as a function of t_{LSCO} for bilayers on LAO substrates.

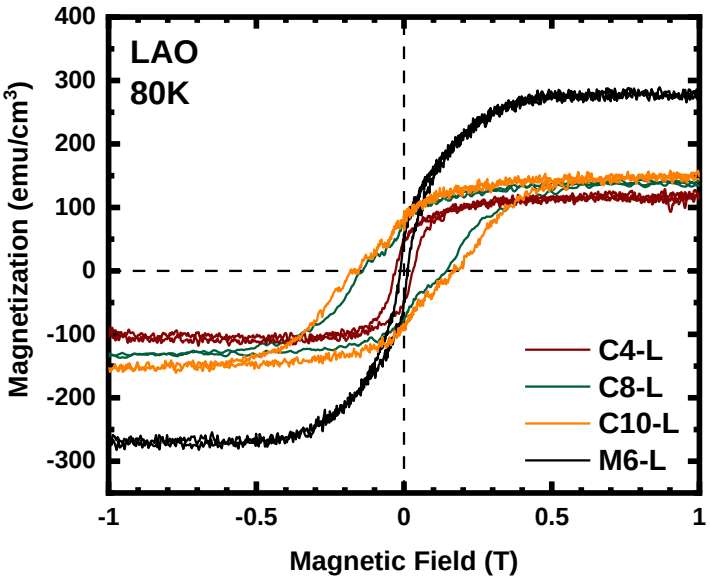

Figure 3.4 Magnetic hysteresis loops of single layer LSCO (4-10 nm) and 6 nm LSMO film on LAO substrates measured at 80 K. The applied magnetic field is parallel to the thin film surface.

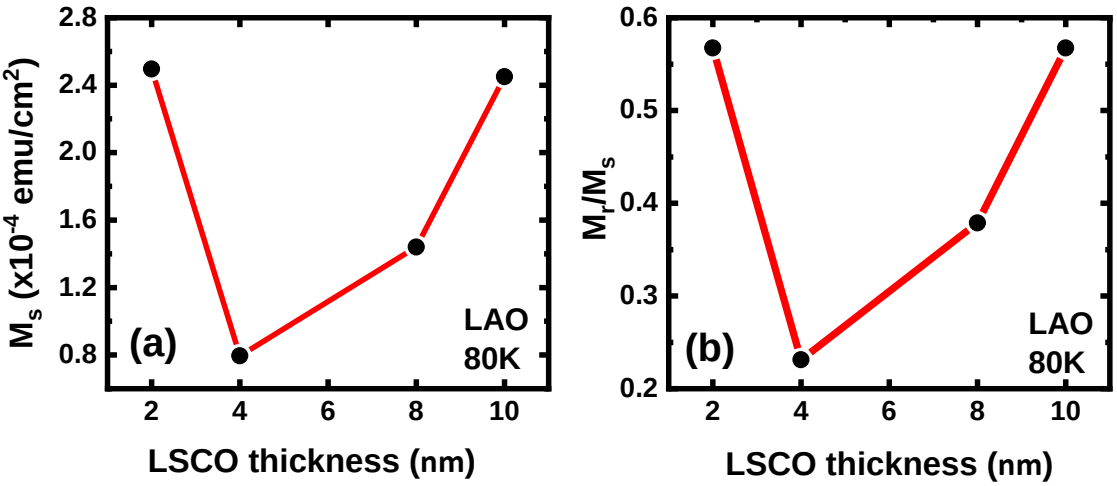

Figure 3.5 (a). M_s and (b). M_r/M_s of LSCO/LSMO bilayers on LAO substrates as a function of t_{LSCO}.

The LSCO/LSMO bilayers grown on NGO substrates [**Figure 3.3** (b)] display a different trend in their magnetic properties with increasing LSCO thickness. Bilayers C2M6-N and C4M6-N show

a single magnetic switching event with almost identical hysteresis loops with large loop squareness (M_r/M_s=0.86) despite the difference in LSCO thickness. This result suggests that the two thinner bilayers share the same magnetocrystalline anisotropy. Two magnetic phases with differing H_c values can be observed in the hysteresis loops for the thicker bilayers C8M6-N and C10M6-N, indicating a combination of soft and hard FM phases. The H_c value of the hard phase increases with increasing LSCO thickness. For bilayer C10M6-N, the hard magnetic switching event at 0.5 T corresponds well with the coercivity of single layer LSCO films with comparable thickness [82], while for bilayer C8M6-N, H_c(LSCO) is only slightly larger than H_c(LSMO). It should be noted that bilayers C8M6-N and C10M6-N share a common value of areal M_s, despite the difference in LSCO thickness.

Magnetization vs. temperature (*M(T)*) curves of bilayers on LAO substrates are shown in **Figure 3.3** (c). These curves were measured upon warming in an applied magnetic field of 800 Oe after field cooling at 800 Oe and the Curie temperature (T_c) was determined from the *M(T)* curves at the peak in *dM/dT*. The relationship between T_c and LSCO thickness for bilayers on LAO substrates are plotted in **Figure 3.3** (d). Despite the fact that distinct chemical and magnetic layers were confirmed (as discussed further below), only one dominant T_c value can be determined from the *M(T)* curves. This behavior may result from to the large magnetic field (H = 800 Oe) used to align the hard LSCO sublayers upon warming [141]. Interestingly, bilayer C2M6-L shows the largest T_c value despite having the thinnest LSCO thickness, which suggest different interfacial phenomena from the thicker bilayers. For thicker bilayers, an increasing trend of T_c values can be seen, following the trend of literature results for $La_{0.5}Sr_{0.5}CoO_3$ thin films [131]. These T_c values for the LSCO/LSMO bilayers are lower than the values for bulk

LSCO [2] and LSMO [110]. Due to the large paramagnetic signal of the NGO substrates, T_c values were not acquired for those bilayers.

C. Soft x-ray magnetic spectroscopy

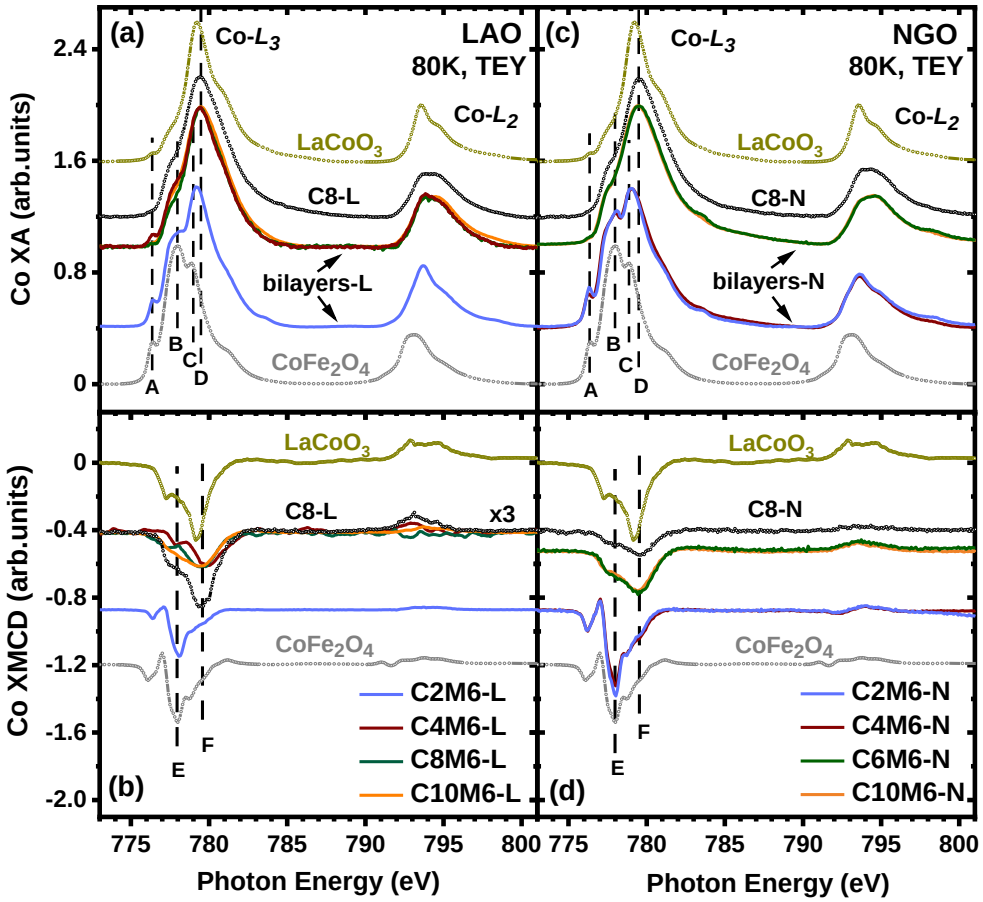

Figure 3.6 Co *L*-edge XA/XMCD spectra of (a) and (b) bilayers on LAO substrates and (c) and (d) bilayers on NGO substrates taken in TEY mode (interfacial region). Labels A-F denote prominent spectral features. Thicker bilayers and C8-L in (b) are multiplied by a factor of 3. XA/XMCD spectra are normalized to the L_3-edge average XA peak and are vertically shifted for clarity. Reference spectra for LSCO (8 nm), $LaCoO_3$, and $CoFe_2O_4$ thin films taken in TEY mode are included for comparison.

To further investigate the origin of the different magnetic characteristics of the LSCO/LSMO bilayers on LAO and NGO substrates, Co/Mn *L*-edge XA/XMCD measurements were performed. From these measurements, information about the valence states and bonding configurations of individual transition metal ions can be obtained. **Figure 3.6** (a) and (c) compare Co *L*-edge XA spectra of bilayers on LAO and NGO substrates in TEY mode. TEY mode is most sensitive to the top 5-10 nm of the sample surface, therefore primarily probes the Co ions at the LSCO/LSMO interface as the signal from the bottom LSCO layer is exponentially diminished. Reference spectra from $CoFe_2O_4$, $LaCoO_3$, and a single layer (8 nm) LSCO film (C8-L and C8-N) were plotted for comparison to Co^{2+} ions, Co^{3+} ions, and mixed valence Co^{3+}/Co^{4+} ions, all in octahedral coordination. A magnetic $LaCoO_3$ spectra was used as a reference because epitaxial $LaCoO_3$ thin films display FM properties at 80 K when Co^{3+} ions are primarily in the intermediate-spin state [108,142]. Labels A, B, and C denote prominent features in the Co^{2+} ion reference spectra and label D marks the Co-L_3 peak position of LSCO reference spectra. Thicker bilayers (LSCO $\geq$ 4 nm) grown on LAO substrates have almost the same XA curve shape and peak positions [Fig. 4(a)], indicating similar Co ion valence state and bonding configuration regardless of LSCO thickness. Furthermore, these XA curves show only subtle differences from the single layer LSCO reference curve (C8-L), suggesting that the Co ions are predominantly in mixed Co^{3+}/Co^{4+} valence states. Bilayer C2M6-L displays prominent spectral features associated with Co^{2+} ions (labeled as features A-C). However, the Co-XA spectra measured in LY mode [**Figure 3.7** (a)] shows that bilayer C2M6-L more closely resembles the LSCO reference spectra, suggesting that the Co^{2+} ions are located at the LSCO/LSMO interface while the mixed Co^{3+}/Co^{4+} ions are closer to the substrate interface. For bilayers on NGO substrates, a similar trend is observed however, the transition from predominantly Co^{2+} ions to mixed Co^{3+}/Co^{4+} ions

occurred for LSCO thickness above 4 nm, a value which approaches the critical thickness (~ 8 nm) for bilayers grown on LSAT substrates [76,80].

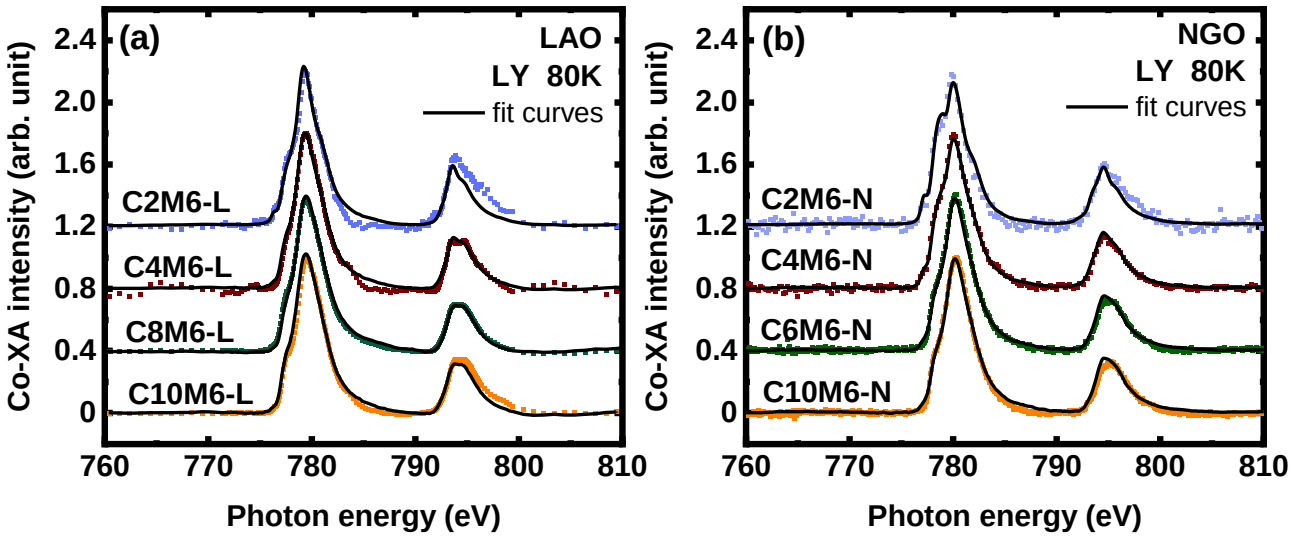

Figure 3.7 Co-XA spectra (LY) fitting of LSCO/LSMO bilayers on (a) LAO substrates and (b) NGO substrates. Spectra are vertically shifted for clarity.

The shapes of XA spectra depend on the surrounding crystal field [22] as well as spin and valence states [115]. A linear combination of the Co^{2+}, Co^{3+} and mixed Co^{3+}/Co^{4+} ions reference spectra was used as a first order approximation to simulate the experimental Co *L*-edge XA spectra for a discussion of the valence states of Co ions (**Figure 3.7** (LY mode) and **Figure 3.8** (TEY mode)). The fitting coefficients of the reference spectra vs. LSCO thickness are plotted in **Figure 3.9**. For the bilayers grown on LAO and NGO substrates, a few general trends can be observed: (1) the LY spectra consistently show a higher proportion of Co^{3+} ions compared to the TEY spectra, suggesting that these Co^{3+} ions reside primarily at the LSCO/substrate interface; (2) the proportion of Co^{3+} ions is consistently higher for the bilayers grown on LAO substrates compared to NGO substrates; (3) both TEY and LY spectra show a tradeoff between the

concentration of Co^{2+} ions and mixed Co^{3+}/Co^{4+} ions with increasing LSCO thickness; and (4) the TEY spectra show that the Co^{2+} ions in the thinner bilayers are predominantly located at the LSCO/LSMO interface.

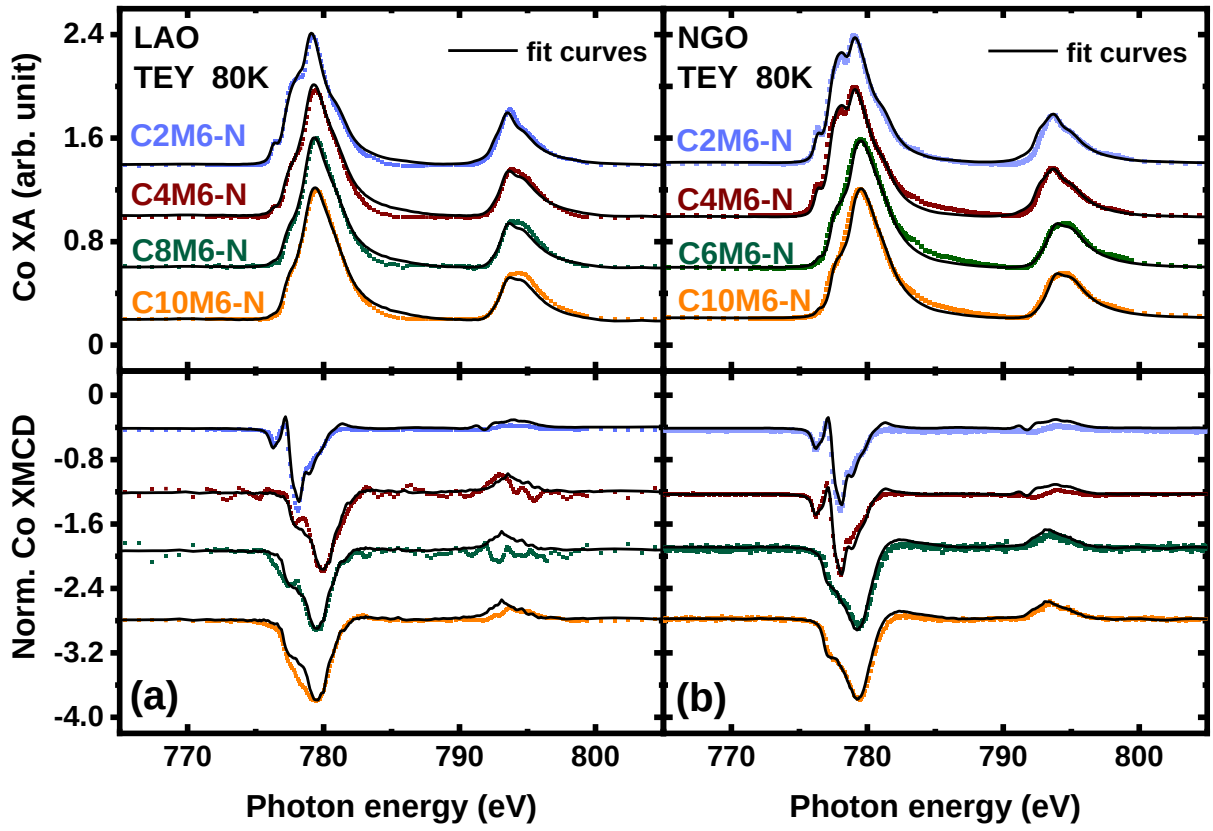

Figure 3.8 Co-XA/XMCD spectra (TEY) fitting of LSCO/LSMO bilayers on (a) LAO substrates and (b) NGO substrates. Spectra are vertically shifted for clarity.

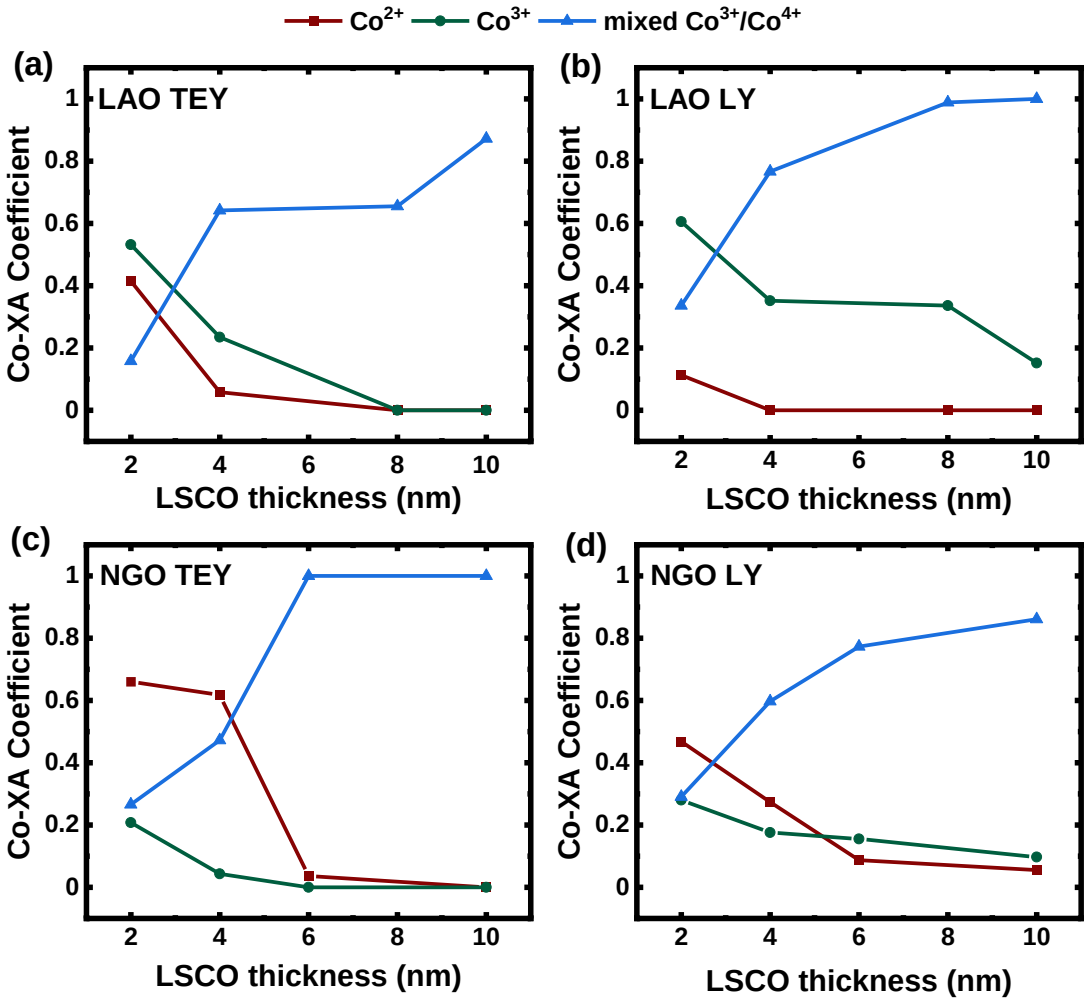

Figure 3.9 Co-XA fitting coefficients vs. LSCO thickness. (a-b) TEY and LY mode Co-XA fitting coefficients of bilayers on LAO substrates. (c-d) TEY and LY mode Co-XA fitting coefficients of bilayers on NGO substrates.

The Co-XMCD spectra [**Figure 3.6** (b) and (d)] highlight the magnetically active Co ions in the bilayers. Label E denotes the maximum intensity of the Co^{2+} reference spectra, while label F denotes the peak in the Co^{3+}/Co^{4+} ion reference spectra. For the spectra of bilayers (except for C2M6-L) grown on LAO substrates and C8-L reference spectra [**Figure 3.6** (b)], the intensities

are multiplied by a factor of 3 to show the features more clearly. The thicker bilayers on both LAO and NGO substrates closely resemble the shape of single layer LSCO reference spectra, indicating that the magnetically active ions are in a mixed Co^{3+}/Co^{4+} state while the thinner ones are similar to the Co^{2+} reference spectra. Moreover, the XMCD signal of Co^{2+} ions is much stronger than mixed Co^{3+}/Co^{4+} ions, which can be explained by the high spin state of Co^{2+} in octahedral coordination [24,81]. This result is consistent with our previous studies on LSCO/LSMO bilayers on LSAT substrates which showed that the interfacial Co^{2+} ions have larger magnetization than that of bulk LSCO when the LSCO thickness is below a critical value [81]. This fact also supports the result of the hysteresis loops shown in **Figure 3.3** (a) where bilayer C2M6-L has almost the same areal M_s as bilayer C10M6-L (similarly, C2M6-N has almost the same areal M_s as bilayer C4M6-N). The presence of oxygen vacancies has been reported in $La_{1-x}Sr_xCoO_{3-\delta}$ thin films grown on NGO and LAO substrates [127,128,143], and as a consequence can lead to the formation of magnetically active Co^{2+} ions with larger ionic radii [81]. The c-lattice expansion observed in **Figure 3.2** can be explained by the existence of these Co^{2+} ions. The TEY Co-XMCD fitting coefficients (**Figure 3.10**) show a step-like LSCO thickness dependence with magnetic Co^{2+} ions dominating for LSCO thickness $\leq$ 2 nm for LAO substrate (LSCO $\leq$ 4 nm for NGO substrate), becoming mixed Co^{3+}/Co^{4+} ions in the thicker bilayers. In addition, no magnetic contribution from Co^{3+} ions was found regardless of LSCO thickness and substrate type. Combining with the fact from XA spectra fitting results (**Figure 3.9**) that Co^{3+} ions exist at the LSCO/substrate interface, we suggest the existence of a non-magnetic layer at the LSCO/substrate interface due to magneto-electronic phase separation (MEPS) [38,82,144]. The thickness of this MEPS layer was found to be below 2.3 nm for $La_{0.5}Sr_{0.5}CoO_3$ films on LAO substrate [128] and it increased with decreasing Sr-doping and

increasing epitaxial strain [38,82]. The fact that robust magnetic properties are observed for bilayers with LSCO thicknesses below this critical thickness for MEPS suggests that the formation of Co^{2+} ions at the LSCO/LSMO interface is able to overpower MEPS at the LSCO/substrate interface. Furthermore, this MEPS layer can explain the larger proportion of Co^{3+} ions observed for the bilayer on LAO substrates where the LSCO layer exists under a -1% compressive strain.

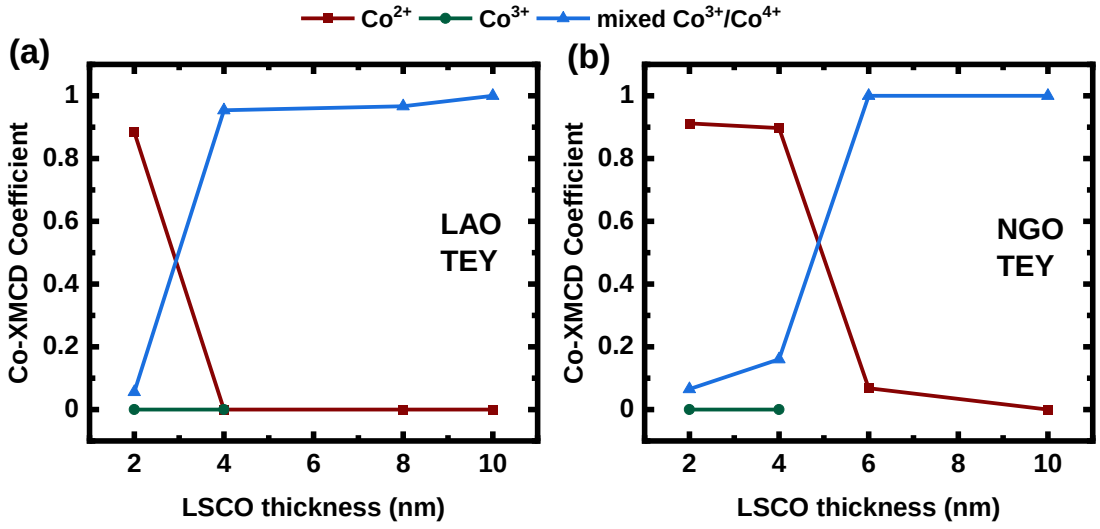

Figure 3.10 Co-XMCD fitting coefficients vs. LSCO thickness. (a) TEY mode Co-XMCD fitting coefficients of bilayers on LAO substrates. (b) TEY mode Co XMCD fitting coefficients of bilayers on NGO substrates.

As with previous studies of LSCO/LSMO bilayers grown on LSAT substrates [76,80], the Mn XA/XMCD spectral shapes and intensities for the bilayers on NGO substrates [**Figure 3.11** (c) and (d)] showed only subtle differences with increasing LSCO layer thickness and the curves

matched well with single layer LSMO films. However, the bilayers on LAO substrates [**Figure 3.11** (a) and (b)] displayed minor deviations from the behavior observed on NGO and LSAT substrates. **Figure 3.11** shows the Mn L_3-edge XA/XMCD only to clearly compare the spectral features. Labels A and B in **Figure 3.11** denote prominent features on the Mn-L_3 edge XA spectra. Among all Mn-XA curves in **Figure 3.11** (a) and (b), only the thicker bilayers (LSCO $>$ 2 nm) on LAO substrates show the shoulder feature A as well as the shifting of the main peak B to higher photon energy compared to the LSMO reference samples and bilayers on NGO substrates, indicating an increased Mn^{4+} ion concentration [145]. Unlike the bilayers grown on LSAT substrates, where a higher Mn^{4+} ion concentration was observed in the thinner bilayers due to interfacial charge transfer from (Mn^{3+} + Co^{3+}) to (Mn^{4+} + Co^{2+}) [76,80], on LAO substrates the thinnest bilayer (C2M6-L) possessed higher Mn^{3+} concentration along with the presence of Co^{2+} ions. In this case of large compressive strain, one much consider an additional contribution from the formation of oxygen vacancies which lowers the average Mn valence state in ultrathin LSMO films [146].

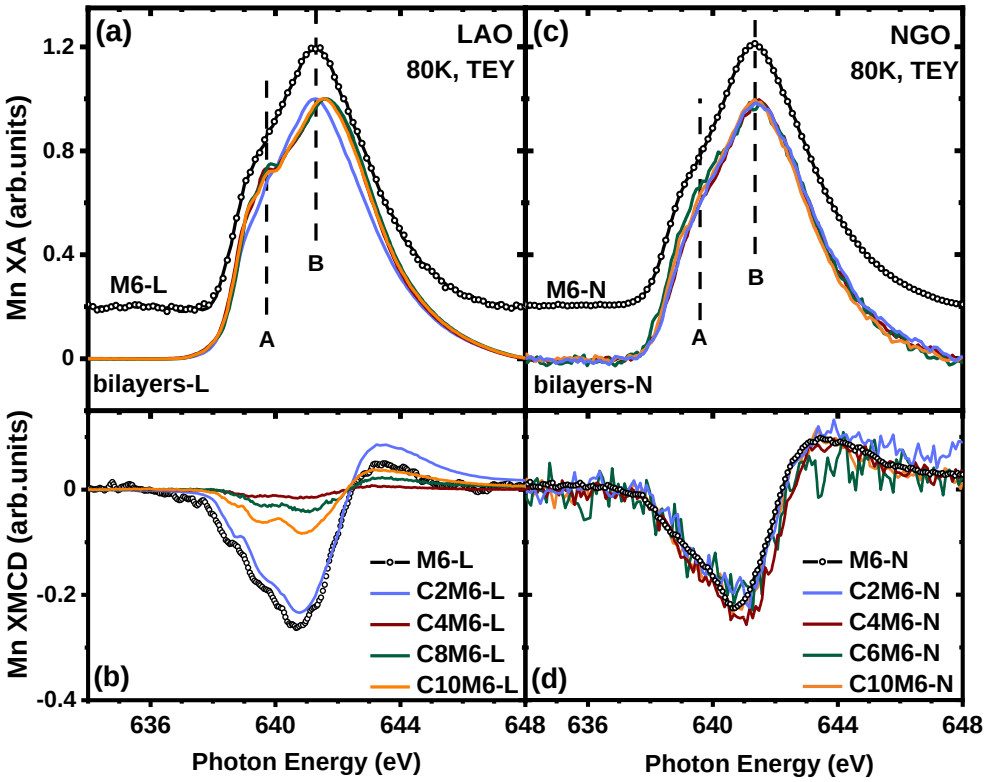

Figure 3.11 Mn L_3-edge XA/XMCD spectra of (a) and (b) bilayers on LAO substrate and (c) and (d) bilayers on NGO substrates taken in TEY mode. Labels A and B mark prominent spectral features. XA/XMCD spectra are normalized to the L_3-edge average XA peak. The M6 XA spectra are vertically shifted for clarity.

This competition between factors such as charge transfer and oxygen vacancy formation leads to a robust Mn-XMCD signal for bilayer C2M6-L. For thicker bilayers on LAO substrates, the Mn-XMCD signal is nearly absent in bilayer C4M6-L and then gradually increases with increasing LSCO layer thickness despite the fact that the LSMO thickness remains fixed at 6 nm. The maximum XMCD intensities remain much lower than that of a single layer LSMO film and bilayer C2M6-L. Previously, a trend of increasing M_s values for LSMO layers with increasing buffer layer thickness was attributed with decreased structural distortions at the buffer

layer/LSMO interface [13]. Similarly, we postulate that the epitaxial strain that builds up with increasing LSCO thickness is accommodated differently on LAO substrates (compared to LSAT and NGO substrates) as all the layers possess the same $a^-a^-a^-$ tilt pattern. A variation of octahedral tilt angles due to oxygen vacancy ordering at the LSCO/LSMO interface could explain the strong thickness dependence observed in the magnetic properties of the LSMO layer. It has been reported that the oxygen vacancy ordering directions are different when $La_{0.5}Sr_{0.5}CoO_3$ film is under tensile vs. compressive strain [128,147]. Additional characterization, such as scanning transmission electron microscopy, will be required to quantify these differences but is outside the scope of the current work.

D. XMCD hysteresis loops

Finally, Co- and Mn-edge XMCD loops of the LSCO/LSMO bilayers on LAO substrates (**Figure 3.12**) allow us to distinguish between the magnetic contributions from the two FM layers on LAO substrates, The XMCD loops were measured at specific Co/Mn-edge energies which correspond to the maximum in the XMCD spectra. Both hysteresis loops for bilayer C2M6-L [**Figure 3.12** (a)] are almost identical, indicating that the two layers are fully coupled. For thicker bilayers, the Co and Mn XMCD loops indicate that the LSCO and LSMO layers are indeed switching independently, despite the fact that the VSM bulk hysteresis loops [**Figure 3.3** (a)] do not show distinct magnetic switching events. **Figure 3.13** shows that the VSM hysteresis loop for bilayer C8M6-L (red dots) can be reproduced using a linear fit of the Co-/Mn-XMCD hysteresis loops (black curve) with a Co : Mn = 1 : 1.8 ratio of fitting coefficients. This ratio agrees well with the magnetization ratio (LSCO : LSMO = 1 : 1.5) obtained from single layer LSCO (C8-L) and LSMO (M6-L) films in **Figure 3.4**. Co-/Mn-XMCD hysteresis loops clearly

show that the H_c values increase with increasing LSCO thickness but remain below that of bilayers on NGO substrates [**Figure 3.3** (a)].

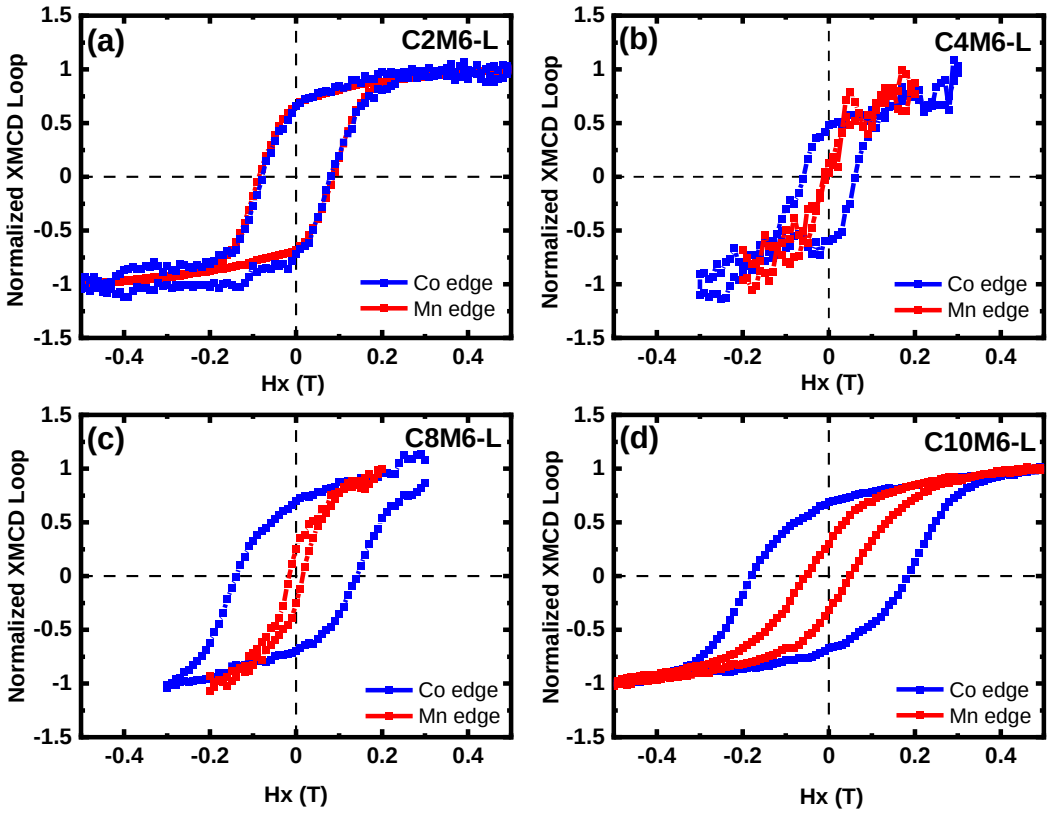

Figure 3.12 Normalized Co and Mn *L*-edge XMCD loops of LSCO/LSMO bilayers on LAO substrates. The hysteresis loops were measured at specific Co/Mn-edge energies which correspond to the maximum in the XMCD spectra.

The combination of XA/XMCD spectra and magnetic hysteresis loops suggest that both epitaxial strain and LSCO thickness strongly influence the formation of magnetic layers in the LSCO/LSMO bilayer system (see inset to **Figure 3.14**), and that interfacial charge transfer alone cannot fully explain the behavior.

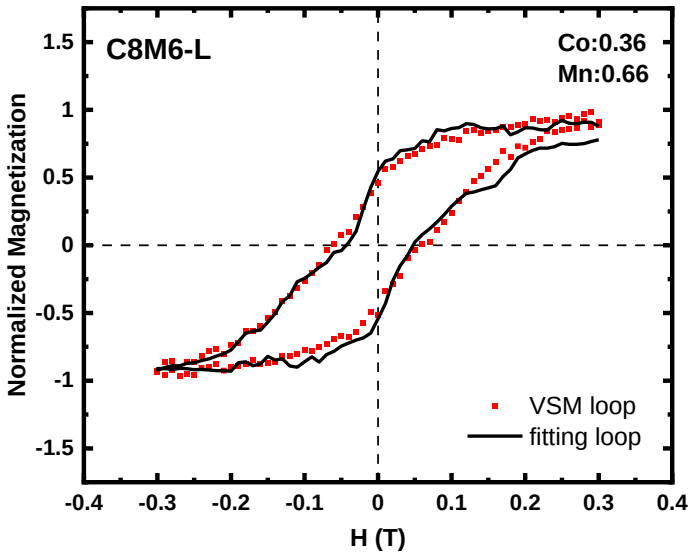

Figure 3.13 Bulk magnetic hysteresis loop of C8M6-L from VSM measurement (red dots) and the fitting loop (black curve) obtained from Co-/Mn-XMCD hysteresis loops via linear fitting method: $M_{VSM} = A * M_{Co-XMCD} + B * M_{Mn-XMCD}$, where A and B are independent fitting coefficients.

The bilayers grown on LAO substrates exist under large compressive strain and share the same bulk octahedral tilt patterns as the substrate but with differing tilt angles. In this case, the LY XA/XMCD measurements suggest the presence of a MEPS LSCO layer consisting primarily of non-magnetic Co^{3+} ions at the LAO interface. TEY measurements demonstrate that the magnetic properties of the remainder of the LSCO layer as well as the LSMO layer depend strongly on LSCO thickness. For bilayer C2M6-L, Co^{2+} ions (red triangles in **Figure 3.14**) at the LSCO/LSMO interface couple magnetically to the LSMO layer. The comparatively large M_s [shown in **Figure 3.3** (a) and triangles in **Figure 3.14** (c)] comes from robust magnetization of both LSCO and LSMO layers. For LSCO thicknesses from 4-10 nm, the concentration of Co^{2+} ions is rapidly suppressed as the LSCO thickness increases, leading to a soft LSCO layer

characterized by mixed valence Co^{3+}/Co^{4+} ions (blue triangles in **Figure 3.14**). The LSCO and LSMO layers switch independently of one another and their coercivity and magnetization values increase gradually with LSCO thickness, though even at a LSCO thickness of 10 nm, their M_s values remain suppressed below that of single layer LSCO and LSMO films on LAO substrates. Therefore, for bilayers under compressive strain, the magnetic properties of both LSCO and LSMO layers displayed a strong LSCO thickness dependence.

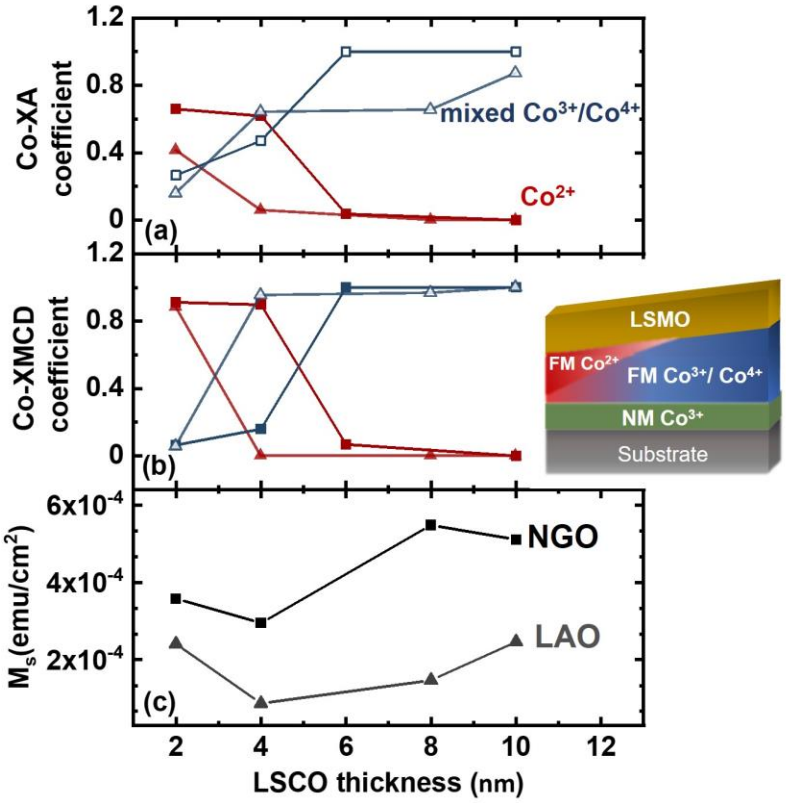

Figure 3.14 (a) Co-XA fitting coefficients and (b) Co-XMCD fitting coefficients vs. t_{LSCO} of bilayers on LAO (triangle) and NGO (square) substrates. Blue lines are for mixed valence Co^{3+}/Co^{4+} ions. Red lines are for Co^{2+} ions. (c). Areal M_s vs. t_{LSCO} of LSCO/LSMO bilayers. The inset figure shows the distribution of Co ions in the bilayers as t_{LSCO} increases (from left to right).

The bilayers grown on NGO substrates exist under mixed compressive and tensile strain and their bulk octahedral tilt patterns differ from the substrate. Though a similar evolution of Co^{2+} ions to mixed valence Co^{3+}/Co^{4+} ions (see **Figure 3.14** square symbols) was found, the critical LSCO thickness was 4 nm and the magnetic properties of the LSMO layer was largely unaffected by the change in LSCO thickness. This thickness-dependent LSCO magnetic structure is more abrupt than that found previously in bilayers on LSAT substrates, despite of the fact that the strain of the bilayers remains approximately the same on both substrates [76,80]. Therefore, we can conclude that both epitaxial strain and octahedral tilt patterns affect the magnetic properties of LSCO/LSMO bilayers, but the impact of compressive strain (when LSCO/LSMO bilayers are on LAO substrates) is more pronounced and advanced structural characterization will be needed to quantify the octahedral tilt angles and any oxygen vacancy ordering that may induced by the epitaxial strain state.

3.4 Conclusions

In summary, I investigated the strain- and thickness-dependent magnetic properties of LSCO/LSMO bilayers grown on LAO and NGO substrates. The combination of soft x-ray magnetic spectroscopy and bulk magnetometry allowed us to explore their electronic and magnetic structures. For bilayers on both LAO and NGO substrates, a non-magnetic layer characterized by Co^{3+} ions exists at the LSCO/substrate interface at thicknesses below 2 nm. As was previously found in bilayers grown on LSAT substrates, the bilayers on NGO substrates with LSCO thickness $\leq$ 4 nm showed the formation of a soft LSCO layer at the LSCO/LSMO interface characterized by magnetically active Co^{2+} ions which couple magnetically to the soft LSMO layer. With increasing LSCO thickness to 6-10 nm, the formation of the Co^{2+} ions was

quickly suppressed leaving only a hard LSCO layer with mixed valence Co^{3+}/Co^{4+} ions. However, the magnetic properties of the LSMO layer were independent of the LSCO thickness and no Mn^{4+} ions were observed. In contrast, the magnetic properties of both LSCO and LSMO layers displayed a strong LSCO thickness dependence when grown on LAO substrates. The magnetically active Co^{2+} ions predominate in bilayer with LSCO thickness = 2 nm. The strong FM signal from Co^{2+} ions and Mn ions lead to relatively larger M_s values among all bilayers on LAO substrates. An increasing trend of areal M_s values can be observed as LSCO thickness increasing from 4 – 10 nm, which follows the similar trend of increasing FM signal of Mn ions. The differences in the magnetic and electronic properties cannot be explained solely based on interfacial charge transfer and likely arise from subtle structure changes resulting from factors such as epitaxial strain states, oxygen vacancies, and octahedral tilts. These findings provide a path to tune the functional properties of complex oxide heterostructures and develop a fundamental understanding of interfacial exchange spring behavior needed for their implementation in next generation spintronic and magnetic memory devices.

Chapter 4

Tuning In-plane Magnetic Anisotropy and Interfacial Exchange Coupling in Epitaxial $La_{2/3}Sr_{1/3}CoO_3$/ $La_{2/3}Sr_{1/3}MnO_3$ Heterostructures

4.1 Introduction

Exchange bias (EB) is an effect broadly explored in ferromagnetic (FM)/antiferromagnetic (AFM) heterostructures [28,58–61] due to its promising applications in devices such as permanent magnets [62,148], spin valves [17,65], and magnetic recording read heads [66,67]. It is characterized by a horizontal shift of magnetic hysteresis loops in the direction opposite to (negative EB) [68–70] or along with (positive EB) [71–74] the biasing or field cooling direction. While it has been widely studied on FM metals and alloys, magnetic perovskite oxides provide degrees of tunability which are absent in purely metallic materials due to interactions between the charge, orbital, spin, and lattice degrees of freedom [75–78]. EB in perovskite oxides has not only been found in FM/AFM heterostructures but has also been observed at interfaces between hard and soft FM layers [75,76,80,81].

Tuning magnetocrystalline anisotropy (MA) of different layers in a heterostructure offers the potential to influence the EB effect. Among the perovskite oxides, $La_{2/3}Sr_{1/3}MnO_3$ (LSMO) has

been extensively studied due to the ability to control its MA properties [13,149,150]. For example, Liao *et al.* demonstrated the switch from interfacial magnetic anisotropy (IMA) to bulk magnetic anisotropy (BMA) of the magnetic easy axis in ultrathin LSMO layers grown on $(110)_o$-oriented $NdGaO_3$ (NGO) substrates by the insertion of an $SrTiO_3$ (STO) buffer layer [13]. Chen *et al.* further demonstrated that MA in the LSMO layer could be probed through the symmetry of the Mn 3*d* orbitals, where the $3d_{x^2-y^2}$ occupancy showed a direct relationship with in-plane anisotropy [150]. However, the EB effect could not be explored on the LSMO/STO system due to the diamagnetic properties of the STO layers. Although it has been reported that the magnetic easy axis of $La_{0.8}Sr_{0.2}CoO_3$/LSMO bilayer can be rotated from the out-of-plane to in-plane (IP) direction via ionic-liquid gating, thus simultaneously reducing and reversing the exchange bias [151], it's not clear which layer contributes to the EB effect from bulk magnetometry. In this chapter, I present a new approach of tuning the *bulk-like* LSMO (~ 6 nm) easy axis from BMA to IMA by changing the thickness of the underlying $La_{2/3}Sr_{1/3}CoO_3$ (LSCO) layer in LSCO/LSMO bilayers deposited on $(110)_o$-oriented NGO substrates and utilizing soft x-ray magnetic circular dichroism (XMCD) hysteresis loops to gain insight of the properties of each layer. This approach allows for enhanced control over the EB behavior of the LSMO layer.

In prior studies, we reported on the exchange coupling in LSCO/LSMO bilayers grown on $(LaAlO_3)_{0.3}(Sr_2AlTaO_6)_{0.7}$ (LSAT) substrates and demonstrated that exchange spring behavior was observed where the hard LSCO layer (h-LSCO) biased a composite soft layer [75,76]. This composite soft layer consisted of an interfacial soft LSCO layer (s-LSCO) characterized by magnetically active Co^{2+} ions and the LSMO layer. This s-LSCO layer arose due to the formation of oxygen vacancies and interfacial charge transfer [81], and as a result, EB effect was

only found when the LSCO thickness (t_{LSCO}) exceeded a critical thickness. Unlike the cubic-structured LSAT substrates where the substrate/film lattice mismatch is equal along the two orthogonal in-plane directions, a small difference (~0.2%) of lattice mismatch between the two in-plane directions exists in $(110)_o$-NGO substrates [152]. In Chapter 3, LSCO/LSMO bilayers on NGO substrates showed a similar Co ion distribution throughout the LSCO thickness: a non-magnetic layer characterized by Co^{3+} ions at the LSCO/NGO interface, a bulk-like h-LSCO layer with mixed Co^{3+}/ Co^{4+} ions in the middle of the layer, and a FM s-LSCO layer at the LSCO/LSMO interface [153]. Moreover, the formation of the Co^{3+}/ Co^{4+} ions was suppressed as t_{LSCO} decreased, leaving only a s-LSCO layer with strong ferromagnetism. However, the interfacial exchange coupling behavior and MA for the bilayers on NGO substrates was not explored.

In this chapter, epitaxial LSCO/LSMO bilayers were grown on $(110)_o$-oriented NGO substrates with a fixed LSMO thickness of 6 nm, and LSCO thicknesses varying from 1-10 nm. NGO has orthorhombic (o) symmetry with the $a^-a^-c^+$ tilt pattern in the Glazer notation [130] and can be redefined as a pseudocubic (pc) unit cell with a slightly rectangular in-plane lattice ($\boldsymbol{a}_{pc}$//$[001]_o$=3.855 Å, $\boldsymbol{b}_{pc}$//$[1\bar{1}0]_o$=3.863 Å, and $\boldsymbol{c}_{pc}$//$[110]_o$=3.855 Å) [152]. The LSCO layer exists under in-plane tensile strain (0.57% along the ***a***-direction, 0.78% along the ***b***-direction) on NGO substrates while the LSMO layer is under in-plane compressive strain (0.54% along the ***a***-direction, 0.34% along the ***b***-direction) on NGO substrates where the in-plane strain is defined as $\varepsilon = (a_{film}-a_{substrate})/a_{substrate}$. The BMA of LSCO and LSMO single layers on $(110)_o$-NGO substrates is along the ***a***- ($[001]_o$) and ***b***- ($[1\bar{1}0]_o$) directions, respectively, corresponding with the smaller in-plane strain induced by the substrate [152]. Based on the results of XMCD hysteresis

loops taken at the Co and Mn *L*-edges, we found that the easy axes for the LSCO layers was always aligned along the ***a***-direction regardless of t_{LSCO}. Surprisingly, the LSMO sublayer clearly saw a transition from an easy axis along the ***a***-direction for $t_{LSCO} \leq 4$ nm, to the ***b***-direction for larger t_{LSCO} values, despite the fact that the LSMO sublayer thickness remains fixed at 6 nm, suggesting the influence of a unique IMA that differs from the bulk properties. As a consequence, for $t_{LSCO} \leq 4$ nm, no EB effect was observed along the ***a***-direction, while a small negative EB shift was observed along the ***b***-direction. For $t_{LSCO} > 4$ nm, a large negative EB shift was found along both ***a***- and ***b***-directions due to the differing in-plane MA between the LSCO and LSMO layers. The preferred direction of the Mn $3d_{x^2-y^2}$ orbital occupancy was measured by element-specific x-ray linear dichroism (XLD) and correlated with the in-plane MA of the LSMO layer. Therefore, the interfacial coupling between the LSCO and LSMO layers strongly influences the IMA of the LSMO layer, enabling the control of EB between the two FM layers.

4.2 Experimental Methods

Thin Film Deposition. The LSCO/LSMO bilayers were grown on $(110)_O$-oriented NGO substrates by pulsed laser deposition from stoichiometric $La_{0.67}Sr_{0.33}CoO_3$ and $La_{0.67}Sr_{0.33}MnO_3$ targets. The LSCO layer thickness was designed to range from 1 nm to 10 nm, capped with 6 nm of LSMO, referred to as bilayers CxM6N (x = 1 – 10, corresponding to the LSCO layer thickness in nm). The chamber was pumped to a base pressure of 2 x 10^{-6} Torr then subsequently filled with flowing O_2 gas to a fixed pressure of 300 mTorr. During the deposition, the substrate temperature was held at 700 °C and a KrF excimer laser (λ = 248 nm), with 1.0 J/cm^2 laser energy, and 1 Hz laser repetition rate was used for both LSCO and LSMO layers. The bilayers were cooled to room temperature in 300 Torr O_2 at a rate of 10 °C/min to ensure proper oxygen

stoichiometry.

Structural Properties Characterization. The structural properties of the bilayers (e.g., total film thickness, interface roughness, crystallinity, and strain state) were characterized by x-ray reflectivity (XRR), high-resolution x-ray diffraction (XRD) and reciprocal space maps (RSMs) using a Bruker D8 Discover four-circle x-ray diffractometer using Cu $K_{\alpha 1}$ X-rays (λ = 1.5406 Å). The out-of-plane lattice parameters of the bilayers were obtained by fitting the XRD profiles using Leptos software [135]. Due to the similarities of the densities of LSCO and LSMO, the bilayers were further characterized using resonant x-ray reflectivity (RXRR) measurements at Beamline 2-1 of the Stanford Synchrotron Radiation Lightsource (SSRL). RXRR profiles were measured at the Co *K*-edge (7730 eV), Mn *K*-edge (6558 eV), and an off-resonance energy (8000 eV). The higher sensitivity of RXRR measurements were able to probe the structural properties of each layer in the bilayers [104]. By fitting the RXRR profiles at three energies to one structural model using GenX software [103], the thickness, roughness, and density of each layer was determined.

Magnetic Properties. Soft x-ray magnetic spectra (x-ray absorption (XA), XMCD, and XLD spectra) were acquired at the Co and Mn *L*-edges at 80 K using Beamline 4.0.2 of the Advanced Light Source (ALS) in total electron yield (TEY) mode, which probes the top 5 – 10 nm of the bilayer (corresponding to the entire LSMO layer and LSCO/LSMO interface region), limited by the escape length of secondary electrons [136]. For acquisition of the XMCD spectra, the bilayers were field cooled in 0.3 T to ensure that all magnetic moments are aligned along the field direction. During the measurements, a 0.3 T magnetic field was applied parallel to the

incident x-ray beam which was 60° from the surface normal and XA spectra were collected using right- and left-circularly polarized x-rays. XMCD spectra were calculated as the difference between two jointly normalized XA spectra collected with right (I_R) and left (I_L) circularly polarized x-rays. The XLD spectra were acquired with the x-ray beam perpendicular to the sample surface and the direction of the linear polarization vector was oriented with $\vec{E}$//$\boldsymbol{a}$ and $\vec{E}$//$\boldsymbol{b}$. The XLD spectra were calculated as the difference of the XA spectra obtained with the two linear polarization directions. Bilayers were zero-field cooled to 80 K before all XMCD hysteresis loop measurements. Unbiased Mn-XMCD hysteresis loops (**Figure 4.2** (a) – (d)) and unbiased Co-XMCD hysteresis loops for bilayer C1M6N (**Figure 4.2** (e)) were measured in TEY mode at Beamline 4.0.2 of the ALS with the magnetic field applied along the ***a***- and ***b***-directions. Unbiased Co-XMCD hysteresis loops for thicker bilayers ($t_{LSCO} \geq 4$ nm, **Figure 4.2** (f) – (h)) and biased Mn-XMCD hysteresis loops were measured at 80 K in TEY mode along the ***a***- and ***b***-directions using Beamline 6.3.1 of the ALS. For the biased hysteresis loops, the bias field was set to ± 1.8 T for 1 minute then the minor loops were measured from - 0.3 T to + 0.3 T.

4.3 Results and Discussion

The LSCO/LSMO bilayers were characterized by RXRR and the curves were fit using GenX software [103] to determine the individual layer thickness, roughness, and density parameters. RXRR curves for bilayer C4M6N are shown in **Figure 4.1** (a) as an example where all three energy spectra were fit simultaneously to one structural model and the parameters derived from the best fits are listed in **Table 4.1**. A thin carbon capping layer was added to the fitting model due to the long-time sample exposure to hard x-rays in air. Kiessig fringes can be seen in all curves, indicating that the surface/interface regions are smooth. The density of each layer at the

interface region is lower than the bulk values as listed in **Table 4.1**, suggesting the formation of oxygen vacancies at the interface [81,154,155]. The total thickness of each layer is in a good agreement with expectations and the fitting results agree with our previous studies on LSCO/LSMO bilayers [80,81].

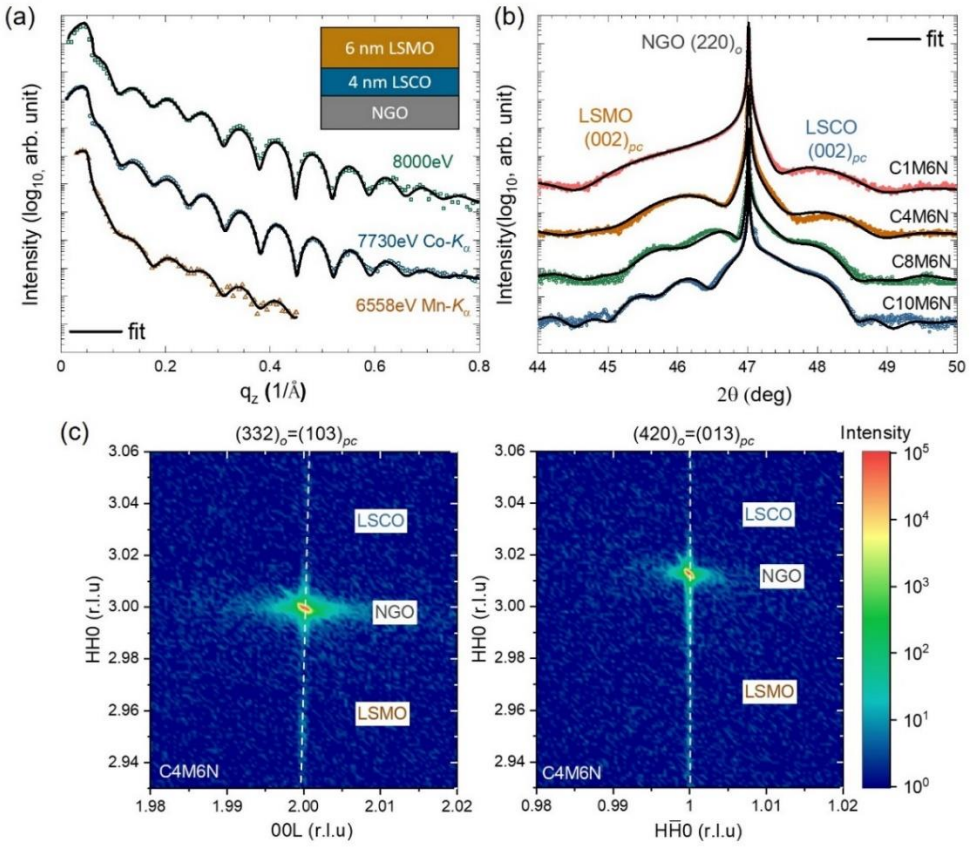

Figure 4.1 (a) RXRR spectra for bilayer C4M6N and (b) XRD 2θ scans of CxM6N (x = 1, 4, 6, 10) bilayers. Colored symbols are experimental data and black curves are fitting results corresponding to the parameters listed in **Table 4.2**. Curves are vertically shifted for clarity. (c) RSMs for bilayer C4M6N around the $(103)_{pc}$ and $(013)_{pc}$ reflections. The dashed white line marks the in-plane alignment of the film and substrate peaks.

Figure 4.1 (b) shows XRD ω−2θ scans of the LSCO/LSMO bilayers around the $(220)_o$ reflection

of the NGO substrates. Curves are vertically shifted with t_{LSCO} ranging from 1 to 10 nm. The LSMO and LSCO $(002)_{pc}$ film peaks are on the left and right side of the NGO substrate peak, respectively, due to the different strain states between the film and the substrate. Though it is difficult to denote film positions because of the overlap between the two film peaks and the substrate peak, the scans were fitted using Leptos software [135] to obtain out-of-plane lattice parameter (*c*) and *c/a* ratio of each layer. Fit curves are plotted in black and the fitting results are listed in **Table 4.1**.

Table 4.1: XRD curve fit parameters for bilayer CxM6N (x = 1, 4, 8, 10)

Bilayer CxM6N	c_{LSMO} **(Å)**	c_{LSMO}/a	c_{LSCO} **(Å)**	c_{LSCO}/a
x = 1	3.911	1.012	3.843	0.995
x = 4	3.910	1.012	3.824	0.990
x = 8	3.906	1.011	3.829	0.991
x = 10	3.909	1.012	3.811	0.987

c_{LSMO}/a values for the LSMO layer are almost the same regardless of t_{LSCO} but slightly larger than the values reported for a single-layer LSMO film on NGO substrates [26,140], suggesting that the underlying LSCO layer may affect the interfacial octahedral tilt pattern/angles of the LSMO layer on top. For the LSCO layer, an overall trend of increased c_{LSCO} is observed as t_{LSCO} decreased, which can be caused by a higher concentration of oxygen vacancies and Co^{2+} ions at the LSCO/LSMO interface [75,81] which have larger radius than Co^{3+} and Co^{4+} ions (high-spin octahedral coordinated Co^{2+}: 88.5 pm, low-spin octahedral coordinated Co^{3+}: 68.5 pm, high-spin octahedral coordinated Co^{4+}: 67 pm) [156,157]. The detailed information regarding Co ion spin and valence states will be discussed later in this article. RSMs were measured around the $(103)_{pc}$

and $(013)_{pc}$ reflections which are rotated by 90° from one another to probe the structural information along the two inequivalent in-plane directions of the orthorhombic NGO substrate. In **Figure 4.1** (c), RSMs of bilayer C4M6N is shown as an example, where vertical alignment of film peaks with substrate peak indicates that both layers are coherently-strained to the NGO substrate. Therefore, no strain relaxation was found for bilayers with t_{LSCO} up to 10 nm [153]. In addition, a small tilt is observed between the film and substrate peak locations in the $(103)_{pc}$ RSM (marked as the white dashed line), indicating that the film has bond angle deviation away from 90° along this direction. This deviation is only observed in $(103)_{pc}$ RSM meaning that this angle variation is only occurring for one of the bond angles resulting in monoclinic unit cells for the LSCO and LSMO films on NGO substrates. The observed bond angle deviation has also been reported for other perovskite films on orthorhombic substrates, such as $SrRuO_3$ films on $DyScO_3$ and $GdScO_3$ substrates [129,158]. Thus, the small tilt in RSM suggests BO_6 octahedral reconstruction at the heterostructure interfacial [127,159].

Table 4.2 Fit parameters for RXRR spectra for C4M6N bilayer

Layer	Thickness (nm)	Roughness (nm)	Density (g/cm^3)
Carbon layer	1.84	0.97	2.32
LSMO surface	2.41	0.72	6.35
LSMO interface	3.35	0.41	6.02
LSCO interface	0.93	0.47	6.47
LSCO	3.32	0.62	6.72
NGO substrate	-	0.14	7.57

To explore the in-plane MA of the LSMO and LSCO layers as the function of t_{LSCO}, *unbiased* XMCD major loops at the Mn and Co *L*-edges were acquired in TEY mode immediately after zero field cooling to 80 K. Traditional bulk magnetometry cannot separate the magnetic contributions of individual layers, however, by tuning the x-ray energies to either the Co or Mn *L*-edges enables such element-specificity from XMCD measurements. Bilayer samples were zero-field-cooled to 80 K before the measurements. **Figure 4.2** (a) – (d) plot the unbiased Mn-XMCD minor loops measured along ***a*-** and ***b*-**directions with increasing t_{LSCO} and they provide information in the inherent LSMO magnetic anisotropy while the LSCO layer is in the demagnetized state. The squareness of the major loops at Mn-edge, defined as remanent magnetization (M_r)/saturation magnetization (M_s) is plotted in **Figure 4.2** (i). The squareness values are much higher along the ***a*-**direction (about 0.9) than along ***b*-**direction when $t_{LSCO} < 8$ nm, indicating the magnetic easy axis of LSMO layer is along the ***a*** ($[001]_o$) direction. However, the in-plane MA of the LSMO layer switches to the ***b*** ($[1\bar{1}0]_o$) direction when t_{LSCO} increases to 10 nm. For t_{LSCO} = 8 nm, the loop shape and squareness along ***a*-** and ***b*-**directions are almost equal, suggesting that either the magnetic easy axis lies in between the ***a*** and ***b*** directions or both directions are energetically degenerated. The trend of M_r/M_S vs. t_{LSCO} along the two in-plane directions reveals that the magnetic properties of the LSMO layer switches from IMA to BMA at a critical t_{LSCO} of 8 nm. The t_{LSCO} - dependent in-plane MA of LSMO layer is shown schematically in **Figure 4.3**. It should be noted that the easy axis of bulk LSMO single layers on $(110)_o$-NGO substrate is along the ***b*-**direction, due to slightly smaller in-plane strain [152]. The re-orientation of the LSMO easy axis to the ***a*-**direction reveals that the strain state is no longer the dominant effect in determining the LSMO MA. We propose that the interfacial interactions between LSCO and LSMO layers plays a key role in explaining this behavior.

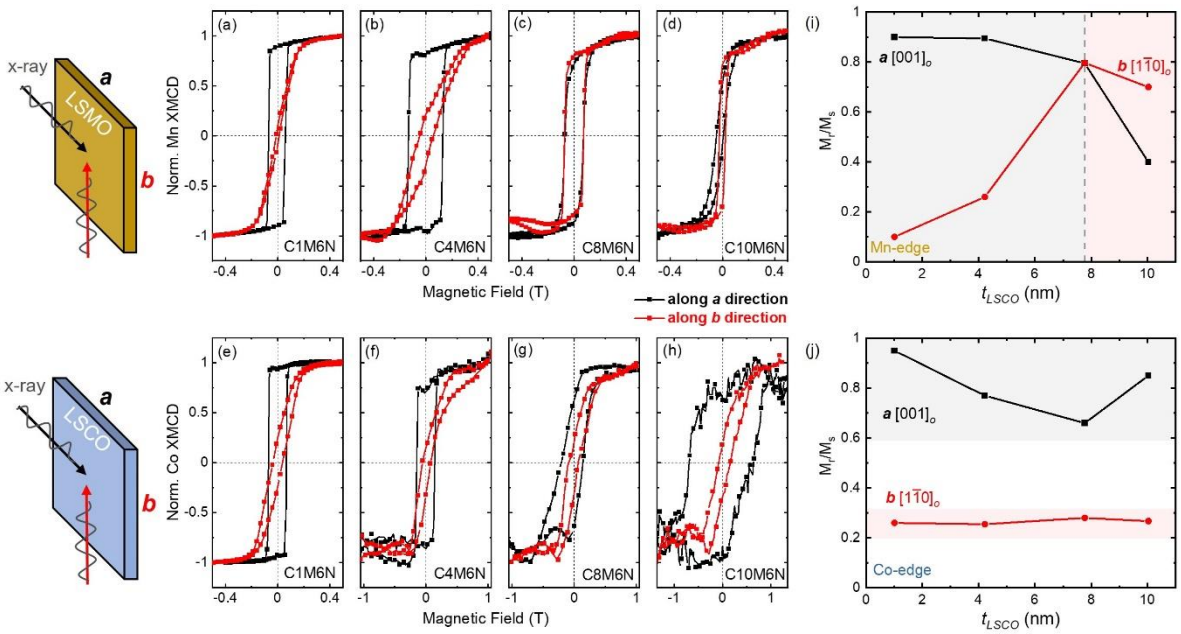

Figure 4.2 Unbiased XMCD loops acquired at the Mn *L*-edge (a) – (d) and at the Co *L*-edge (e) – (h) measured along ***a***- (black) and ***b***- (red) directions. Loops were normalized from -1 to 1. Squareness (M_r/M_s) of XMCD loops along ***a***- and ***b***- directions at the Mn-edge (i) and at the Co-edge (j) are plotted as a function of LSCO layer thickness (t_{LSCO}).

Similar unbiased XMCD major loops at the Co *L*-edge were taken along the ***a***- and ***b***-directions as shown in **Figure 4.2** (e) – (h). Note that the magnetic field range is significantly expanded for the three thicker bilayers. The squareness values of the Co-edge loops along the ***a***-direction are much larger than along the ***b***-direction regardless of t_{LSCO} as shown in **Figure 4.2** (j), suggesting that the easy axis of the LSCO layer is always along the ***a*** ($[001]_o$) direction, which is in agreement with single layer LSCO on NGO substrates. In addition, a trend of increasing H_c (LSCO) as a function of t_{LSCO} is observed (as shown in **Figure 4.4**), similar to the behavior of single layer LSCO on NGO and other substrates [82,153]. Furthermore, in bilayers C1M6N and

C4M6N, H_c (LSCO) are almost the same as H_c (LSMO) along the ***a***-direction (as shown in **Figure 4.4** (a)), indicating that the LSCO and LSMO layers are magnetically coupled when t_{LSCO} ≤ 4 nm. It has been reported that LSCO and LSMO layers were found to be fully magnetically coupled when t_{LSCO} was below a critical thickness, as indicated by a single magnetic switching event from bulk magnetometry [82,153]. This interfacial coupling results in an increase of H_c (LSMO) values shown in **Figure 4.4** compared to single layer LSMO on NGO and other substrates. Along the ***a***-direction, H_c (LSMO) = 0.13 T in bilayer C4M6N, which corresponds to an enhancement of more than 60 times when compared to the bulk value (~ 0.002 T) [160,161] and more than six times compared to the thickest bilayer C10M6N (~ 0.02 T). H_c enhancement is commonly observed in FM/AFM systems due to the pinning effect [51,162] or caused by the presence of defects in the FM sample [161], but has not been widely studied in FM/FM perovskite systems. Therefore, the modification of H_c values and change in LSMO MA through interfacial coupling could affect the EB effect on LSCO/LSMO heterostructures.

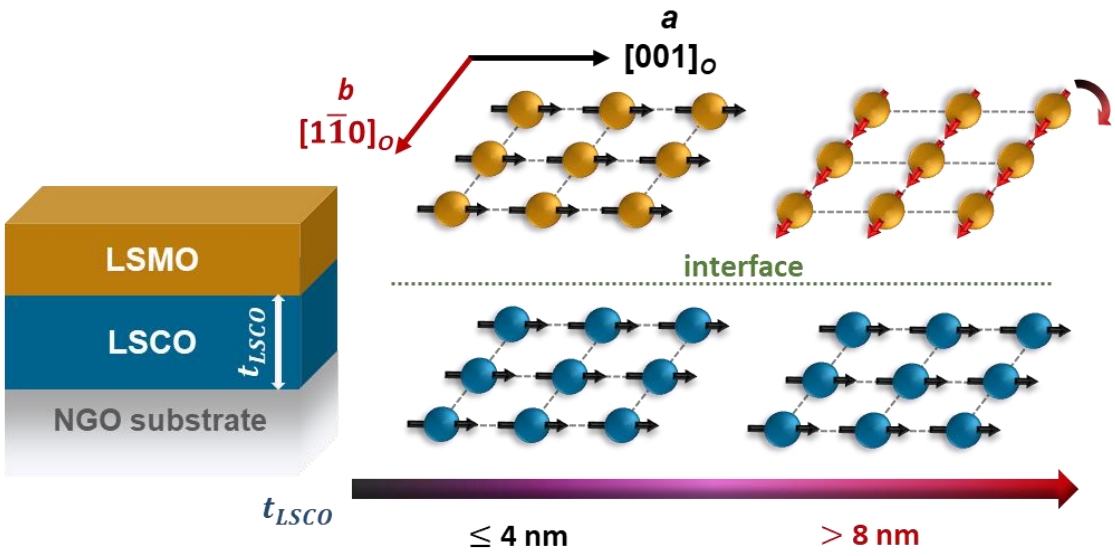

Figure 4.3 LSCO thickness (t_{LSCO}) - dependent in-plane MA in LSCO/LSMO bilayers on NGO substrates. The Mn ions are colored in yellow and Co ions are colored in blue.

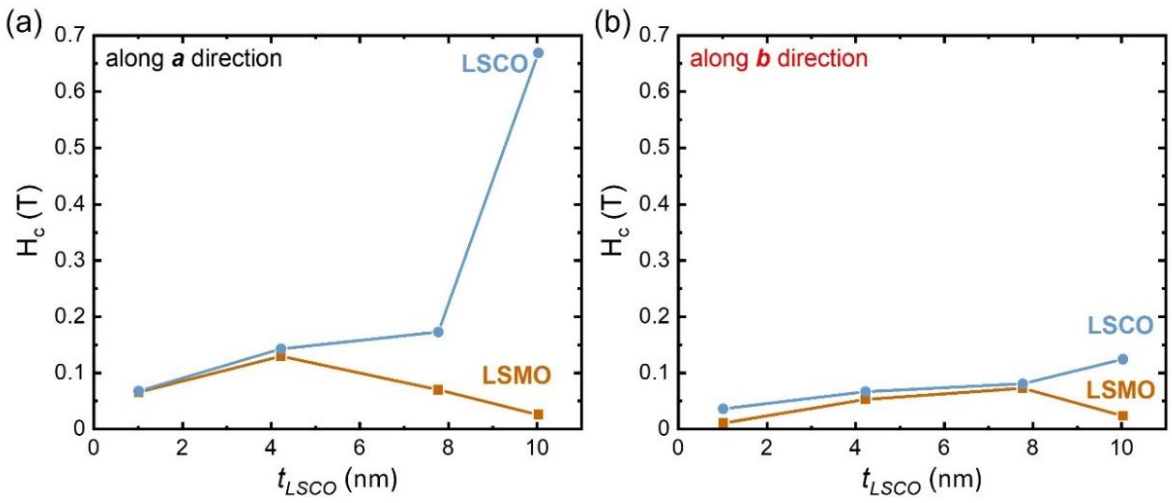

Figure 4.4 H_c as a function of t_{LSCO} derived from XMCD unbiased loops (a) along ***a*** ($[001]_o$) direction and (b) along ***b*** ($[1\bar{1}0]_o$) direction.

The exchange bias effect of the LSCO/LSMO bilayers are explored using *biased* XMCD hysteresis loops measured in TEY mode at 80 K along the ***a***- and ***b***-directions after zero-field cooling to 80 K as shown in **Figure 4.5**. Unlike in traditional FM/AFM exchanged bias systems, biasing in FM/FM systems does not require field-cooling the samples through the Néel temperature of the AFM layer but can be accomplished by magnetizing both hard and soft layers with a sufficiently large magnetic field (i.e., 1.8 T), or field cooling the sample through the Curie temperature of both layers. At the Mn *L*-edge, the bilayers were first biased at +/- 1.8 T so that both layers reach full saturation, then minor loops were measured between ± 0.3 T. **Figure 4.5** (a) – (d) plot biased XMCD minor loops at the Mn *L*-edge measured along the ***a***-direction with t_{LSCO} ranging from 1 nm to 10 nm. For $t_{LSCO} \leq 4$ nm, the absence of EB effect in bilayers C1M6N and C4M6N along the ***a***-direction, as observed by perfectly overlapping minor loops, can be attributed to the same MA and the magnetic coupling between the hard/soft FM layers.

Conversely, a small EB effect is observed along the ***b***-direction in the two thinner bilayers (shown in **Figure 4.5** (e) and (f)), caused by slightly different H_c values between the two FM layers (shown in **Figure 4.4** (b)). For bilayers with t_{LSCO} > 4 nm, a significant lateral shift of the hysteresis loops in the direction opposite to the biasing field is observed along both in-plane directions due to the different in-plane MA and larger difference in H_c values between the LSCO and LSMO layers, resulting in a large EB effect. Such behavior indicates that the magnetic moments of the soft LSMO layer are pinned by a hard FM layer, and the interfacial FM/FM exchange coupling is similar to the behavior at FM/AFM interfaces [163,164]. Unfortunately experimental limitations due to the extremely low luminescence yield of NGO substrates [153] and the finite probing depth of TEY detection mod [136], prevent us from acquiring reliable biased Co-XMCD loops from the buried LSCO layer.

The H_c values from XMCD minor loops and exchange bias field (H_{EB}) values as a function of t_{LSCO} are plotted in **Figure 4.5** (i) and (j), respectively. H_{EB} values were found to increase as a function of t_{LSCO} where H_{EB} is defined as $H_{EB} = |(H_1 + H_2)/2|$, and H_1 and H_2 are the values where the hysteresis loop intersects the left and right field axes, respectively. In EB systems, the expectation is that H_{EB} and H_c should show similar trends [165]. However, a reversed trend of H_{EB} and H_c is observed in **Figure 4.5** (i) and (j), suggesting that additional interfacial interactions must be considered. A similar decoupling of H_{EB} and H_c, and the enhancement of H_c values in LSCO/LSMO bilayers was previously reported, where the decrease in interfacial Co^{2+} ion concentration and an increase of nonmagnetic Co^{3+}/Co^{4+} ions was observed with increasing t_{LSCO} [80]. Here we propose a similar t_{LSCO} dependence of the hard/soft magnetic interfacial interactions related to the details of the Co valence states in the LSCO layer, as discussed below.

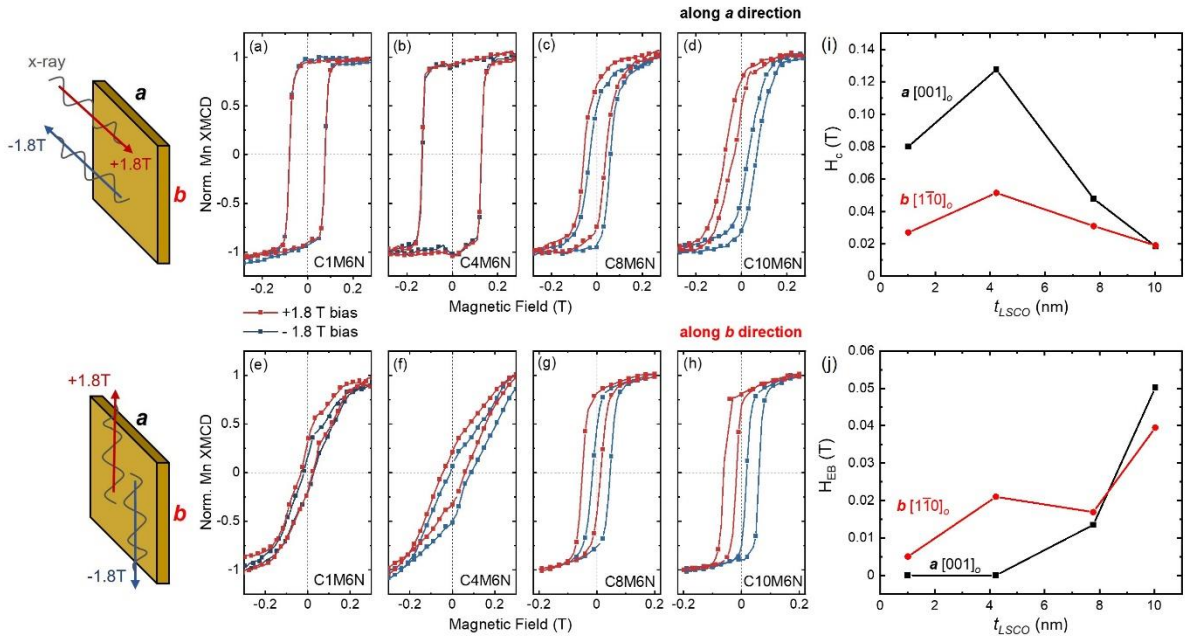

Figure 4.5 Biased XMCD minor loops acquired at the Mn *L*-edge measured along ***a***-direction (a) – (d) and along ***b***-direction (e) – (h). Loops in red and blue were measured after applying + 1.8 T field and - 1.8 T field, respectively. Loops were normalized from -1 to 1. H_c values of biased loops in (i) and EB field (H_{EB}) in (j) as a function of LSCO layer thickness (t_{LSCO}) along ***a***- and ***b***-directions.

Co ion valence states and bonding configurations in the bilayers were probed by Co *L*-edge XA spectra as shown in **Figure 4.6**. Averaged XA spectra were normalized from 0 to 1. XMCD spectra were calculated as the difference between two jointly normalized XA spectra collected with right (I_R) and left (I_L) circularly polarized x-rays. Reference spectra from $CoFe_2O_4$ (Co^{2+}) and a single-layer LSCO film (mixed Co^{3+}/Co^{4+}), both in octahedral coordination, were plotted in **Figure 4.7** for comparison to the bilayer spectra. The Co-XA spectra of bilayer C1M6N shown in **Figure 4.6** (a) reveals that the Co ions are predominantly Co^{2+} ions. For the thickest bilayer C10M6N, the Co-XA curve fully assembles the single-layer LSCO reference spectra

where mixed Co^{3+}/Co^{4+} ions dominate as shown in **Figure 4.6** (d). In addition, several general trends can be observed: (1) As t_{LSCO} increases to 8 nm, the pre-peak intensity (shaded in pink color) decreases and fully disappears when t_{LSCO} = 10 nm; (2) The intensity ratio of the doublet peak (marked with "▼") reduces as t_{LSCO} increases from 1 to 4 nm; (3) The Co-L_3 peak positions shift to higher energies as t_{LSCO} increases. These gradual changes in XA spectral shape indicate that the valence state of Co ions is gradually changing from Co^{2+}-dominated to mixed Co^{3+}/Co^{4+}-dominated with increasing t_{LSCO}, which is consistent with the results in previous work. [76,81,153] This t_{LSCO} dependence again supports the result of decoupling of H_{EB} and H_c, and the enhancement of H_c values in the LSMO layer as shown in **Figure 4.5** [80].

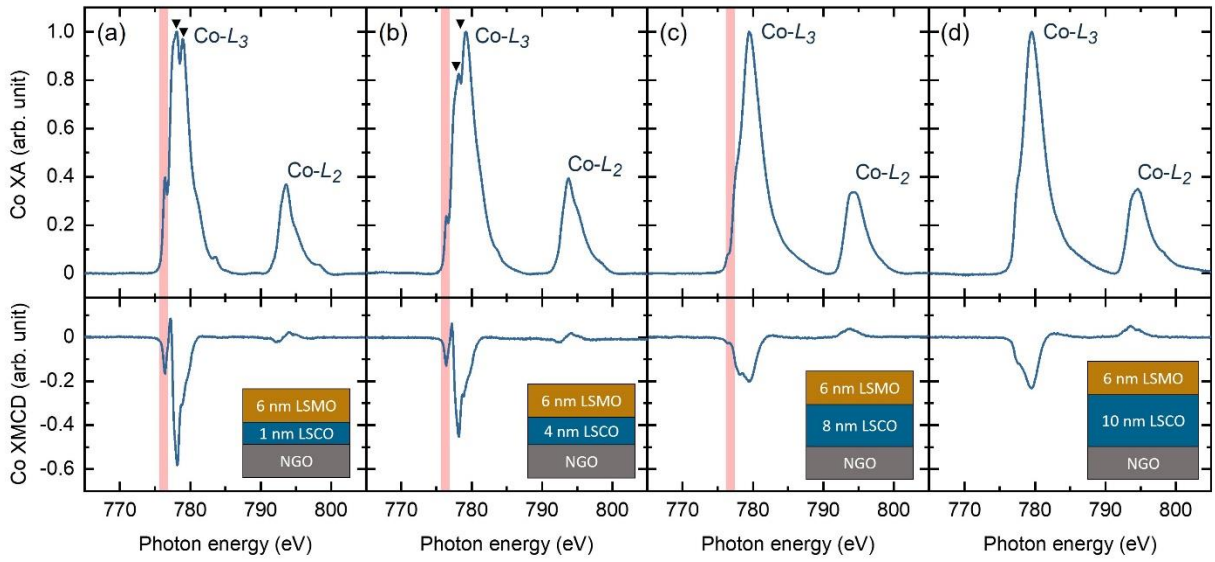

Figure 4.6 (a) – (d) Co *L*-edge XA/XMCD spectra of CxM6N (x = 1, 4, 8, 10) bilayers taken in TEY mode (interfacial region). XA spectra are normalized from 0 to 1. Pre-peak features are shaded with pink color while "▼" symbols represent the main L_3 peaks associated with Co^{2+} ion features.

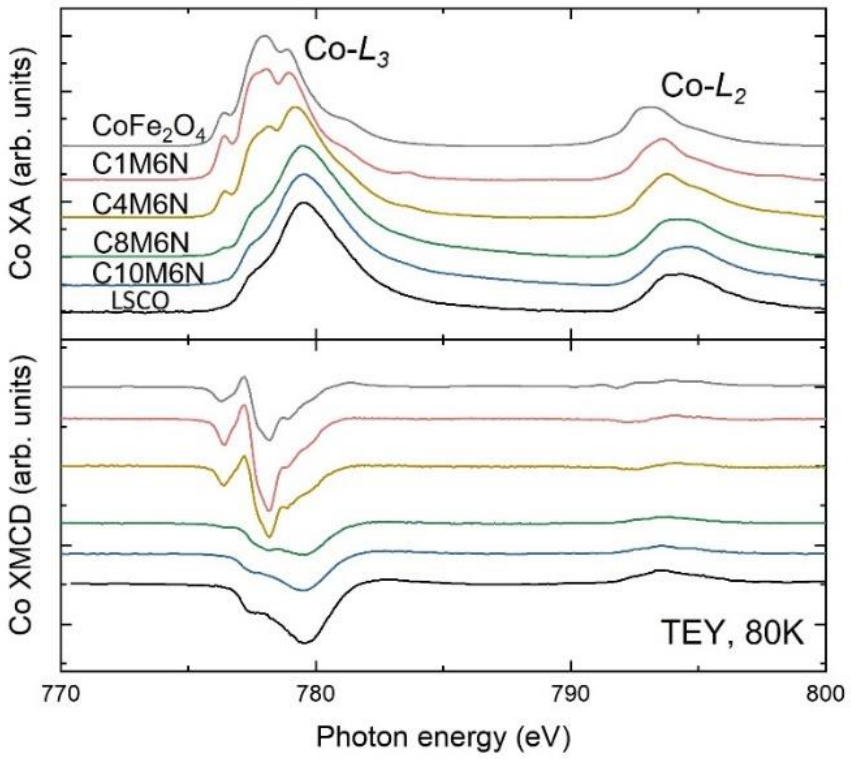

Figure 4.7 Co *L*-edge XA/XMCD spectra of LSCO/LSMO bilayers on NGO substrates taken in TEY mode at 80 K.

The Co-XMCD spectra denote the magnetically active Co ions in the bilayers. The XMCD signal from bilayers C1M6N and C4M6N where Co^{2+} ions dominate are much stronger than thicker bilayers where mixed Co^{3+}/Co^{4+} ions predominate, suggesting that the Co^{2+} ions are in a high spin state [24,81]. Moreover, the decrease of Co-XMCD intensity as t_{LSCO} increases from 1 nm to 8 nm indicates that the number of Co^{2+} ions does not increase with t_{LSCO} but rather are replaced by mixed Co^{3+}/Co^{4+} ions that have lower magnetization. The existence of high spin Co^{2+} ions (larger ionic radius) in thinner bilayers is also supported by the observation of *c*-lattice expansion shown in **Table 4.1**. The formation of Co^{2+} ions cannot be explained by the charge transfer between Co and Mn ions due to the fact that the valence state of Mn ions stays almost

unchanged with t_{LSCO} as shown in **Figure 4.8**, thus we propose the contribution from oxygen vacancies at LSCO/LSMO interface to maintain charge neutrality [81,153].

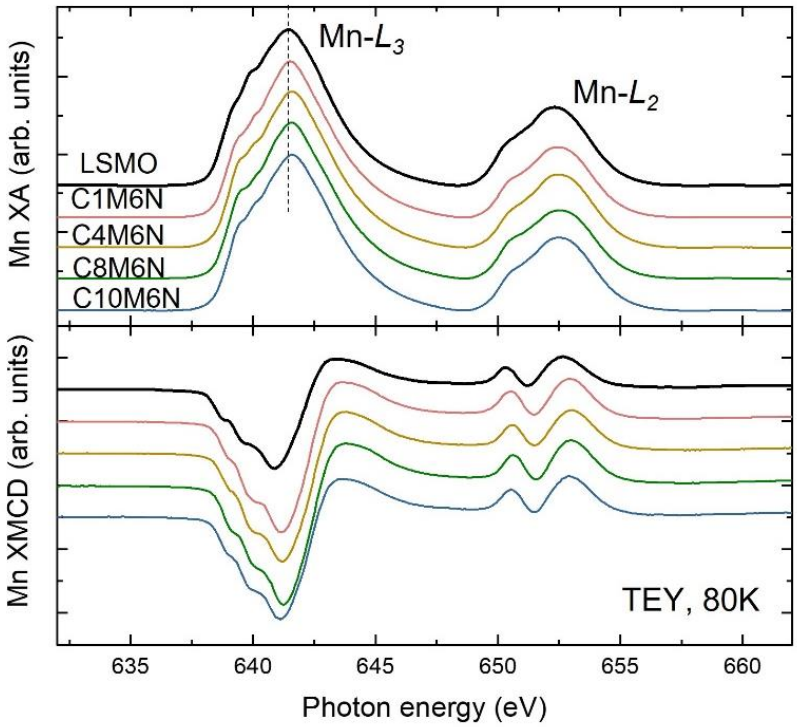

Figure 4.8 Mn *L*-edge XA/XMCD spectra of LSCO/LSMO bilayers on NGO substrates taken in TEY mode at 80 K. Reference spectrum from a LSMO single layer is also plotted. XA/XMCD spectra are normalized to the L_3-edge average XA peak and curves are vertically shifted for clarity.

Figure 4.9 displays the O *K*-edge spectra on bilayers, revealing a decreasing trend of peak A (ascribed to transition metal 3*d* unoccupied states) and an increasing intensity of peak B (transition metal 3*d* relevant absorption peak) with increasing LSCO thickness [45,146]. These observations suggest the presence of more oxygen vacancies in the thinner bilayers.

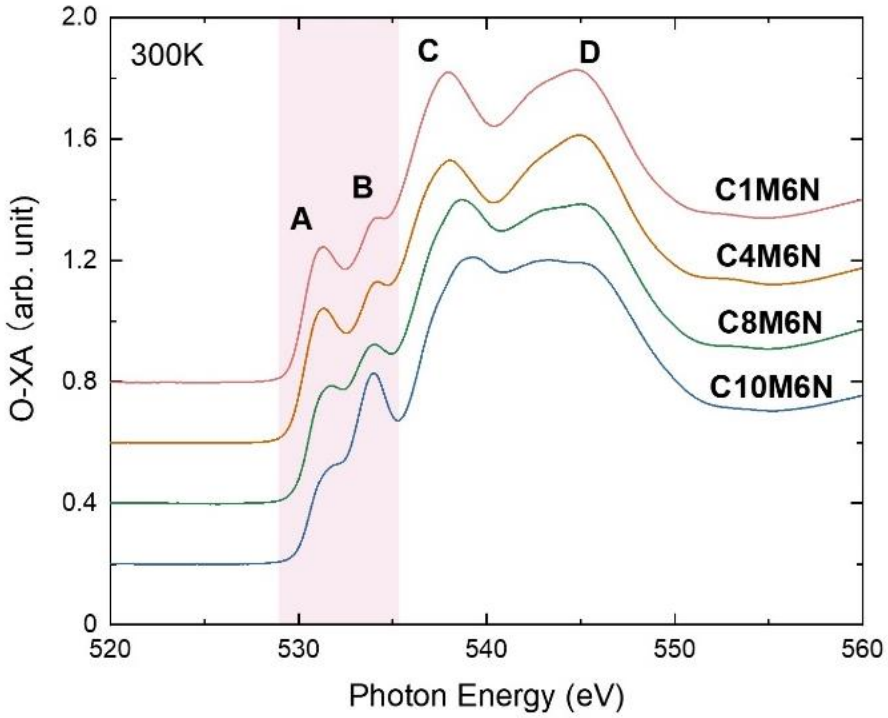

Figure 4.9 O *K*-edge spectra of LSCO/LSMO bilayers on NGO substrates measured at 300 K using TEY mode. Peak A: transition metal 3*d* unoccupied states; Peak B: transition metal 3*d* relevant absorption peak; Peak C: related to the band with La 5*d*/Sr 4*d*; Peak D: related to the band with Mn 4 *sp*.

Finally, XLD is an elemental-sensitive measurement technique for determining the preferred direction of 3*d* orbital occupancy in transition metal oxides that shows a direct correlation to MA [122,150,166]. Here we focus on probing the $3d_{x^2-y^2}$ occupancy because of its direct relationship with in-plane anisotropy. Mn-edge XA spectra were taken with x-rays perpendicular to the sample surface, while the polarization vectors have the geometry of $\vec{E}$//$\boldsymbol{a}$ and $\vec{E}$//$\boldsymbol{b}$, showing schematically in **Figure 4.10**. It should be noted that XLD asymmetry may also arise from factors such as AFM ordering or ferromagnetism [167], but we can rule out the contribution from AFM ordering because of the bulk-like FM behavior of the LSMO layer. The samples were

demagnetized before the measurements and no magnetic field was applied during the measurement.

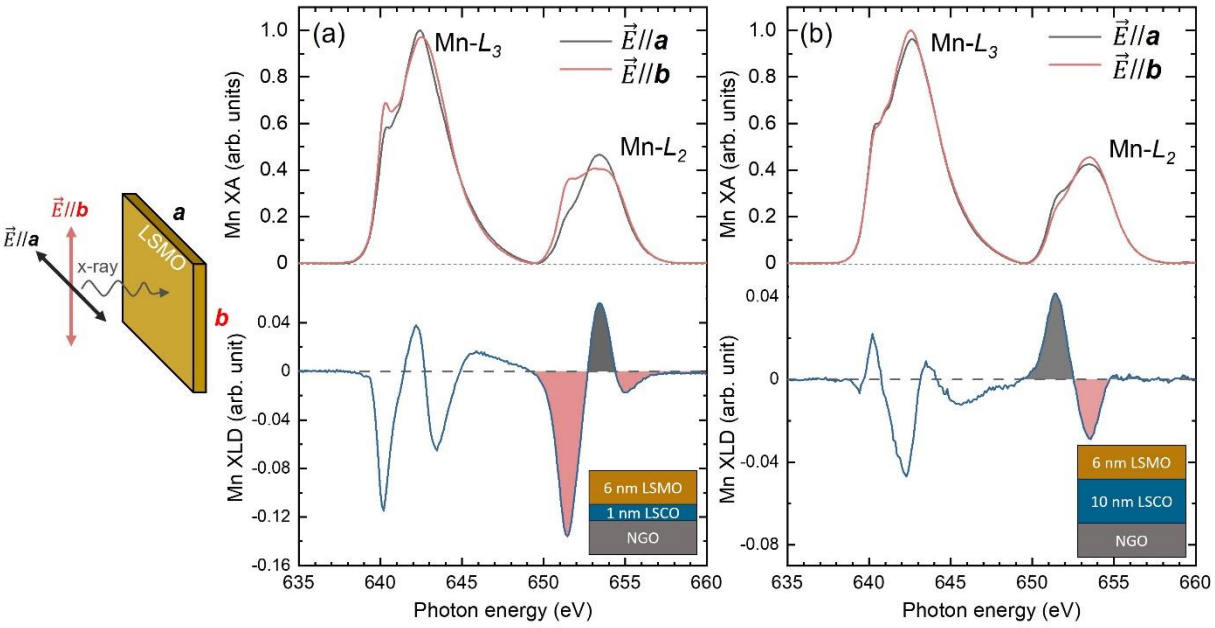

Figure 4.10 A schematic of the XA/XLD measurement geometry (left) for probing the $3d_{x^2-y^2}$ orbital occupancies along the ***a***- and ***b***-directions, with x-rays perpendicular to the sample surface and $\vec{E}$//***a*** and $\vec{E}$//***b***, respectively. Representative Mn *L*-edge XA (top) and XLD (bottom) obtained from (a) C1M6N and (b) C10M6N bilayer. The integrated area under the XLD spectra (A_{XLD}) around Mn-L_2 peak is filled in gray and red for positive and negative XLD values, respectively.

Figure 4.10 (a) and (b) show Mn *L*-edge XA/XLD spectra measured along the ***a***- and ***b***-directions of bilayers C1M6N and C10M6N, respectively. XLD was calculated as the difference between two XA spectra ($I_{XLD} = I_a - I_b$). The integrated area under XLD spectra (A_{XLD}) around the Mn-L_2 peak (from 649 – 660 eV) represents the preferred direction of Mn $3d_{x^2-y^2}$ orbital occupancy [150]. The negative A_{XLD} from bilayer C1M6N reveals enhanced electron occupancy

along the ***a***-direction that aligns well with the magnetic easy axis of the LSMO layer. In contrast, a positive A_{XLD} in bilayer C10M6N indicates favored electron occupancy along the ***b***-direction with the LSMO easy axis along the same direction. To examine the relationship between in-plane electron occupancy and the magnetic easy axis, Co-edge XA/XLD spectra were taken on bilayer C1M6N under the same conditions. The easy axis of LSCO layer was along the ***a***-direction, while A_{XLD} around the Co-L_2 peak (from 792 – 805 eV) was negative as shown in **Figure 4.11**. As a result, both Mn- and Co-edge XLD spectra reaffirm the direct correlation between $3d_{x^2-y^2}$ orbital occupancy and in-plane MA.

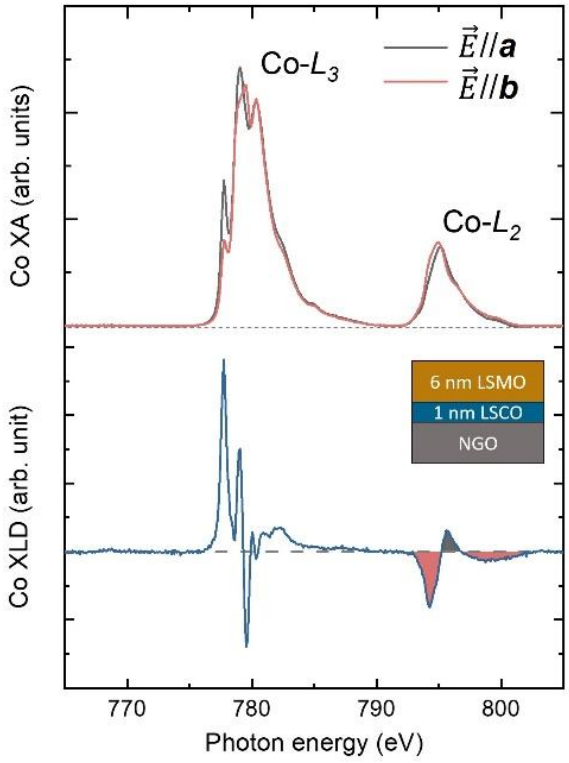

Figure 4.11 Co-edge XA/XLD spectra obtained from bilayer C1M6N taken in TEY mode at 80 K. X-rays are perpendicular to the sample surface with $\vec{E}$//***a*** and $\vec{E}$//***b***, respectively.

Consistent with previous studies, the competition between BO_6 octahedral rotation and strain has been identified as the primary factor that governs the MA of perovskite heterostructures [13,129]. In this study, no strain relaxation was observed with increasing t_{LSCO} from 1 to 10 nm. The LSCO layer maintains its magnetic easy axis along the ***a***-direction, as the tensile strain state is smaller along this direction (0.57%) compared to the ***b***-direction (0.78%). Conversely, we found that the BO_6 octahedral at the heterostructure interface plays a significant role in determining the LSMO magnetic easy axis when $t_{LSCO} \leq 4$ nm. In contrast to the rhombohedral structure in bulk LSCO and LSMO, LSCO/LSMO bilayers exhibit a monoclinic distortion, lead to biaxially anisotropic B-O bond length, thereby inducing the symmetry breaking of the Mn $3d_{x^2-y^2}$ orbitals. The presence of Co^{2+} ions which have a larger ionic radius, and oxygen vacancies can offer more degrees of freedom for octahedral rotation, thus eliminating the strain effect at the interface. Moreover, the FM exchange coupling between the soft LSCO and LSMO layers promotes the alignment of the LSMO easy axis to the LSCO easy axis, resulting in enhanced total magnetization of LSCO layer and enhanced H_C values of LSMO layer. With further increasing t_{LSCO} beyond 4 nm, the concentration of Co^{2+} ions at the interface region decreases, the strain effect becomes the predominant factor influencing the MA of the bilayers. Consequently, the easy axis of the LSMO layer switches from IMA back to BMA, leading to a pronounced EB effect.

4.4 Conclusions

In conclusion, magnetocrystalline anisotropy (MA) of a bulk-like LSMO thin film can be tuned by adjusting the thickness of the underlying LSCO layer for LSCO/LSMO bilayers grown under biaxial strain on NGO substrates. For $t_{LSCO} \leq 4$ nm, no EB effect is observed along the ***a***-

direction due to the strong interfacial magnetic coupling between the two layers that share the same in-plane magnetic easy axis and H_c values. However, along the ***b***-direction, a small negative exchange bias shift is observed because of the small H_c difference between the two layers. As t_{LSCO} increases beyond 4 nm, the EB effect appears due to the difference in MA of the two layers, causing the easy axis of the LSMO layer to rotate back to the $[1\bar{1}0]_o$ direction as in bulk LSMO. With direct correlation to in-plane anisotropy, Mn-edge XLD spectra shows different electron occupancy along the two in-plane directions with increasing t_{LSCO}. Thus, the interfacial exchange coupling between the LSCO and LSMO layers facilitates the rotation of the LSMO easy axis, allowing for the control of MA and EB between the two FM layers. Moreover, the ability to manipulate the MA of FM heterostructures, leading to thickness-dependent properties, makes magnetic perovskite heterostructures promising candidates for next-generation spintronic and magnetic memory devices.

Chapter 5

Hydrogen-induced Topotactic Phase Transformations of Cobaltite Thin Films

5.1. Introduction

The development of neuromorphic computing has inspired a vigorous exploration of innovative materials and methodologies capable of leveraging topotactic phase transformations to tailor functionalities for information processing and memory storage [3,15,41,168–171]. Topotactic phase transformations are characterized by the reversible modulation of crystal structures involving oxygen ion gain or loss, providing potential pathways for tuning electrical and magnetic properties [21,172,173]. Transition metal oxides (TMOs) stand as promising candidates for neuromorphic computing applications, offering diverse functionality including metal-insulator transitions, ferromagnetism, and superconductivity that stem from complex interplays between the spin, charge, orbital, and lattice degrees of freedom [2,9,145,174]. Conventional techniques have been harnessed to induce phase transitions in TMOs, such as thermal annealing in oxygen-rich or reducing environments [41,171,175–177], which usually requires relatively high temperatures (from 400 – 900 ℃) to break metal-oxygen (M-O) bonds. Additionally, the controlled movement of ions driven by electric fields through applying direct positive/negative voltage [178,179] or ionic liquid gating [3,14,180] has been explored. Ionic liquids usually suffer

from toxicity, and high processing costs [181], and the need to distinguish between reversible electrostatic effects and irreversible electrochemical effects [182]. The hydrogenation has recently been shown to offer a novel route for tuning TMO properties where the interactions with hydrogen atoms/ions act as the driving force for topotactic phase transformations [183–186].

While the fundamentals of the hydrogenation process for TMOs are in debate, two primary mechanisms regarding the role of hydrogen atoms/ions have bene proposed. Mazza *et al.* reported using neutron reflectometry that hydrogen solely adsorbs onto the surface of $La_{0.7}Sr_{0.3}MnO_3$ (LSMO) thin films without entering the bulk lattice. Subsequently, the presence of surface absorbed hydrogen atoms facilitates the formation of oxygen vacancies within the bulk [185]. However, for LSMO thin films, the hydrogen absorption process requires the presence of Pt nanoparticles on the film surface, serving as catalysts to enable the phase transformation from perovskite to brownmillerite phase [185,186]. In contrast, the second mechanism suggested that hydrogen ions interact with the lattice ions of the TMOs, creating direct bonds with transition metal ions (substituting for O ions and forming M-H bonds) [187] or with lattice oxygen ions to form O-H bonds [170]. In addition, a dual ion exchange process including the removal of O^{2-} ions and insertion of H^{+} ions was reported in the reversible phase transformation of $SrCoO_{2.5}$ that controlled by electric-field [3]. It should be noted that hydrogen atoms can also occupy interstitial sites in $SmNiO_3$ (SNO) thin films, leading to an eight order of magnitude increase in resistivity. However, this process occurs without any phase transformations [188,189].

Among TMO materials, thin films of the perovskite oxide $La_{1-x}Sr_xCoO_{3-\delta}$ are attractive due to their diverse array of perovskite-related phases, each characterized by unique magnetic and electrical properties, rendering them promising materials for incorporation in neuromorphic computing applications [3,14,41,175,179,190]. For example, the manipulation of distinct topotactic phases of $SrCoO_x$ (SCO) thin films results in a tailored evolution of its physical properties from the equilibrium antiferromagnetic (AFM)/insulating brownmillerite (BM) $SrCoO_{2.5}$ phase to the metastable ferromagnetic (FM)/conducting perovskite (P) $SrCoO_3$ phase [175,191]. In the meantime, the exploration of Sr-doped lanthanum cobaltite ($La_{1-x}Sr_xCoO_{3-\delta}$) remains relatively scarce, in which the perovskite phase ($\delta = 0$) is the equilibrium phase [41,192]. At a Sr doping level of 30%, the perovskite phase manifests a metal-to-insulator transition (MIT) coupled with a FM to paramagnetic transition at the Curie temperature (T_c) of 240 K [2]. The combination of high ionic conductivity and low oxygen vacancy formation energy renders it a promising candidate for the investigation of topotactic phase transformations [169,193].

In a previous work [41], a series of topotactic transformations were initiated in $La_{0.7}Sr_{0.3}CoO_3$ (LSCO) thin films grow on $(LaAlO_3)_{0.3}(Sr_2TaAlO_6)_{0.7}$ (LSAT) substates with controlled reducing conditions through thermal vacuum annealing. With increasing reducing conditions, a series of transformations from the P to BM phase was observed through the loss of O^{2-} ions, followed by an evolution into the Ruddlesden-Popper (RP) phase through the loss of O^{2-} and Co ions. This RP phase displayed weak ferromagnetism at low temperatures (< 25 K) and insulating properties. However, these studies required a combination of high-temperatures (400 ºC - 900 ºC) and ultra-high vacuum (p_{O_2} = 10^{-12} - 10^{-24} atm) conditions. In this chapter, we explored hydrogenation as

an alternative method where topotactic transformations can be achieved under more moderate conditions (< 400 ºC). A topotactic phase transformation from the P to pure BM phase was achieved in hydrogenated LSCO thin films around 220 ºC. However, the continued transition to the RP phase was not observed at higher temperatures due to the role of H atoms/ions in the thin film lattice. The magnetic and electrical properties of the hydrogenated phases were determined by bulk magnetometry, x-ray magnetic circular dichroism (XMCD) and resistivity measurements. This topotactic transformation resulted in approximately a six order of magnitude increase in the room temperature resistivity for the hydrogenated BM phase compared to the as-grown perovskite (AG-P) LSCO film, making it a promising candidate to be used in neuromorphic computing devices.

In this chapter, hydrogenation of the LSCO thin films and x-ray diffraction (XRD) of hydrogenated thin films were performed by Junjie Li at University of California, San Diego.

5.2 Experimental Methods

The LSCO thin films were grown on (100)-oriented single-side polished LSAT substrates by pulsed laser deposition from a stoichiometric $La_{0.7}Sr_{0.3}CoO_3$ target. For consistency and to minimize potential variations in film quality, four pieces of 5×5 mm² substrates were mounted at the central region of the heating plate during a single growth. The chamber was pumped to a base pressure of 3×10^{-6} Torr then subsequently filled with flowing O_2 gas to establish a constant pressure of 300 mTorr. During the deposition, the substrate temperature was held at 700 °C and a KrF excimer laser (λ = 248 nm), with 0.8 J/cm^2 laser energy and 1 Hz laser repetition rate was used. The thin film samples were cooled to room temperature within an oxygen environment of

300 Torr at a cooling rate of 10 °C/min to ensure proper oxygen stoichiometry, which is essential in the study of topotactic phase transformations.

The hydrogenation was performed in a homemade annealing system, which is analogous to the gas evolution system previously reported [171]. The hydrogenation setup consists of a thickened quartz tube connected to a vacuum chamber capable of achieving hydrogen pressures from 10^{-3} to 3.8×10^{3} Torr and temperatures up to 1000 °C. Before flowing hydrogen gas, the quartz tube was preheated to the hydrogenation temperature, and maintained at ~10^{-6} Torr base pressure for at least 30 minutes to remove any gas impurities. An ultra-high vacuum transfer arm was used to insert the LSCO film into the quartz tube. Once the film was loaded and the arm was retracted, the ultra-high pure hydrogen gas (>99.999 %) was introduced into the tube at a rate of ~450 Torr/s using a needle valve and held at a constant pressure of 2.25×10^{3} Torr. After one hour of hydrogenation, the tube was depressurized at a rate of ~300 Torr/s and pumped down to high vacuum. Meanwhile, the film was extracted using the same transfer arm, which was capable of cooling down the sample at an approximate rate of ~10 °C/s. The sample was settled for at least 5 minutes in high vacuum before being exposed to air.

XRD measurements were conducted using a Rigaku SmartLab diffractometer with Cu-$K\alpha_1$ radiation (λ = 0.154 nm). X-ray reflectivity (XRR) and reciprocal space maps (RSMs) were performed using a Bruker D8 Discover four-circle x-ray diffractometer (Cu-$K\alpha_1$ radiation with λ = 0.154 nm). XRR profiles were fitted using GenX software [103] to determine film thickness, roughness, and density of the AG and hydrogenated films. Bulk magnetic properties were determined using a Quantum Design VersaLab or DynaCool system equipped with a vibrating-

sample magnetometer. A magnetic field of 0.08 T was applied along the in-plane [100] substrate direction as sample was cooled to 80 K. Magnetization vs. temperature (*M(T)*) measurements were performed upon warming from 80 K to 350 K, with 0.08 T magnetic field along the same direction. Measurements of film resistivity were conducted using a Lakeshore cryogenic probe station with four-point van der Pauw geometry. The resistivity was measured upon warming from 80 K to 350 K, with a controlled heating rate of approximately 3 K/min.

Soft x-ray absorption (XA) and XMCD spectra were acquired at the Co *L*-edge at 80 K using Beamline 4.0.2 of the Advanced Light Source (ALS) in total electron yield (TEY) and luminescence yield (LY) detection modes. TEY detection probes the sample surface (top 5 – 10 nm) due to the limitation of the escape length of secondary electrons [194], while LY detection provides information of the entire film thickness [195]. For the XMCD measurements, the films were field cooled to 80 K in 0.3 T to ensure that all magnetic moments are aligned along the field direction. During the measurements, a 0.3 T magnetic field was applied parallel to the incident x-ray beam which was 60° from the surface normal. XMCD spectra were calculated as the difference between two jointly normalized XA spectra collected with right (I_{RCP}) and left (I_{LCP}) circularly polarized x-rays [196]. Oxygen *K*-edge XA spectra was acquired at 300 K using Beamline 6.3.1 of ALS in TEY mode with no magnetic field applied.

5.3 Results and Discussion

Figure 5.1 (a) presents the ω-2θ XRD curves of LSCO thin film exposed to hydrogenation temperatures of 170 ºC, 220 ºC, and 320 ºC. A more comprehensive series of XRD profiles spanning a wider range of hydrogenation temperatures (from 150 ºC to 320 ºC) is shown in

Figure 5.2 (b). From the periodicity of the integer and half-order diffraction peaks, the peaks can be indexed to the (00*L*) family of planes from the P, oxygen-deficient perovskite (H-OD-P), or hydrogenated BM (H-BM) phase, where the H-index specifies a phase obtained from hydrogenation rather than vacuum annealing. The reciprocal space map around the (103) substrate peak (**Figure 5.2** (a)) demonstrates that the AG-P LSCO thin film is fully strained to the underlying LSAT substrate throughout its whole film thickness, presented by the vertical alignment of the LSCO film and LSAT substrate peaks marked with a white dashed line. Bulk LSCO film has a lattice parameter of 3.833 Å in pseudocubic notation, while the LSAT substrate has the lattice constant of 3.867 Å [153]. Therefore, the film has an in-plane tensile strain of 0.89%, where the strain is denoted by: $\varepsilon = (a_{strained} - a_{bulk})/a_{bulk}$. As shown in **Figure 5.1** (a), The AG-P LSCO film peaks are on the high angle side of the substrate peaks on the XRD profile, revealing smaller out-of-plane lattice constants as expected. Upon hydrogenation at 170 ºC, the integer film peaks shift towards lower 2θ angles, signifying the expansion of the out-of-plane lattice constant (from 3.80 Å to 3.93 Å), revealing the formation of oxygen vacancies in the H-OD-P phase. In addition, the emergence of a set of less intense peaks (i.e., so-called half-order peaks) at 2θ values of 11.21º, 34.17º, 58.73º signify the formation of the H-BM phase with the quadrupling of the unit cell due to the alternating octahedrally- and tetrahedrally-coordinated layers (see crystal structures with alternating layers shown in **Figure 5.1** (b)). The coexistent of the OD-P and BM phases has been reported in LSCO thin films with a Gd capping layer [192] where the spontaneous oxidation of the Gd capping layer leaches O^{2-} ions from the oxide thin film. For the LSCO film hydrogenated at 220 ºC, the prominent half-order peaks indicate a (near) complete phase transition to the H-BM phase. The out-of-plane lattice constant is calculated to be 16.12Å which is slightly larger than the BM phase ($La_{0.7}Sr_{0.3}CoO_{2.5}$) (16.053 Å) formed after

vacuum annealing at 400 ºC and $1x10^{-24}$ atm [41]. Unlike anneals performed under vacuum conditions [41], at the hydrogenation temperature of 320 ºC, no half order peaks were observed and the integer film peaks are on the high angle side of substrate peak. The film peak positions closely align with those of the AG-P LSCO film, with an out-of-plane lattice constant of 3.81 Å. Therefore, we denoted this high temperature hydrogenated perovskite as the H-P phase rather than the H-OD-P phase.

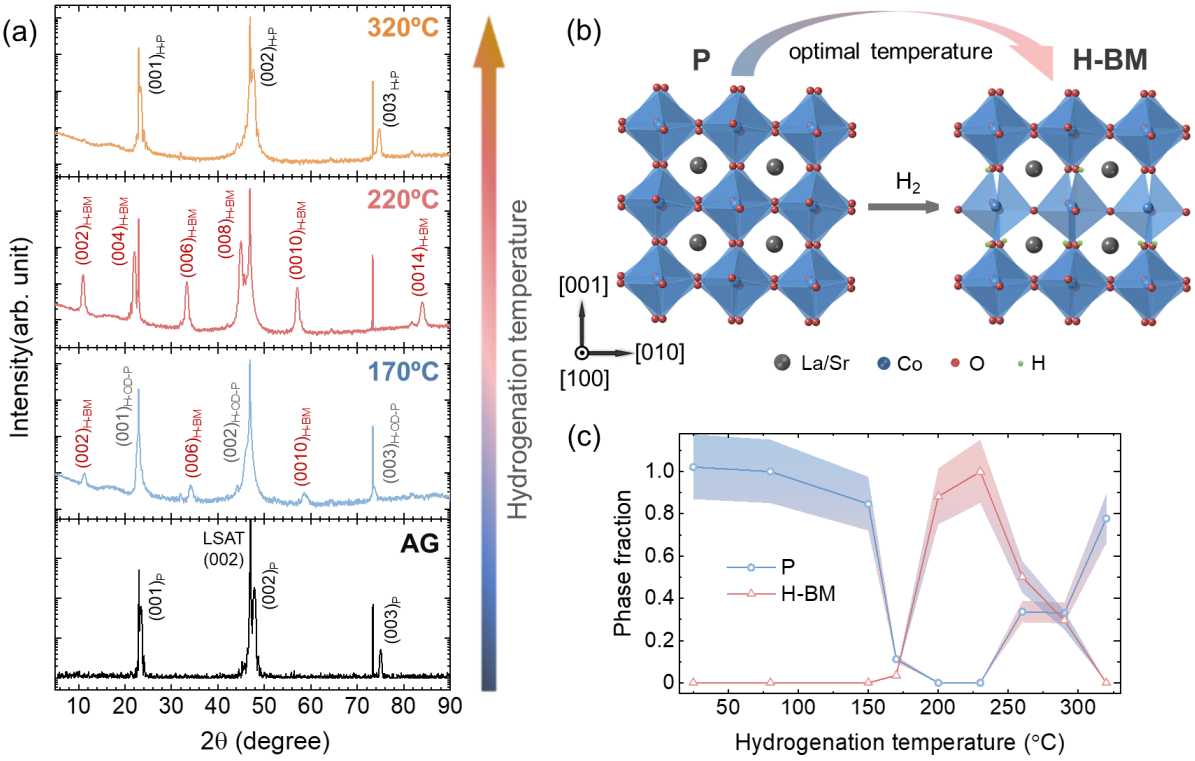

Figure 5.1 (a) XRD patterns of AG and hydrogenated LSCO thin films upon annealing for one hour. The hydrogenation temperature increases from bottom to top. (b) Crystal structure diagrams of the P and H-BM phases. La/Sr, Co, O and H ions are shown in grey, blue, red, and green, respectively. The structures are oriented along pseudocubic axes as determined by XRD. (c) Phase fractions of hydrogenated samples plotted against the hydrogenation temperature. The shaded region denotes the range of error bars.

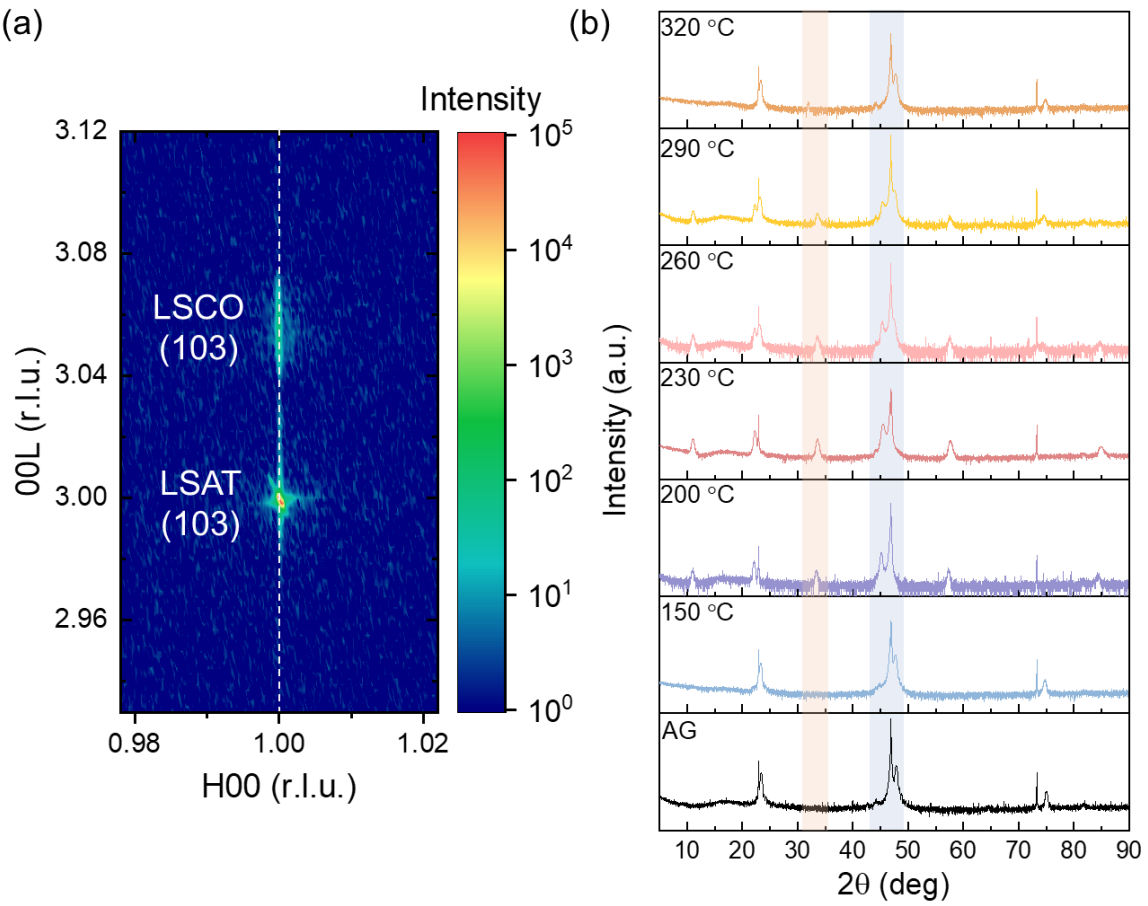

Figure 5.2 (a) RSM around the (103) substrate peak of the AG-P LSCO film on LSAT substrate. The white dashed line marks the vertical alignment of the film peak to the substrate peak. (b) XRD profiles as a function of hydrogenation temperatures ranging from 150 ºC to 320 ºC.

The ω-2θ XRD curves shown in **Figure 5.2** (b) provide further details on the temperature dependence of the hydrogenated topotactic transformation of the LSCO films. The half-order peaks originating from the H-BM phase (shaded in red) only exist at intermediate hydrogenation temperatures (from 170 ºC to 290 ºC) and the H-P peaks (shaded in blue) shift to lower angles (forming the H-OD-P phase) then nearly back to its initial 2θ value (H-P phase) with increasing temperature. **Figure 5.1** (c) shows the phase fraction determined from fitting results of XRD

profiles using the AG-P LSCO film as the P phase and the film hydrogenated at 220 ºC as the pure H-BM phase. The shaded region denotes the range of error bars from the fitting. The evolution of the curves shows that the formation of different perovskite-related phases can be controlled using the hydrogenation temperatures where the H-BM phase only forms for hydrogenation temperatures between 170 °C and 300 ºC. Above 300 ºC, instead of forming more reduced phases, the LSCO thin film reverts to a H-P structure.

The topotactic transitions result in measurable changes in thin film thickness, roughness, and density obtained from XRR measurements. The fitting parameters of the XRR curves for samples before (designated as AG) and after hydrogenation (designated as H) are presented in **Tables 5.1 - 5.3**. To obtain the best fitting results from GenX software, the film must be fit as a thin surface layer and a bulk layer with different fitting parameters [41,81,153]. These parameters show that the H-BM phase formed at 170 ºC and 220 ºC is accompanied by an increase in roughness and a decrease in density. The bulk portion of the pure H-BM phase (220 ºC) shows a decrease in density by approximately 9%, compared to previous reports of around a 13% density decrease for the BM phase formed upon vacuum annealing [41]. Moreover, the total film thickness increases by 2%. This phenomenon can be attributed to the presence of ordered oxygen vacancies in the tetrahedrally-coordinated layers of the H-BM structure that expand the lattice in the out-of-plane direction [40]. The observation of larger density than vacuum annealed BM film and the total thickness expansion of the H-BM film suggests the possibility of the insertion of H ions/atoms accompany with the loss of O^{2-} ions. In contrast, the density of the bulk layer of the H-P phase film (320 ºC), increases by 4.1% after hydrogenation compared to the AG-P LSCO, while the surface layer has the density 6.1% lower than AG-P LSCO. It suggests that

the bulk layer has fewer or no oxygen vacancies but with the insertion of H ions into the lattice, while the surface layer is oxygen deficient and no significant structural change was detected by XRD or the oxygen vacancies are randomly distributed without forming ordered structures.

Table 5.1 Fit parameters of XRR spectra for the LSCO thin film hydrogenated at **170 ºC**

Sample	Thickness (nm)	Roughness (nm)	Density (g/cm^3)
AG-Surface	2.63	0.70	7.05
AG-Bulk	15.76	0.46	6.88
H-Surface	2.55	0.80	6.02
H-Bulk	16.17	0.51	6.69

Table 5.2 Fit parameters of XRR spectra for the LSCO thin film hydrogenated at **220 ºC**

Sample	Thickness (nm)	Roughness (nm)	Density (g/cm^3)
AG-Surface	3.07	0.81	7.07
AG-Bulk	15.50	0.52	6.88
H-Surface	1.74	0.69	4.32
H-Bulk	17.22	1.49	6.24

Table 5.3 Fit parameters of XRR spectra for the LSCO thin film hydrogenated at **320 ºC**

Sample	Thickness (nm)	Roughness (nm)	Density (g/cm^3)
AG-Surface	2.77	0.75	7.07
AG-Bulk	15.80	0.61	6.81
H-Surface	4.93	0.61	6.64
H-Bulk	12.97	0.13	7.09

In order to gain insight into the bonding configuration of the H and O^{2-} ions and the valence states of the Co ions, XA/XMCD spectra at the Co *L*-edge and XA spectra at the O *K*-edge were acquired. **Figure 5.3** (a) shows that a pronounced shift of the Co-L_3 peak to lower photon energy occurs for the H-OD-P (blue curve) and H-BM phase (red curve), in comparison to the AG-P LSCO film (black curve), indicating a significant reduction in the valence state of Co ions in the bulk. In addition, the pre-edge feature (~777.5 eV) in the H-OD-P and H-BM phases, and the prominent triplet structure of the Co-L_3 main peak of the H-BM phase suggest the presence of multiple Co ion valence states. The resemblance in peak shape and position compared to the Co^{2+} reference spectra ($CoFe_2O_4$) included in **Figure 5.4** indicates that Co^{2+} ions are the dominant valence state within the H-BM phase. A comparison between TEY detection mode (which provides surface sensitivity, **Figure 5.4** (a)) and LY detection mode (offering insights throughout the entire film thickness, **Figure 5.4** (b)), shows that the Co-L_3 peak of the H-BM phase in TEY mode has less splitting, and the peak position shifts 0.2 eV to higher photon energy compared to the LY spectra, implying higher Co valence states near the surface. The probing depth of TEY and LY detection modes are schematically shown in the inset of **Figure 5.3** (b). However, we cannot rule out the possibility of surface oxidation, considering the samples'

exposure to air during transfer and extended x-ray exposure. At a hydrogenation temperature of 320 ºC, the Co-XA spectrum closely resembles the spectrum from the AG-P LSCO sample, suggesting comparable valence state and coordination number for the Co ions.

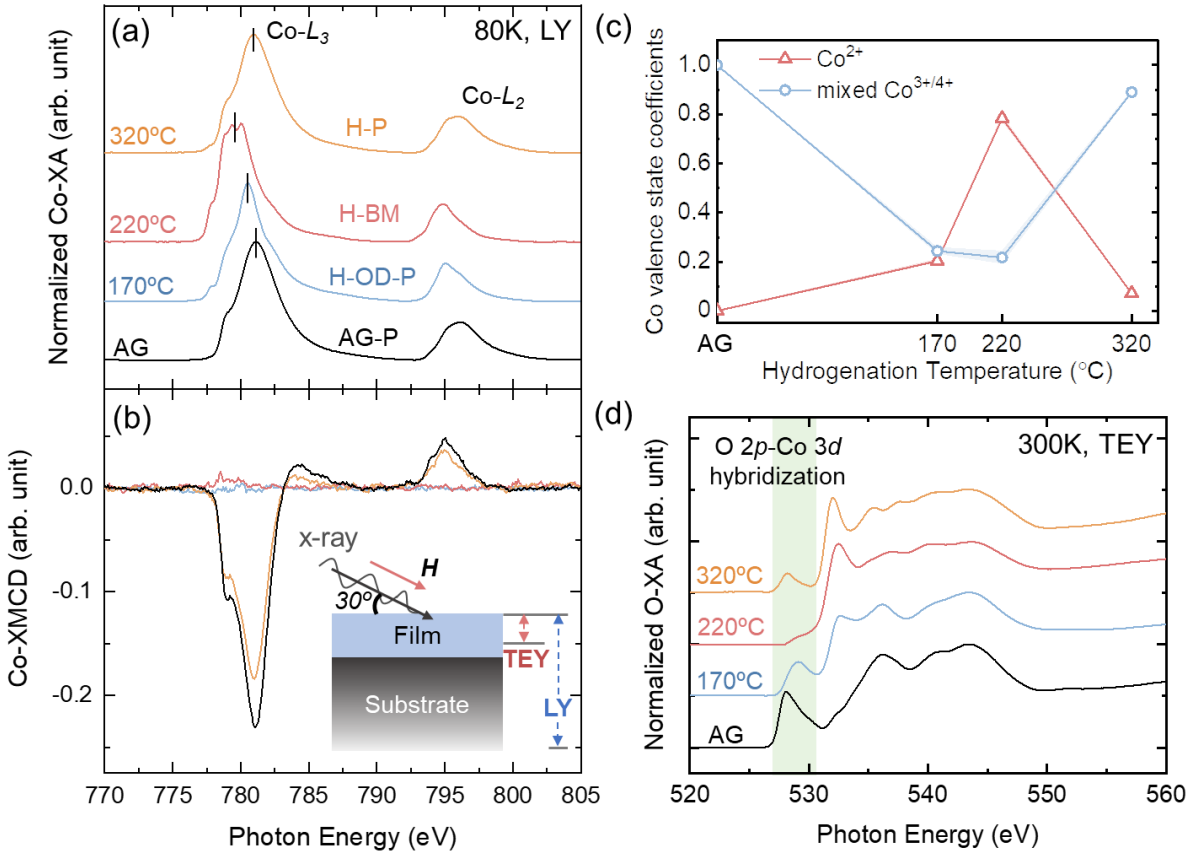

Figure 5.3 Co *L*-edge (a) XA and (b) XMCD spectra of AG- and hydrogenated-LSCO thin films measured in LY mode. XA spectra are normalized from 0 to 1 and vertically shifted for clarity. The inset diagram in (b) represents the measurement geometry and the probing depth of TEY and LY detection modes. (c) Co ion valence state fitting coefficients as a function of hydrogenation temperature. (d) O *K*-edge XA spectra taken at 300 K using TEY mode. The shaded region in green represents the energy range associated with hybridization between O 2*p* and Co 3*d* orbitals.

To quantify the fraction of Co ion valence states, a simple linear fit was applied to the Co-XA spectra of the hydrogenated thin films, employing reference XA spectra from Co^{2+} ions ($CoFe_2O_4$), mixed $Co^{3+/4+}$ ions (AG-P), and Co^{3+} ions ($LaCoO_3$), as displayed in **Figure 5.4**. As previous reports have shown that Co^{3+} ions are mainly confined to the interface between the film and substrate, forming a non-magnetic dead layer due to magneto-electronic phase separation (MEPS) with a thickness below 2 nm [76,197], the analysis focused on the contributions from Co^{2+} and mixed $Co^{3+/4+}$ ions, as shown in **Figure 5.3** (c). An increasing trend in Co^{2+} ions is observed alongside a decreasing trend in mixed $Co^{3+/4+}$ ions as the hydrogenation temperature is raised to 220 ºC, suggesting that the H-BM phase predominantly comprises lower valence Co ions. Upon further elevating the temperature to 320 ºC, the fraction of mixed $Co^{3+/4+}$ ions approaches 1, while the proportion of Co^{2+} ions decreases significantly to nearly 0. Meanwhile, it's worth noting that the fitting quality of the H-BM phase spectra is not as optimal as other samples, and the peak shape doesn't align well with that of the BM-phase LSCO after vacuum annealing as previously reported [41]. This observation leads us to propose that beyond the loss of O^{2-} ions, the insertion of H ions into the film also occurs, causing the Co XA-spectral shape to differ from a conventional BM-phase XA spectra obtained from vacuum annealing [41]. A Co-XA spectrum displaying similar triplet peaks at Co-L_3 edge has been reported for $HSrCoO_{2.5}$ thin films where the H^+ ions are bonded to the apical O^{2-} ions in tetrahedral layers, leading to large lattice expansion [3]. Therefore, we propose that the H-BM phase results from the topotactic phase transformation from a perovskite phase with the loss of O^{2-} ions and insertion of H^+ ions into the lattice, can be described as a dual-ion exchange process.

Figure 5.3 (b) presents the Co-XMCD spectra, derived as the difference between XA spectra acquired with right (I_{RCP}) and left (I_{LCP}) circularly polarized x-rays ($I = I_{RCP} - I_{LCP}$). The applied magnetic field is oriented parallel to the direction of the x-rays and saturates the magnetic moments within the film plane. Both the AG-P and H-P films display strong XMCD intensity, indicative of ferromagnetism from mixed Co^{3+}/Co^{4+} ions in both samples. This result corroborates the findings from the XRD measurements that the H-P phase maintains the structure and magnetic ordering as the AG-P film, suggesting that the hydrogenation process does not have large effect to the LSCO film above 300 ºC or it formed a metastable phase during hydrogenation but returned back to perovskite phase rapidly in air. In contrast, thin films featuring the H-OD-P and H-BM phases exhibit no XMCD signal, suggesting that the Co ions are non-ferromagnetic. Formation of oxygen vacancies affects the Co-O bond length and Co-O-Co bond angle by preventing Co^{3+}-O^{2-}-Co^{4+} double exchange, leading to the existence AFM structures as reported in vacuum annealed OD-P and BM phases of cobaltite thin film which shows no/weak XMCD signal [41,198].

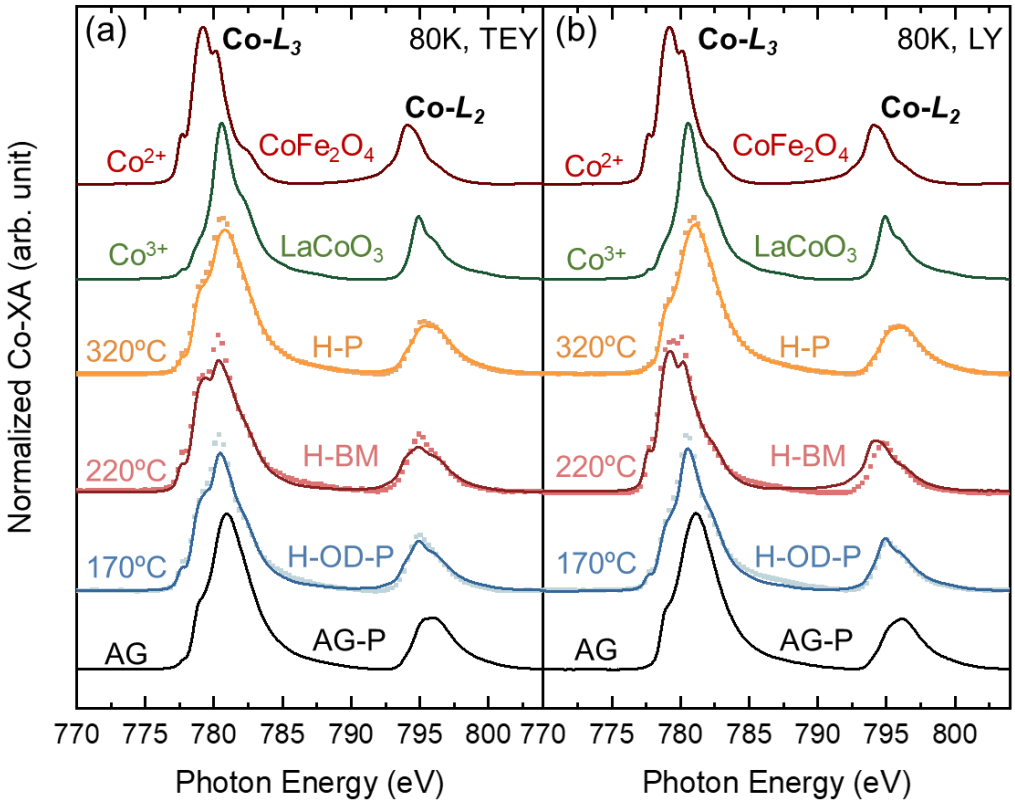

Figure 5.4 Co *L*-edge XA spectra in (a) TEY and (b) LY detection mode of AG and hydrogenated LSCO thin film measured at 80 K. XA spectra are normalized from 0 to 1 and vertically shifted for clarity. Reference spectra of $CoFe_2O_4$ (Co^{2+}) and $LaCoO_3$ (Co^{3+}) are plotted for comparison.

Figure 5.3 (d) plots O *K*-edge XA spectra measured at 300 K using TEY detection mode, exclusively probing the oxygen environment within the film while excluding substrate signals (LY signal reflects a combination of film and substrate contributions). The shaded green region signifies hybridization between O 2*p* and Co 3*d* orbitals within octahedral coordination. The weak pre-peak near 529 eV for the H-BM film corresponds to lower Co valence states, consistent with the increase in Co^{2+} ion concentration, as shown in **Figure 5.3** (a). In contrast, for the H-

OD-P and H-P films, the existence of the pre-peaks suggests that the films are still dominated by Co ions with higher valence states but not as much as in AG-P film due to lower peak intensities. A discernible discrepancy in peak shapes between the AG-P and H-BM phases can be noticed in the photon energy range from 535 eV to 545 eV. However, the characteristic hydroxyl peak around 540 eV, reported in other studies [3,170], is not observed, which does not support the evidence of O-H bonds. However, we cannot rule out the lower concentration of H^+ ions near the surface compared to the bulk, which necessitating alternative techniques for further investigation.

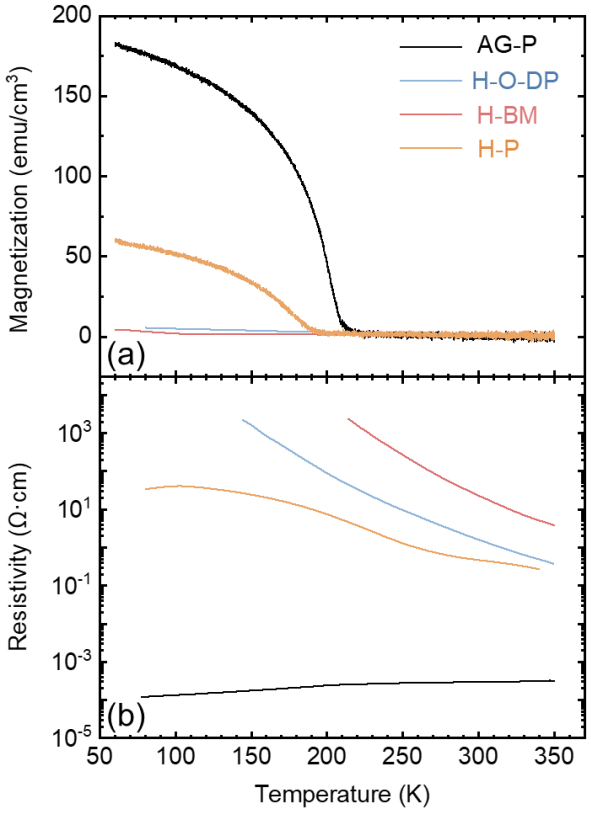

Figure 5.5 (a) Magnetization as a function of temperature for AG-P LSCO and hydrogenated thin films. The magnetizations were normalized to the film volume. A magnetic field of 0.08 T was applied along the in-plane [100] substrate direction during the measurements. (b) Resistivity as a function of temperature.

Figure 5.5 presents the bulk magnetic and electrical characteristics of both the AG-P film and hydrogenated thin films. The magnetization (*M*) was normalized to the respective film volume determined from the XRR/XRD analysis. T_c is determined by identifying the temperature at the peak of $|dM/dT|$. In the case of the AG-P film, a transition from FM to paramagnetic behavior, coupled with a metal-to-insulator transition, is observed around 200 K, which aligns with the bulk LSCO value, as previously reported [41,82]. Both H-OD-P and H-BM films display non-ferromagnetic and insulating behavior across the entire temperature range studied. The room temperature resistivity of the H-BM film is approximately six orders of magnitude higher than that of the AG-P film, presenting a similar value (~10^2 Ω·cm) with the pure BM phase obtained from vacuum annealing [41]. Meanwhile, at lower temperature range, H-BM film exhibits higher resistivity than the pure BM phase, indicating a larger bandgap value (0.62 eV, calculated by a linear fitting of the resistivity Arrhenius plot). This result matches well with the study of $SrCoO_{2.5}$, which has smaller bandgap value than $HSrCoO_{2.5}$ thin film where H^+ ions bonded to O^{2-} ions [3]. The H-P film displays reduced saturation magnetization, lower T_c (174 K) and an increase in resistivity (ρ_{300K} = 0.47 Ω·cm) compared to the AG-P film, suggesting the persistence of oxygen vacancies and H^+ ions within the film even though the crystal structure remains as perovskite. The presence of these disordered oxygen vacancies and H^+ ions have the same effect of hindering the double exchange interaction between Co^{3+} and Co^{4+} ions, resulting in diminished magnetization and increased resistivity. The suppression of double exchange has also been found in hydrogenated LSMO thin films with three orders of magnitude increase in resistivity [186]. With a room temperature resistivity that is higher by four orders of magnitude compared to the AG-P film, the transition from AG-P to H-P phase presents another promising candidate for designing MIT devices without establishing significant phase changes.

Two potential scenarios can explain the emergence of the high-temperature H-P phase. In the first scenario, a highly metastable hydrogenated phase formed at higher temperature during hydrogenation process and quickly reverted back to the perovskite phase with the extraction of H^+ ions from lattice once the film was removed from the hydrogen environment. It has been reported that the hydrogenated BM phase $SrCoO_{2.5}$ ($HSrCoO_{2.5}$), can transform back to the corresponding SCO phase at temperatures exceeding 150 °C in a mixed H_2/Ar gas or O_2 gas environment [199]. Another similar example is the transition of $BaInO_3H$ to $BaInO_3$ in humid air above 300°C [183]. In this study, after the hydrogenation process, the film was removed from the hydrogen source and quenched in a vacuum environment to room temperature. Although the time in vacuum is short, this effect might still result in the decomposition of the metastable phase, leading to the formation of the perovskite phase which is more energetically favorable. In the second scenario, the formation of the metastable phase is excluded. At elevated temperatures, the migration of oxygen ions is significantly constrained by the concurrent diffusion of H ions, which can hop between existing oxygen vacancies or occupy interstitial sites in the lattice [188,189]. Consequently, the crystal structure retains its perovskite phase rather than forming any reduced phases, while the resistivity and magnetic properties differ from pure perovskite phase of AG-P film as shown in **Figure 5.5**.

A remaining question is the role of H^+ ions in the structural and properties change observed with the hydrogenated thin films. We proposed that different hydrogenation temperatures lead to different roles of H^+ ions. For the H-OD-P phase (formed below 170 °C in this chapter), the formation of oxygen vacancies led to AFM/insulating behavior of the film, though we cannot rule out the existence of small amount of H^+ ions in the film which will require more studies in

the future. For the H-BM phase (170 °C to 300 °C), the dual-ion exchange between O^{2-} ions and H^{+} ions leads to larger lattice expansion, higher resistivity at lower temperatures and larger bandgap compare to vacuum annealed BM film [41]. In contrast, for the H-P phase (300 °C to 400 °C), H ions hop between oxygen vacancies or occupy the interstitial sites that prohibit the formation of reducing phases. The film maintains the perovskite structure but shows suppressed magnetization and increased resistivity in comparison to the AG-P LSCO film.

5.4. Conclusions

In summary, LSCO thin films were hydrogenated in pure H_2 gas from room temperature to 400 ºC. The emergence of the H-BM phase with characteristics of AFM/insulating behavior was only achieved at intermediate temperatures from 170 °C to 300 °C compared to 400 °C or higher temperatures required under vacuum annealing conditions. XRR, XRD profiles and XA measurements collectively verified a dual-ion exchange mechanism involving both the loss of O^{2-} ions and insertion of H^{+} ions. An interesting observation was the preservation of the perovskite structure at higher hydrogenation temperatures (above 300 ºC), distinct from the path towards more reduced phases, such as RP phases observed under vacuum annealing conditions. While the H-P phase almost maintain the same crystal structure with the AG-P LSCO film from XRD measurements, the magnetization was suppressed and resistivity significantly increased, signifying the presence of a limited number of disordered oxygen vacancies and the existence of H ions that impede the double exchange interactions between Co ions. The versatility of perovskite LSCO in adopting high-resistance phases, either through phase transformation to the BM phase or without substantial phase changes, underscores its potential for application in the fabrication of MIT devices tailored for the realm of neuromorphic computing.

Chapter 6

Topotactic Phase Transformations in Magnetite and Ferrite Thin Films under Vacuum Annealing

6.1. Introduction

Transition metal oxides (TMOs) are promising candidate materials for applications in neuromorphic computing and spintronic devices, owing to their intricate interplay of spin, charge, orbital, and lattice interactions that yield a wide range of functional properties, including metal-to-insulator transitions (MIT), and magnetic transitions between ferromagnetic (FM) to antiferromagnetic (AFM) phases [3,14,171]. Topotactic phase transformations involve reversible modifications in crystal structures through the gain or loss of oxygen ions or transition metal ions, offering a pathway to finely tune electrical and magnetic properties, enabling the tailoring of emerging functionalities [4,200,201]. Various techniques have been employed to induce these phase transitions in TMOs, such as thermal annealing in oxygen-rich or reducing environments [41,176,185], as well as through the manipulation of applied electric fields [170,178,179].

Among TMOs, cobaltite thin films have attracted considerable attention due to their relatively low oxygen vacancy formation energy and high ionic diffusivity [41,179,180,202]. Meanwhile, investigations into the structural and functional property changes resulting from thermal annealing of manganite and ferrite thin films remain largely unexplored [203–205]. Among these intriguing materials, $La_{0.7}Sr_{0.3}MnO_3$ (LSMO) and $La_{0.7}Sr_{0.3}FeO_3$ (LSFO) thin films have similar oxygen ion diffusivity as $La_{0.7}Sr_{0.3}CoO_3$ (LSCO), making them potential candidates for the study of topotactic phase transformations [202,206]. Similar to LSCO, bulk LSMO exhibits FM to paramagnetic transition coincident with an MIT around its Curie temperature (T_c) of approximately 360 K [42]. In contrast, LSFO is a G-type AFM insulator with its Néel temperature (T_N) at around 360 K [50]. For LSMO thin films, the phase transformation from perovskite (P) to brownmillerite (BM) phases has been realized through various techniques, such as depositing an oxygen-deficient complex oxide film as an oxygen getter layer [4], thermally annealing under oxygen-deficient environments [185,203,205], and applied electric fields [170,178]. For ferrite thin films, Xie *et al*. reported reversible oxygen loss leading to significant changes in electronic conductivity, optical absorption, and lattice parameters within $La_{0.3}Sr_{0.7}FeO_{3-\delta}$ films [56]. Additionally, recent work by Taylor *et al*. highlighted the intriguing observation that the Gibbs free energy of oxygen vacancy formation becomes less favorable at 400 °C compared to room temperature for an O_2 partial pressure of 2.25 Torr in $La_{0.5}Sr_{0.5}FeO_3$ thin films [176].

In a prior study [41], a sequence of controlled topotactic transformations was induced in $La_{0.7}Sr_{0.3}CoO_3$ (LSCO) thin films grown on $(LaAlO_3)_{0.3}(Sr_2TaAlO_6)_{0.7}$ (LSAT) substrates through annealing under oxygen partial pressure of 7.6×10^{-22} to 7.6×10^{-5} Torr from 200 °C to 1000 °C.

This process initiated the transition from the FM/metallic P phase to the AFM/insulating BM phase through the loss of oxygen ions, followed by a progression into the *n*=1 Ruddlesden-Popper (RP) phase ($La_{1.4}Sr_{0.6}Co_{1+\upsilon}O_{4-\delta}$) characterized by the loss of both oxygen and cobalt ions from the oxide matrix. The RP phase exhibited weak ferromagnetism at temperatures below 25 K coupled with insulating behavior in the range of temperature investigated from 150 – 300 °C. The results of these cobaltite thin films inspire the investigation of other TMOs which also possess low oxygen vacancy formation energy and high ionic diffusivity. This study applied the same vacuum annealing conditions to LSMO and LSFO thin films in order to introduce oxygen vacancies and compared the observed changes to the structural and functional properties. Unlike the cobaltite films which readily progressed through a series of topotactic transformations, a pronounced phase transformation was observed only at the highest annealing temperature for LSMO films, resulting in a mixed phase featuring both BM and RP phases. In contrast, the LSFO films displayed the oxygen-deficient perovskite (OD-P) phase across the temperature range used in this study. For annealing temperatures between 400 – 600 °C, the LSFO films maintained their AFM/insulating behavior, however, the LSFO film annealed at 900 °C exhibited weak ferromagnetism and metallic behavior. The distinct trends in phase transformations observed in LSCO, LSMO, and LSFO films yield valuable insights for selecting potential candidate materials for neuromorphic computing applications.

In this chapter, vacuum annealing of the LSMO, LSFO thin films and x-ray diffraction (XRD) of post-annealed thin films were performed by Junjie Li at University of California, San Diego.

6.2 Experimental Methods

The LSMO and LSFO thin film were grown on (001)-oriented LSAT and $SrTiO_3$ (STO) substrates, respectively, by pulsed laser deposition, in order to minimize the in-plane lattice strain. To maintain uniformity and mitigate potential variations in film quality, four pieces of 5 x 5 mm^2 substrate were mounted centrally on the heating plate during a single growth cycle. The vacuum chamber was pumped to reach a base pressure of 3×10^{-6} Torr before being subsequently filled with flowing O_2 gas, establishing a steady pressure of 0.3 Torr. During the deposition process, the substrate temperature was maintained at 700 °C, and a KrF excimer laser (λ = 248 nm) was used. The growth of LSMO thin films was achieved using a laser energy of 1.0 J/cm^2 and a laser repetition rate of 1 Hz. For LSFO thin films, a laser energy of 1.0 J/ cm^2 and a laser repetition rate of 10 Hz were utilized. To ensure the appropriate oxygen stoichiometry, the thin films were gradually cooled to room temperature in an oxygen-rich environment with a pressure of 300 Torr, with a cooling rate of 10 °C/min.

The vacuum annealing was carried out within a custom-designed gas evolution system [171], which consists of a tube furnace linked to a high vacuum setup, capable of attaining oxygen partial pressures spanning from 7.6×10^{-10} to 76 Torr, and temperatures extending up to 1000 °C. The gas evolution system maintained a base pressure of approximately $\sim7.6\times10^{-8}$ Torr, with high-purity oxygen (> 99.99%) introduced into the annealing chamber through a computer-controlled metal-seated valve at pressures around 7.6×10^{-10} Torr. For LSMO and LSFO films, all anneals were performed for 1 hour.

XRD measurements were performed using a Rigaku SmartLab diffractometer with Cu-$K\alpha_1$

radiation (λ = 0.154 nm). X-ray reflectivity (XRR) and reciprocal space maps (RSMs) were measured using a Bruker D8 Discover four-circle x-ray diffractometer (Cu-$K\alpha_1$ radiation with λ = 0.154 nm). XRR profiles were fitted using GenX software [103] to determine the film thickness, roughness, and density of the as-grown (AG) samples and vacuum annealed samples. Bulk magnetic properties of LSMO thin films were determined using a Quantum Design VersaLab system equipped with a vibrating-sample magnetometer. A magnetic field of 0.08 T was applied along the in-plane [100] substrate direction as thin film was cooled to 80 K. Magnetization vs. temperature (*M(T)*) measurements were performed upon warming from 80 K to 350 K, with 0.08 T magnetic field along the same direction. Measurements of film resistivity were performed using a Lakeshore cryogenic probe station with four-point van der Pauw geometry. The film was measured upon warming from 80 K to 350 K, with a controlled heating rate of approximately 3 K/min.

Soft x-ray absorption (XA) and x-ray magnetic circular dichroism (XMCD) spectra were acquired from the AG- and annealed-LSMO films at the Mn *L*-edge at 80 K using Beamline 6.3.1 of the Advanced Light Source (ALS) at Lawrence Berkeley National Laboratory. Both total electron yield (TEY) mode and luminescence yield (LY) mode signal were acquired. TEY mode is limited by the escape length of secondary electrons [136] and thus probes the sample surface (top 5 – 10 nm), while LY mode captured information across the entire film thickness [117]. The LSMO layers underwent field cooling in a 0.3 T magnetic field, ensuring alignment of all magnetic moments along the field direction. During the measurements, a 0.3 T magnetic field which was applied parallel to the incident x-ray beam and at a 60° angle from the surface normal. XMCD spectra were calculated as the difference between two coherently normalized XA spectra,

acquired by changing polarity of the magnetic field which was parallel or anti-parallel to x-ray. Oxygen *K*-edge XA spectra were collected without applying a magnetic field at 300 K. Fe *L*-edge XA/XMCD measurements were only conducted in TEY mode from the LSFO films using Beamline 6.3.1 at ALS, due to the limited LY signal emanating from STO substrates at 80 K. A 0.3 T magnetic field which was parallel to the incident x-ray beam, which was applied perpendicular or at a 30° angle to the sample surface. Fe *L*-edge soft x-ray magnetic linear dichroism (XMLD) measurements were performed at 80 K in TEY mode, using Beamline 4.0.2 of the ALS. The XMLD spectra were calculated by the difference between XA spectra acquired with s- and p-polarized x-rays, where the x-ray ***E***-vector was respectively aligned parallel to the in-plane [010] substrate direction or canted by 30° from the [001] substrate direction, based on the grazing-incidence geometry (x-ray is 60° away to surface normal) of the measurements.

6.3 Results and Discussion

Figure 6.1 presents the XRD curves of the as-grown (AG) LSMO and LSFO thin film on LSAT and STO substrates, respectively. The LSMO layers exist under a small compressive strain on LSAT substrates ($a_{LSMO} = 3.876$ Å, $a_{LSAT} = 3.867$ Å), therefore, the LSMO film peaks appear on the low angle of the substrate peaks as shown in **Figure 6.1** (a). Fitting of the XRD curves using Leptos software [135] indicates a small out-of-plane lattice expansion such that $c_{LSMO} = 3.90$ Å. In contrast, almost no lattice mismatch exists between the LSFO layers and the STO substrates ($a_{LSFO} = 3.91$ Å, $a_{STO} = 3.905$ Å) [5], where the film and substrate peaks overlap as shown in **Figure 6.1** (b). For both LSMO and LSFO films, periodic Kiessig fringes indicate good crystallinity throughout the film thickness with smooth interfaces. The near-identical XRD profiles in each plot reveal the consistency of the films from a single growth

process. Notably, a minor thickness variation (< 2 nm) between LSFO samples is observed due to the relatively smaller laser spot size used during growth. RSMs were acquired around the (103) substrate peak to demonstrate the strain state of the AG-films (**Figure 6.2**). For both LSMO and LSFO films, no strain relaxation occurs throughout the whole film thickness, as observed by the vertical alignment of film peak and substrate peak marked with a white dashed line. Therefore, both LSMO and LSFO film exist under minimal in-plane compressive strain of 0.23% and 0.13%, respectively, where the strain is denoted by: $\varepsilon = (a_{strained} - a_{bulk})/a_{bulk}$.

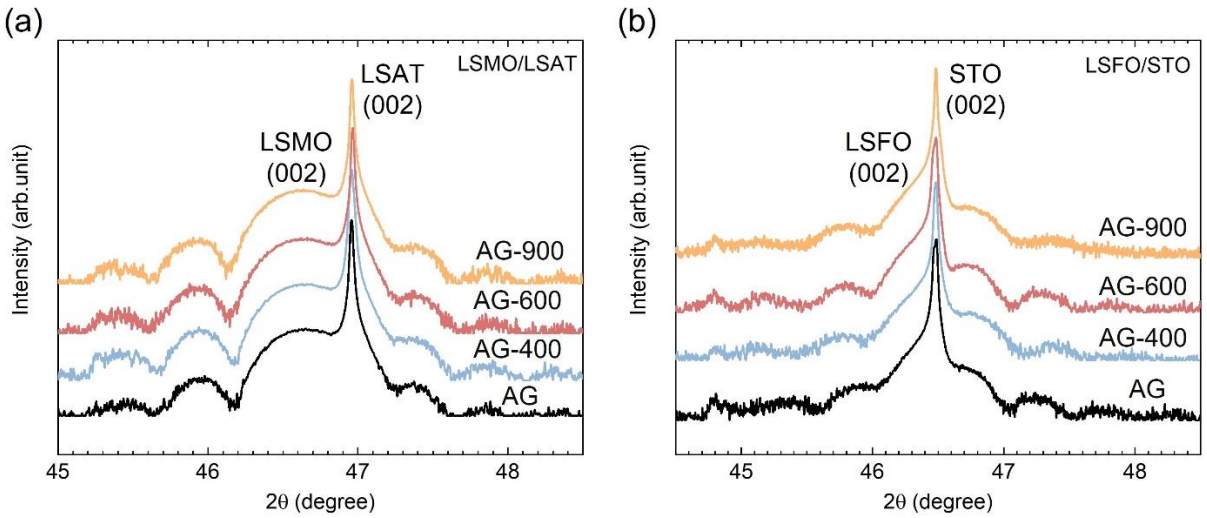

Figure 6.1 XRD profiles of AG (a) LSMO/LSAT and (b) LSFO/STO thin films around the (002) substrate peaks.

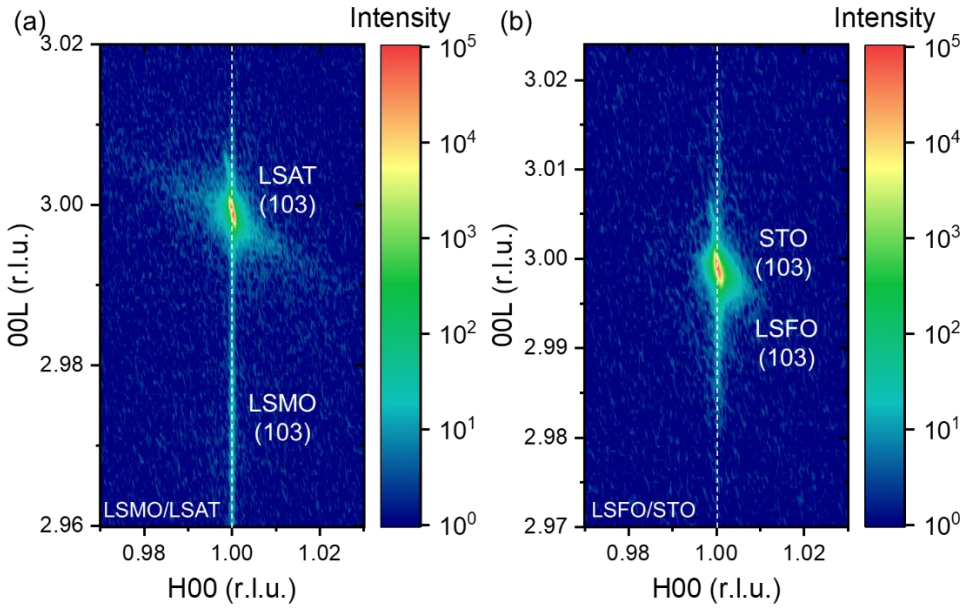

Figure 6.2 RSM around the (103) substrates peak of as-grown (a) LSMO/LSAT and (b) LSFO/STO thin films. The white dashed line denotes the vertical alignment of the film and substrate peaks.

The impact of vacuum annealing on the structural properties of the LSMO and LSFO thin films are shown in the XRD profiles in **Figure 6.3** (a) and (b), respectively. Both sets of samples underwent annealing at 400 °C, 600 °C, and 900 °C with an oxygen partial pressure of 7.6×10^{-10} Torr for one hour. In the case of LSMO films, a transformation from the P phase to the OD-P phase was observed after annealing at 400 °C and 600 °C. The expansion of out-of-plane lattice constant is evidenced by the shift of the film peak to lower 2θ values, indicative of an increasing oxygen vacancy concentration. The out-of-plane lattice parameters were calculated to be 3.90 Å, 3.94 Å and 3.99 Å for AG, 400 °C and 600 °C annealed film, respectively. At 900 °C, several new peaks emerge at 2θ values of 10.79°, 27.72°, 32.49°, and 55.52°, indicating the transformation to other perovskite-related phases. Indexing the peaks shows that the film consists of a mixture of

both the RP ($c_1 = 12.862$ Å) and BM ($c_2 = 16.501$ Å) phases, matching reported values from the literature [41,205]. It should be noted that both families of peaks experience significant peak broadening and loss of integrated intensity (more so for the RP phase), indicating the presences of structural defects. In contrast, the LSFO thin films show no evidence of the emergence of new phases within the studied temperature range, but rather only the transition to the OD-P phase with out-of-plane lattice parameter of 3.94 Å regardless of annealing temperature. The results from XRD profiles indicate that higher annealing temperature (above 600 °C) is required for LSMO film to undergo phase transformations from P phase to BM/RP mixed phases compared to LSCO film [41]. In contrast, for LSFO film, within the temperature range in this chapter (400 °C to 900 °C), no reducing phases (BM or RP phases) were observed.

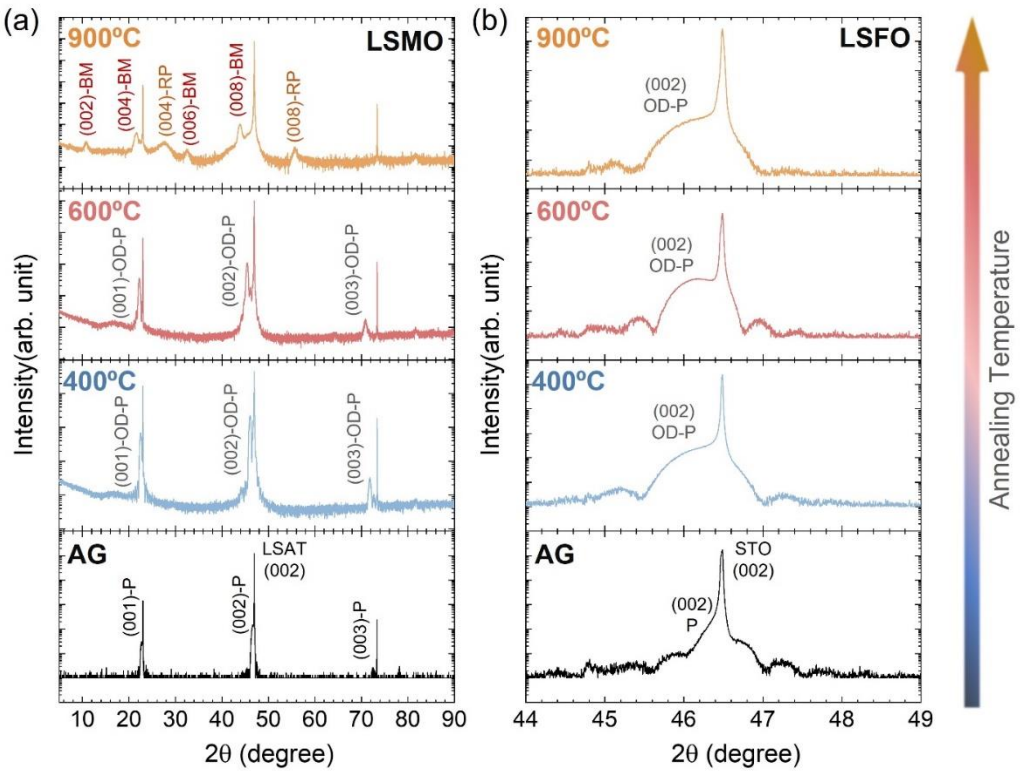

Figure 6.3 XRD patterns of AG and vacuum annealed (a) LSMO/LSAT and (b) LSFO/STO thin films. The annealing temperature increases from bottom to top.

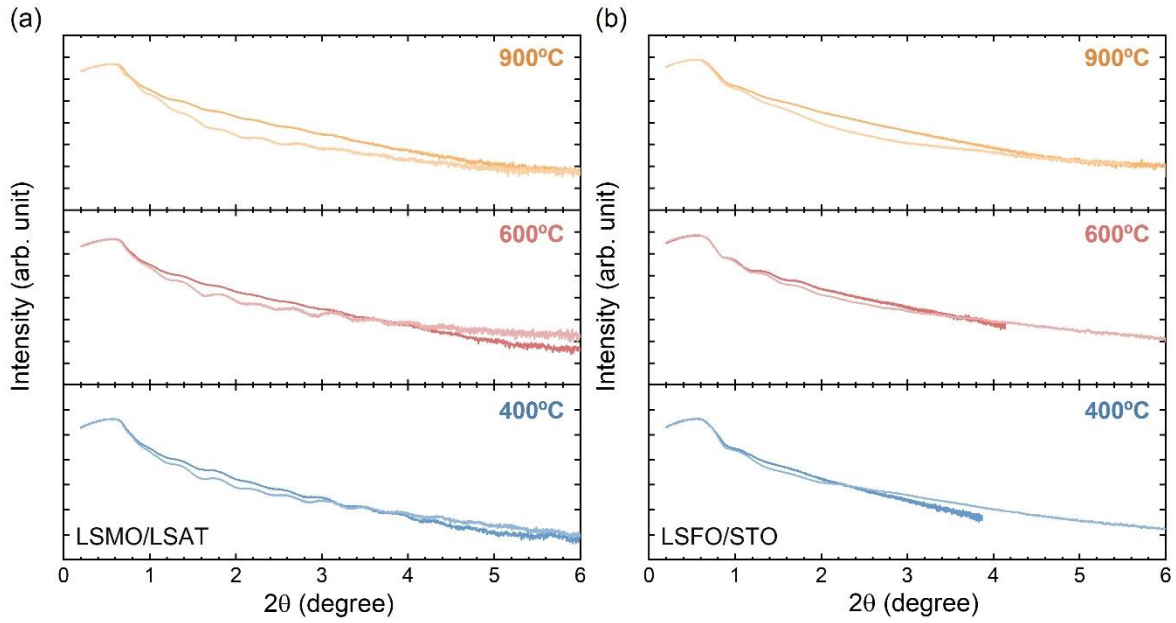

Figure 6.4 XRR curves of AG and vacuum annealed (a) LSMO/LSAT and (b) LSFO/STO thin films. The annealing temperature increases form bottom to top. The dark curve corresponds to the individual AG films, while the light curve represents annealed films.

The change in the thin film thickness, roughness, and density that resulted from the vacuum annealing can be observed through the fitting of XRR curves utilizing the GenX software [103]. Detailed fitting parameters of LSMO films are presented in **Tables 6.1 - 6.3**. **Figure 6.4** shows the AG (darker color) and vacuum annealed (lighter color) LSMO and LSFO films in panels (a) and (b), respectively. Both sets of annealed films exhibit higher roughness, shown as more rapid decay of the XRR curves. The critical angles of the annealed LSMO films shift to lower 2θ values, indicating decreased density with increasing annealing temperatures as listed in **Tables 6.1-6.3**. The XRR curves for the LSFO films show only a slow decay of the curves without prominent thickness fringes, indicating that the films have a similar overall roughness as the LSMO films, but have a limited density contrast between the film and substrate. Due to the lack

of prominent thickness fringes, the quantitative fitting of the XRR curves cannot be performed. Based on the XRR curves, the critical angle variation of the annealed LSFO thin films is negligible (< 2%), consistent with the absence of phase transformations observed in the XRD profiles.

Table 6.1 Fit parameters of XRR spectra for **400 ºC** vacuum annealed **LSMO** film

Sample	Thickness (nm)	Roughness (nm)	Density (g/cm^3)
AG-Surface	2.29	0.46	6.95
AG-Bulk	18.07	0.46	6.41
400 ºC -Surface	1.71	0.27	5.37
400 ºC -Bulk	18.38	0.77	6.49

Table 6.2 Fit parameters of XRR spectra for **600 ºC** vacuum annealed **LSMO** film

Sample	Thickness (nm)	Roughness (nm)	Density (g/cm^3)
AG-Surface	1.81	0.46	6.94
AG-Bulk	17.66	0.42	6.49
600 ºC -Surface	1.91	0.38	5.25
600 ºC -Bulk	17.8	0.68	6.43

Table 6.3 Fit parameters of XRR spectra for **900 ºC** vacuum annealed **LSMO** film

Sample	Thickness (nm)	Roughness (nm)	Density (g/cm^3)
AG-Surface	1.91	0.45	6.94
AG-Bulk	17.71	0.48	6.43
900 ºC -Surface	1.94	0.36	4.10
900 ºC -Bulk	16.94	0.97	6.00

Bulk LSMO displays coincident FM-to-paramagnetic and MIT occurring at T_c ~ 360 K [42], and T_c values in thin films typically decrease with decreasing film thickness and decrease sharply below a thickness of 20 unit cells [83,207–209]. **Figure 6.5** plots the *M(T)* curves of both the AG and vacuum annealed LSMO thin films. As expected, the AG-LSMO film exhibits a T_c of around 324 K, while an observable trend emerges as the annealing temperature increases: a reduction in both T_c and the magnetization of the annealed films. Meanwhile, the linear shape of the *M(T)* curves for the film annealed at 400 ºC and 600 ºC indicate the films likely have a range of T_c values. The formation of disordered oxygen vacancies breaks the double exchange interactions between Mn^{3+}-Mn^{4+} ions, leading to lower magnetization. In particular, the film annealed at 900 ºC displays non-FM behavior, aligning with reports that the BM and RP phases are weak/non-FM [205,210].

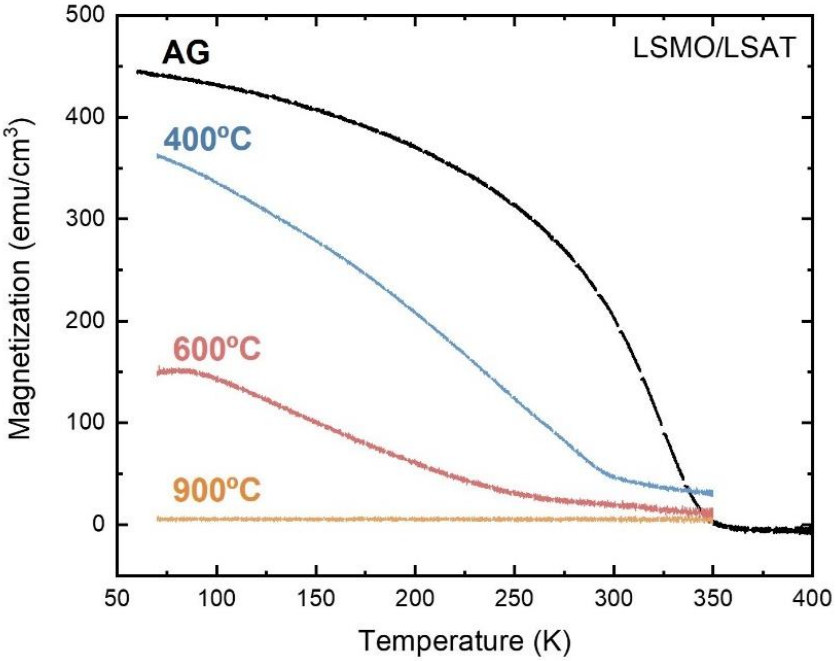

Figure 6.5 Magnetization as a function of temperature for AG and vacuum annealed LSMO thin films. The magnetization was normalized to the film volume. A magnetic field of 0.08 T was applied along the in-plane [100] substrate direction during the measurements.

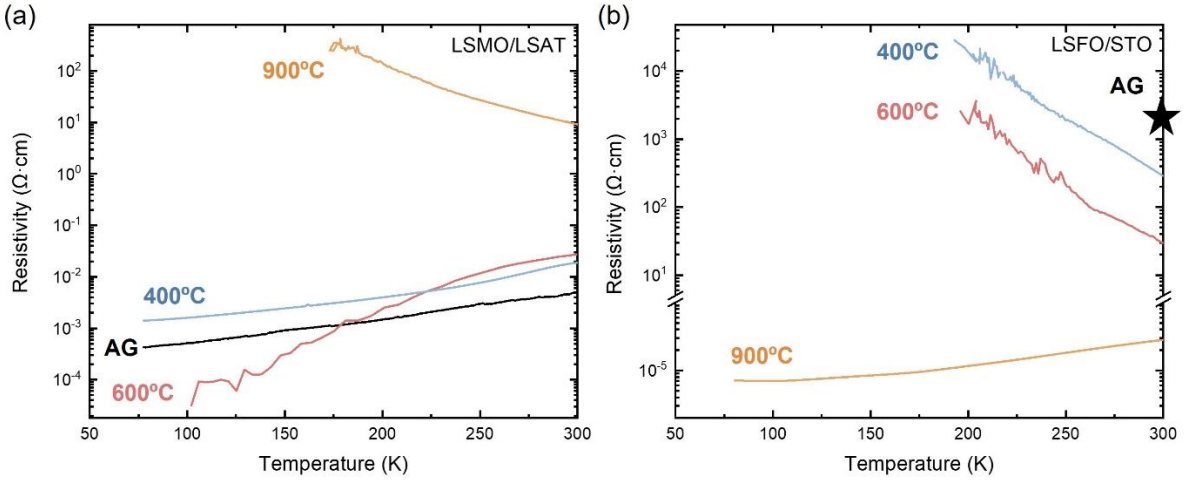

Figure 6.6 Resistivity as a function of temperature for AG and vacuum annealed (a) LSMO and (b) LSFO thin films.

Figures 6.6 (a) and (b) plot the resistivity profiles of both the AG and vacuum annealed LSMO and LSFO thin films, respectively. AG-LSMO and films annealed at lower temperatures (< 900 ºC) exhibit metallic behavior up to 300 K, with one order of magnitude change in resistivity at room temperature. However, the 900 ºC annealed film displays insulating characteristics, with a room temperature resistivity value that exceeds that of AG-LSMO by three orders of magnitude. It should be noted that the accuracy of the resistivity curve for the 600 ºC annealed film is compromised due to the significantly smaller sample size caused by sample breakage during annealing, making it challenging to establish proper electrical connections to the sample corners. In contrast, the AG LSFO film exhibits a high resistivity value of 2270 Ω· cm at 300 K (marked as a star in **Figure 6.6** (b)). Surprisingly, despite the absence of significant phase transformations between the annealed films as shown in the XRD profiles, the resistivity values experience a substantial decrease with increasing annealing temperature. This phenomenon is particularly pronounced in the case of the film annealed at 900 ºC, which exhibits metallic behavior and a room temperature resistivity more than seven orders of magnitude lower than that of the AG-LSFO film.

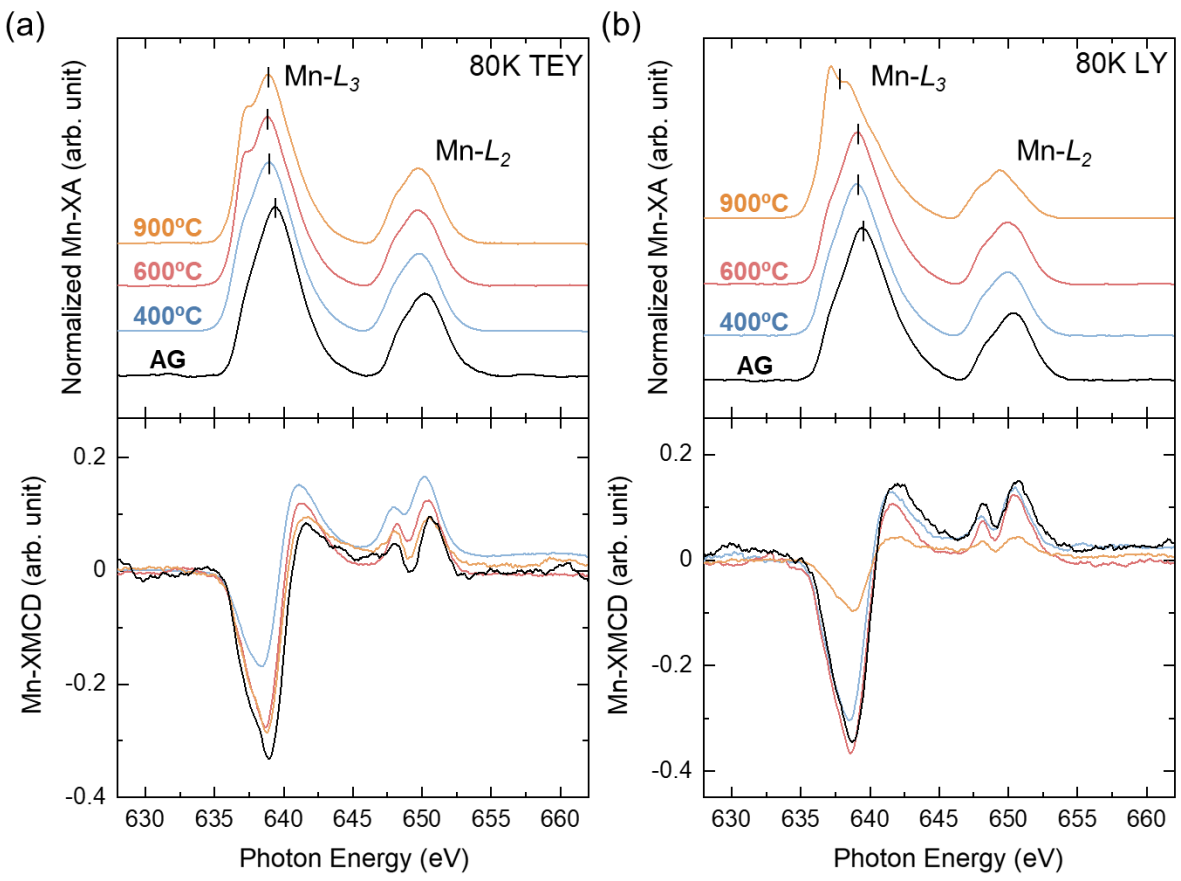

Figure 6.7 Mn *L*-edge XA spectra in (a) TEY and (b) LY detection mode of AG and vacuum annealed LSMO thin films measured at 80 K. XA spectra are normalized from 0 to 1 and vertically shifted for clarity. The short black lines on Mn-L_3 peaks mark the representative peak positions obtained from Gaussian fitting.

XA/XMCD spectra were collected at the Mn *L*-edge on both the AG and vacuum annealed LSMO thin films to probe the bonding arrangement, valence state, and magnetic properties of Mn the ions. The spectra presented in **Figure 6.7** (a) were acquired in TEY mode, which is sensitive to the top 5-10 nm of the film surface, while **Figure 6.7** (b) shows spectra acquired using LY mode, probing the entire film thickness. In the case of the LSMO film annealed at

400ºC, the XA spectra shape closely resembles that of AG-LSMO in both TEY and LY detection modes, displaying only a peak position shift by 0.5 eV to lower energy, indicating an increase in the concentration of Mn^{3+} ions due to the formation of oxygen vacancies. For the 600 ºC annealed film, the bulk of the film maintains a comparable Mn^{3+}/Mn^{4+} ion concentration ratio as observed in the 400 ºC annealed film (evident from the similar XA shape and peak positions in LY mode). However, an additional shoulder feature (637.3 eV) emerges on the low energy side of the Mn-L_3 main peak, indicating the presence of Mn^{2+} ions. The difference between the TEY and LY mode spectra suggest that a higher concentration of oxygen vacancies exists near the film surface, while the bulk of the film experiences negligible change. In contrast, the LSMO film annealed at 900 ºC exhibits clearly spectral signatures of Mn^{2+} ions within the bulk of the film, as indicated by the notable increase in intensity of the peak at 673.2 eV in LY mode. Meanwhile, the surface layer of the film maintains a similar spectral shape as the LSMO film annealed at 600ºC, as indicated by their comparable XA spectra shape in TEY mode. Ideally, the RP phase ($La_{1.4}Sr_{0.6}MnO_4$) has averaged Mn valence state of +2.6, which is higher than the valence state of BM phase ($La_{0.67}Sr_{0.33}MnO_{2.5}$) where Mn^{2+} ions dominant. Therefore, it is possible that the RP phase forms preferentially at the film surface while the BM phase exists predominantly in the bulk of the film. It should be noted that both BM and RP phases are not the equilibrium phases and prolonged exposure of the samples to air at room temperature might also contribute to the oxidation of the film surface.

Figure 6.7 shows that the AG and vacuum annealed LSMO films display Mn-XMCD signals with lineshapes consistent with the double exchange mechanism involving Mn^{3+}/Mn^{4+} ions. In the case of the LSMO film annealed at 400 ºC, the FM signal from the surface is notably weaker

than that of the bulk, suggesting that at lower annealing temperatures, oxygen vacancy formation primarily occurs at the film's surface, while the bulk retains its original properties. In contrast, the 900 ºC annealed film, characterized by a mixture of BM and RP phases, presents the opposite behavior where the bulk film exhibits diminished ferromagnetism, while the surface shows a more pronounced Mn-XMCD signal. Previous reports have indicated that $La_{0.7}Sr_{0.3}MnO_{2.5}$ (BM phase) possesses non-FM or weak-FM properties, while the n=1 RP phase was usually characterized by AFM or spin-glass (SG) behaviors [203,211–213]. Hence, the observed ferromagnetism in this film emerges as a result of the interplay between AFM and FM orderings associated with different phases within the film. However, the XMCD results do not align well with *M(T)* curves as shown in **Figure 6.5**, where the 900 ºC is non-FM. The ferromagnetism could also come from the surface oxidation for the film expose in air and x-rays. To gain a comprehensive understanding of the precise structural configuration and the percentage of each phase, more sophisticated experimental investigations will be essential in future studies.

In order to probe the AFM properties of the LSFO films, XA/XMLD spectra at the Fe *L*-edge were acquired for both the AG-LSFO and annealed samples using TEY mode at 80 K, as shown in **Figure 6.8** (a). With the incident x-rays at a 30º angle from the sample surface with the projection along the [100] direction, the XMLD spectra was calculated as the difference between spectra acquired with the ***E***-vector aligned with the in-plane [010] direction vs. 30º away from the out-of-plane [001] direction. While the shapes of the Fe-XA spectra remain almost identical across all samples, subtle shifts (0.1 eV) of the L_3 peak position toward lower energy are discernible in the 600 ºC and 900 ºC annealed films. These shifts suggest a slightly increased concentration of Fe^{3+} ions due to the formation of oxygen vacancies. XMLD spectra provide

insights into any asymmetries such as charge distribution around the Fe ions stemming from AFM ordering, orbital ordering ($d_{x^2-y^2}$ vs. d_{z^2} orbitals), and structural asymmetries [167]. The Fe-XMLD spectra of the AG-LSFO film indicates an out-of-plane canting of the AFM spin axis [52], while the inversed shape of the annealed films implies that the AFM spin-axis is confined to the in-plane direction [214].

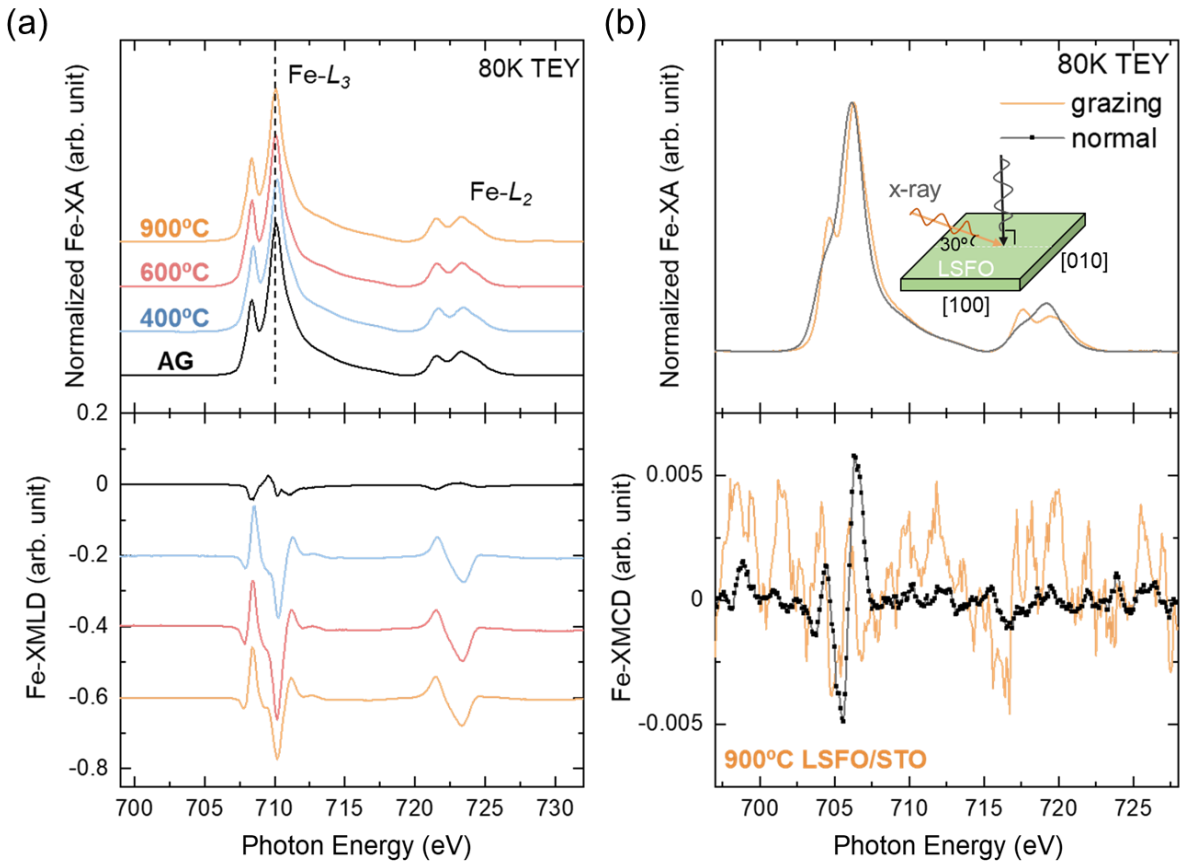

Figure 6.8 Fe *L*-edge (a) XA/XMLD spectra of AG and vacuum annealed LSFO thin films measured at TEY mode. XA/XMLD spectra are vertically shifted for clarity. (b) XA/XMCD spectra of LSFO thin film vacuum annealed at 900 ºC and measured in grazing and normal incidence. XA spectra are normalized from 0 to 1.

For the LSFO film annealed at 900 ºC, Fe-XA/XMCD spectra were obtained using both grazing and normal incidence x-rays, as shown in **Figure 6.8** (b). Interestingly, a weak Fe-XMCD signal (around two orders of magnitude smaller than Mn-XMCD) can be observed for measurements performed at normal incidence, while no such signal was found above the noise level for grazing incident measurements. This result may suggest a weak FM phase with its magnetic easy axis oriented in the out-of-plane direction. In contrast, the film's main matrix predominantly retains AFM ordering, with the spin axis directed along the in-plane directions.

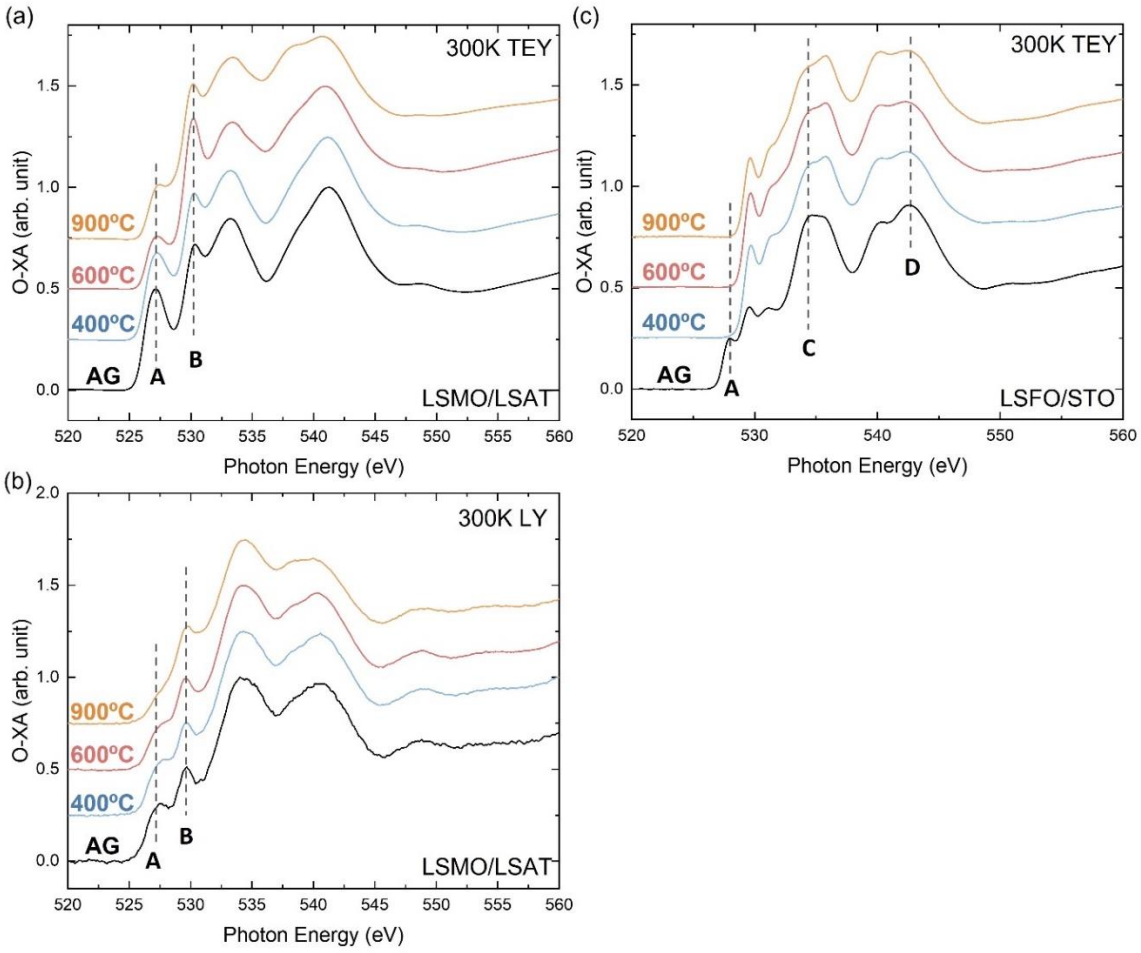

Figure 6.9 O *K*-edge XA spectra of LSMO/LSAT films in (a) TEY mode and (b) LY mode, and (c) LSFO/STO films taken in TEY mode at 300 K. Spectra are vertically shifted for clarity.

Figure 6.9 (a) and (b) present O *K*-edge XA spectra of LSMO/LSAT films, measured at 300 K using TEY and LY detection modes, respectively. The pre-peak around 527 eV, labeled as "A", signifies the hybridization between O 2*p* and Mn 3*d* orbitals within an octahedral coordination environment, while peak "B" is sensitive to the valence state of Mn ions. The decreasing intensity of peaks A and B as the annealing temperature increases indicates an increase in the oxygen vacancy concentration and reduced Mn valence states at both the film's surface and bulk, correlated with the increase in Mn^{2+} and Mn^{3+} ion concentrations as shown in **Figure 6.7**. **Figure 6.9** (c) shows O *K*-edge XA spectra of LSFO/STO films in TEY mode. The absence of peak A in all the annealed films, in comparison to the AG-LSFO film, indicates the presence of oxygen vacancies. Despite nearly identical spectral shapes across all annealed films, a subtle decreasing trend in peaks C and D is observed, suggesting an increasing proportion of Fe^{3+} ions, aligning with the XA spectra shown in **Figure 6.8** (a) [45].

6.4. Conclusions

Figure 6.10 summarizes the extend of topotactic transformations observed in LSMO and LSFO films upon vacuum annealing as compared to previous reports for LSCO films. For LSMO films, a notable phase transformation beyond the FM/M OD-P phase only occurs at the highest temperature explored in this study (900 ºC), where a mixed phase comprising of the BM and RP structures emerges. This mixed phase exhibits weak ferromagnetism observed from *M(T)* measurements coupled with insulating behavior. In contrast, topotactic transformations are absent in all annealed LSFO films with the films maintaining their OD-P phase regardless of the annealing temperature. The Fe-XA spectra shows almost identical peak shapes, while Fe-XMLD spectra change signs along with higher intensity for the annealed films, and the O K-edge XA

spectra also shows different pre-peak intensities. The 900 ºC annealed LSFO film displayed a profound change in its magnetic ordering and resistivity, showing extremely weak FM properties with an out-of-plane easy axis that embedded in an AFM matrix with its spin axis along the in-plane direction and overall metallic behavior. For both LSMO and LSFO films, the annealing process resulted in an increase in oxygen vacancy concentration, accompanied by a reduction in the valence states of transition metal ions to uphold charge neutrality.

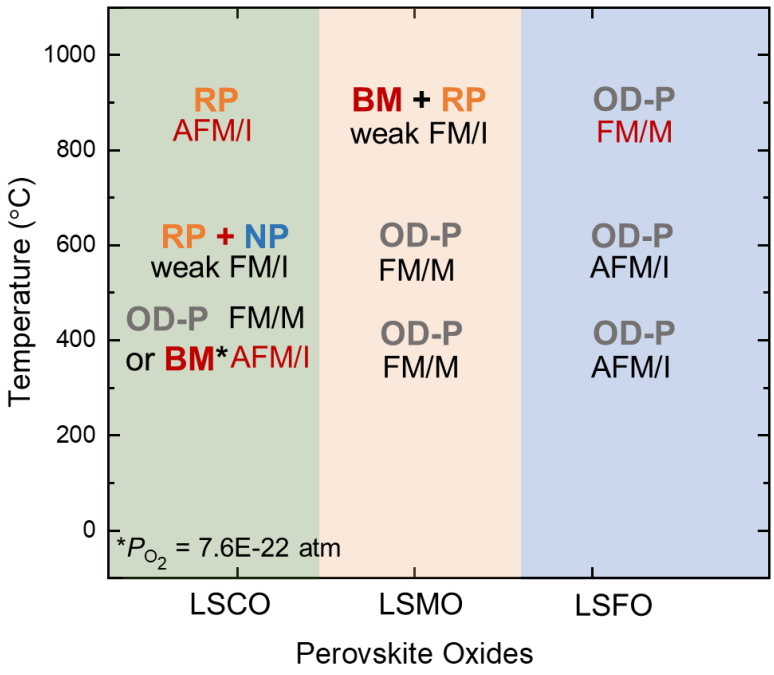

Figure 6.10 Phase map of LSCO, LSMO, LSFO films as a function of vacuum annealing temperature. All films (except the one with "*") were annealed with oxygen partial pressure at 7.6×10^{-10} Torr for 1 hour. The name of the reducing phases and corresponding magnetic and electrical properties are marked on the map. M: metallic; I: insulating.

Despite similar ionic conductivity across cobaltite, manganite, and ferrite bulk materials [202,206], the disparate behaviors among these materials imply the strong influence of

other factors, such as surface reaction kinetics, oxygen formation energy, and the stability of reducing phases, which contribute to distinct phase transformations. Further experimental and computational endeavors are required to unravel these distinctions. Grasping the diverse behaviors of these materials sets the foundation for deeper investigations into MIT transitions, and for the identification of potential candidates for future neuromorphic computing devices.

Chapter 7

Conclusions and Future Work

7.1. Conclusions

This dissertation explores functional properties of lanthanum-based complex oxides, focusing on interfacial exchange coupling and topotactic phase transformations. It investigates how magnetic anisotropy changes with epitaxial strain and film thickness, then reveals insights into the exchange bias (EB) effect of $La_{2/3}Sr_{1/3}CoO_3$ (LSCO)/$La_{2/3}Sr_{1/3}MnO_3$ (LSMO) bilayers. Additionally, the studies present the impact of different reducing conditions (hydrogen vs. vacuum at different temperatures) on topotactic phase transformations. These findings contribute to our understanding of structure and functional properties of the complex oxides and their potential applications in magnetic memory devices and neuromorphic computing.

Synchrotron soft x-ray magnetic spectroscopy are essential techniques to understand the bonding configurations, preferred electron occupancy, valence states and magnetic ordering of complex oxides. More importantly, it can distinguish ferromagnetic (FM) signals from different magnetic elements. In Chapter 3, x-ray absorption (XA) and x-ray magnetic circular dichroism (XMCD) spectroscopy revealed that magnetically active Co^{2+} ions from LSCO layer that strongly coupled to the LSMO layer were observed below a critical LSCO thickness (T_{LSCO}) for LSCO/LSMO bilayers grown on $LaAlO_3$ (LAO) and $NdGaO_3$ (NGO) substrates. In particular, T_{LSCO} was found

to be 2 nm on LAO substrates while it was 4 nm on NGO substrates. Above T_{LSCO}, the formation of Co^{2+} ions was quickly suppressed leaving only a soft LSCO layer with mixed valence Co^{3+}/Co^{4+} ions for bilayers on LAO substrates, and only a hard bulk-like LSCO layer on NGO substrates. By comparing the functional properties of LSCO/LSMO bilayers on these two substrates, it was found that the impact of compressive strain (-1% for LSCO, -2% for LSMO on LAO substrates) is more pronounced, strongly hinders the EB effect between LSCO and LSMO layers due to similar coercive fields.

Based on the results from Chapter 3, NGO substrate is an ideal platform to investigate the magnetic anisotropy and EB effect of the bilayer system due to its different in-plane lattice parameters (a_{pc}=3.855 Å, b_{pc}=3.863 Å). In Chapter 4, XMCD hysteresis loops revealed that for LSCO thickness (t_{LSCO}) ≤ 4 nm, the easy axes for both LSCO and LSMO layers were along the $[001]_o$ direction and the LSCO layer was characterized by magnetically active Co^{2+} ions that strongly coupled to the LSMO layer. No EB effect was observed in the hysteresis loops. In contrast, along the $[1\bar{1}0]_o$ direction, the LSCO and LSMO layers displayed a small difference in their coercivity values, and a small EB shift was observed. As t_{LSCO} increased above 4 nm, the easy axis for the LSCO layer remained along the $[100]_o$ direction, but it gradually rotated to the $[1\bar{1}0]_o$ direction for the LSMO layer, resulting in a large negative EB shift. In addition, with direct correlation to in-plane anisotropy, Mn-edge x-ray linear dichroism (XLD) showed different electron occupancy along the two in-plane directions with increasing t_{LSCO}. Hence, the fusion of Chapter 3 and 4 delved into manipulating magnetocrystalline anisotropy and EB effect through the adjustment of interfacial exchange coupling between two FM perovskite oxide layers.

The ability to manipulate EB effect of FM heterostructures, makes them promising candidates for next-generation spintronic and magnetic memory devices.

The topotactic phase transformations introduced in Chapter 5 show the ability to control the physical properties of LSCO thin films upon annealing in a pressurized hydrogen environment. The emergence of the brownmillerite (BM) phase with characteristics of antiferromagnetic (AFM) and insulating behavior was only achieved at intermediate temperatures from 170 ºC to 300 ºC, where a dual-ion exchange mechanism involving the loss of O^{2-} ions and the insertion of H^{+} ions was proposed. An interesting observation was the preservation of the perovskite structure at higher hydrogenation temperatures (from 300 ºC to 400 ºC), instead of forming more reduced phases. For the high-temperature hydrogenated perovskite film, the magnetization was suppressed and resistivity increased significantly, signifying the presence of a limited number of disordered oxygen vacancies and the H ions in the lattice that impede the double exchange interactions between Co ions.

Chapter 6 conducted a comparative analysis of topotactic phase transformations and associated functional properties in LSMO and $La_{0.7}Sr_{0.3}FeO_3$ (LSFO) thin films during vacuum annealing. Notably, LSMO thin films exhibited substantial phase transitions, manifesting a mixed phase with BM and Ruddlesden-Popper (RP) phases at the highest annealing temperature (900 ºC), resulting in weak ferromagnetism and insulating behavior. Conversely, LSFO films experienced no observable phase changes throughout the annealing conditions used, consistently maintaining their oxygen-deficient perovskite (OD-P) structure (shown in XRD profiles). However, the 900ºC annealed LSFO film displayed a remarkable shift in its functional properties, exhibiting

extremely weak magnetism along with AFM ordering and overall metallic behavior. Oxygen vacancy concentrations increased with annealing temperature for both LSMO and LSFO films, accompany with a decrease in the valence states of transition metal ions to maintain charge neutrality. While cobaltite, manganite, and ferrite bulk materials share similar ionic conductivity, the distinct behaviors highlight the potential influence of factors such as oxygen formation energy, surface reaction kinetics, and reducing phase stability on phase transformations, which requires more surface sensitive measurements to be explored. The exploration of these materials provides valuable insights into the complex interplay between structural and functional changes during topotactic phase transformations and offers new paths for selecting candidates with tailored properties for advanced applications in neuromorphic computing.

7.2 Future Work

7.2.1 Topotactic Phase Control via Pulsed Laser Deposition

The direct synthesis of reducing phases using pulsed laser deposition (PLD) can be an alternative to external stimuli like thermal annealing or applied voltages. Oxygen partial pressure (p_{O_2}) during PLD growth is a crucial parameter governing the stoichiometry of complex oxide thin films. Although various studies have explored the influence of p_{O_2} on film properties, few have reported the observation of phase transformations [174,215–217]. Preliminary results indicate that, under specific p_{O_2} conditions, the perovskite phase of LSCO can transform into multiple reduced phases, as shown in the XRD plot in **Figure 7.1**. For single-layer LSCO on LSAT substrate, a stoichiometric film can be obtained with p_{O_2} = 0.3 Torr. Decreasing p_{O_2} during PLD growth leads to transformations into OD-P, RP, or amorphous phases. Additionally, when depositing LSCO/LCO heterostructures, a mixed BM and RP phase can be achieved. The

formation of RP phase cobaltite thin films directly through PLD growth has not been reported before. Given the insulating nature of RP phase cobaltites, the successful synthesis opens up opportunities for creating metallic/insulating heterostructures via direct thin-film fabrication, eliminating the need for external stimuli. Further investigation into the intricacies of such direct PLD synthesis could yield valuable insights for tailoring materials with specific properties for advanced applications.

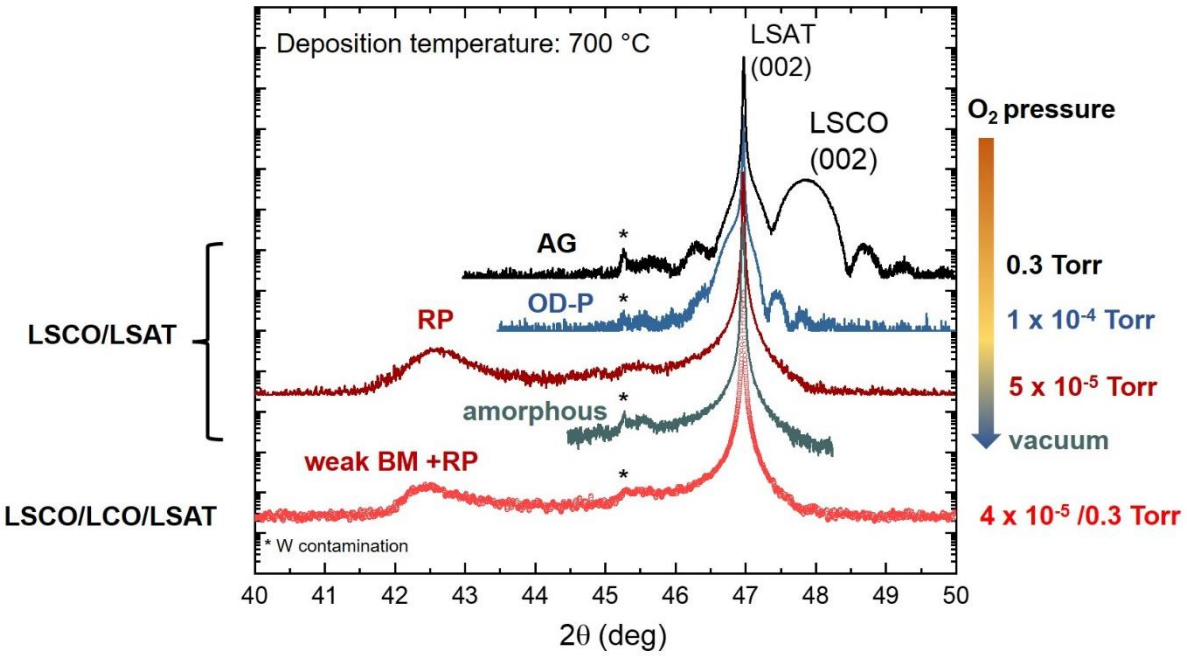

Figure 7.1 XRD profiles of LSCO and LSCO/LCO thin films grown under different oxygen pressures at 700 ºC. p_{O_2} values during PLD growth are labeled on the right side of the XRD plot.

7.2.2 *In-situ* Experiments on Hydrogenation Process

In Chapter 5, the unconventional preservation of the perovskite structure in high-temperature hydrogenated LSCO thin films, without transitioning into reducing phases, raises intriguing questions about the underlying mechanisms. It remains uncertain whether intermediate phases

play a role in this process or if there are no phase changes throughout the hydrogenation. To address these questions, conducting *in-situ* experiments becomes imperative for gaining insights into any phase transformations occurring during hydrogenation/thermal annealing process. *In-situ* x-ray diffraction (XRD) has proven valuable for studying transitions between perovskite and BM phases in other complex oxides such as $SrCoO_x$ (SCO) and LSMO films, as a function of applied voltage or annealing temperature [179,185]. Furthermore, *in-situ* x-ray photoemission spectroscopy (XPS) can elucidate changes in the valence states of transition metal ions, as demonstrated in the study of Ni ions where the evolution of valence state changes were observed based on hydrogenation time and temperatures [218]. By employing *in-situ* experiments, we can also explore the possibility of unstable intermediate phases forming during the process, which may not be readily observable in the final state. This approach promises a deeper understanding of the intricate phase transformations occurring during the hydrogenation/thermal annealing process, providing controls over functional properties of the complex oxides.

7.2.3 Strain-Engineered Topotactic Phase Transformations

In Chapter 3, I observed the significant impact of strain state on magnetic and electrical behaviors. Chapters 5 and 6 of this dissertation delved into the topotactic phase transformations of LSCO, LSMO, and LSFO thin films, grown on selected substrates to minimize lattice strain with origin perovskite structure. However, the strain state can change upon topotactic phase transformations. Therefore, it's unclear how lattice strain affects the phase changes if we choose to use substrates with a better lattice mismatch to the reduced phases, and there are only few studies dedicated to manipulating strain states to explore the phase transformations of transition metal oxides. The distinct ordering of oxygen vacancies within the BM phase of LSCO and

LSMO films when subjected to either compressive or tensile strain was reported [14,219]. This phenomenon highlights the profound impact that strain can lead to structural changes of these materials and providing possibilities for tailoring their properties via precise control of strain states.

Bibliography

[1] P. D. Battle, D. E. Cox, M. A. Green, J. E. Millburn, L. E. Spring, P. G. Radaelli, M. J. Rosseinsky, and J. F. Vente, *Antiferromagnetism, Ferromagnetism, and Phase Separation in the GMR System $Sr_{2-x}La_{1+x}Mn_2O_7$*, Chemistry of Materials **9**, 1042 (1997).

[2] J. Wu and C. Leighton, *Glassy Ferromagnetism and Magnetic Phase Separation in $La_{1-x}Sr_xCoO_3$*, Phys Rev B **67**, 174408 (2003).

[3] N. Lu et al., *Electric-Field Control of Tri-State Phase Transformation with a Selective Dual-Ion Switch*, Nature **546**, 124 (2017).

[4] J. D. Ferguson, Y. Kim, L. F. Kourkoutis, A. Vodnick, A. R. Woll, D. A. Muller, and J. D. Brock, *Epitaxial Oxygen Getter for a Brownmillerite Phase Transformation in Manganite Films*, Advanced Materials **23**, 1226 (2011).

[5] P. G. Radaelli, G. Iannone, M. Marezio, H. Y. Hwang, S.-W. Cheong, J. D. Jorgensen, and D. N. Argyriou, *Structural Effects on the Magnetic and Transport Properties of Perovskite $A_{1-x}A'_xMnO_3$ (X=0.25, 0.30)*, Phys Rev B **56**, 8265 (1997).

[6] S. Zhang, H. Vo, and G. Galli, *Predicting the Onset of Metal-Insulator Transitions in Transition Metal Oxides - A First Step in Designing Neuromorphic Devices*, Chemistry of Materials **33**, 3187 (2021).

[7] J. Chen et al., *Revealing the Role of Lattice Distortions in the Hydrogen-Induced Metal-Insulator Transition of $SmNiO_3$*, Nat Commun **10**, 694 (2019).

[8] A. Ohtomo and H. Y. Hwang, *A High-Mobility Electron Gas at the $LaAlO_3/SrTiO_3$ Heterointerface*, Nature **427**, 423 (2004).

[9] D. Li, K. Lee, B. Y. Wang, M. Osada, S. Crossley, H. R. Lee, Y. Cui, Y. Hikita, and H. Y. Hwang, *Superconductivity in an Infinite-Layer Nickelate*, Nature **572**, 624 (2019).

[10] H. M. Christen and G. Eres, *Recent Advances in Pulsed-Laser Deposition of Complex Oxides*, Journal of Physics Condensed Matter **20**, 264005 (2008).

[11] D. H. Lowndes, D. B. Geohegan, A. A. Puretzky, D. P. Norton, and C. M. Rouleau, *Synthesis of Novel Thin-Film Materials by Pulsed Laser Deposition*, Science **273**, 898 (1996).

[12] S. Wu et al., *Prototype Design of a Domain-Wall-Based Magnetic Memory Using a Single Layer $La_{0.67}Sr_{0.33}MnO_3$ Thin Film*, ACS Appl Mater Interfaces **13**, 23945 (2021).

[13] Z. Liao et al., *Controlled Lateral Anisotropy in Correlated Manganite Heterostructures by Interface-Engineered Oxygen Octahedral Coupling*, Nat Mater **15**, 425 (2016).

[14] V. Chaturvedi et al., *Doping- And Strain-Dependent Electrolyte-Gate-Induced Perovskite to Brownmillerite Transformation in Epitaxial $La_{1-x}Sr_xCoO_{3-\delta}$ Films*, ACS Appl Mater Interfaces **13**, 51205 (2021).

[15] A. Hoffmann et al., *Quantum Materials for Energy-Efficient Neuromorphic Computing: Opportunities and Challenges*, APL Mater **10**, 070904 (2022).

[16] M. Bibes, J. E. Villegas, and A. Barthélèmy, *Ultrathin Oxide Films and Interfaces for Electronics and Spintronics*, Adv Phys **60**, 5 (2011).

[17] D. Pantel, S. Goetze, D. Hesse, and M. Alexe, *Reversible Electrical Switching of Spin Polarization in Multiferroic Tunnel Junctions*, Nat Mater **11**, 289 (2012).

[18] J. M. Rondinelli and C. J. Fennie, *Octahedral Rotation-Induced Ferroelectricity in Cation Ordered Perovskites*, Advanced Materials **24**, 1961 (2012).

[19] V. M. Goldschmidt, *Die Gesetze Der Krystallochemie*, Naturwissenschaften **14**, 477 (1926).

[20] J. M. Rondinelli and N. A. Spaldin, *Structure and Properties of Functional Oxide Thin Films: Insights from Electronic-Structure Calculations*, Advanced Materials **23**, 3363 (2011).

[21] J. Li et al., *Topotactic Phase Transformations by Concerted Dual-Ion Migration of B-Site Cation and Oxygen in Multivalent Cobaltite La–Sr–Co–O_x Films*, Nano Energy **78**, 105215 (2020).

[22] A. Grimaud, C. E. Carlton, M. Risch, W. T. Hong, K. J. May, and Y. Shao-Horn, *Oxygen Evolution Activity and Stability of $Ba_6Mn_5O_{16}$, $Sr_4Mn_2CoO_9$, and $Sr_6Co_5O_{15}$: The Influence of Transition Metal Coordination*, Journal of Physical Chemistry C **117**, 25926 (2013).

[23] G. Van Der Laan, E. Arenholz, R. V Chopdekar, and Y. Suzuki, *Influence of Crystal Field on Anisotropic X-Ray Magnetic Linear Dichroism at the Co^{2+} $L_{2,3}$ Edges*, Phys Rev B **77**, 064407 (2008).

[24] C. F. Chang et al., *Spin Blockade, Orbital Occupation, and Charge Ordering in $La_{1.5}Sr_{0.5}CoO_4$*, Phys Rev Lett **102**, 116401 (2009).

[25] D. Fuchs, M. Merz, P. Nagel, R. Schneider, S. Schuppler, and H. Von Löhneysen, *Double Exchange via t_{2g} Orbitals and the Jahn-Teller Effect in Ferromagnetic $La_{0.7}Sr_{0.3}CoO_3$ Probed by Epitaxial Strain*, Phys Rev Lett **111**, 257203 (2013).

[26] F. Tsui, M. C. Smoak, T. K. Nath, and C. B. Eom, *Strain-Dependent Magnetic Phase Diagram of Epitaxial $La_{0.67}Sr_{0.33}MnO_3$ Thin Films*, Appl Phys Lett **76**, 2421 (2000).

[27] Y. Konishi, Z. Fang, M. Izumi, T. Manako, M. Kasai, H. Kuwahara, M. Kawasaki, K. Terakura, and Y. Tokura, *Orbital-State-Mediated Phase-Control of Manganites*, J Physical Soc Japan **68**, 3790 (1999).

[28] R. Jungblut, R. Coehoorn, M. T. Johnson, J. Aan De Stegge, and A. Reinders, *Orientational Dependence of the Exchange Biasing in Molecular-Beam-Epitaxy-Grown $Ni_{80}Fe_{20}/Fe_{50}Mn_{50}$ Bilayers*, J Appl Phys **75**, 6659 (1994).

[29] P. W. Anderson and H. Hasegawa, *Considerations on Double Exchange*, Physical Review **100**, 675 (1955).

[30] M. Opel, *Spintronic Oxides Grown by Laser-MBE*, J Phys D Appl Phys **45**, 033001 (2012).

[31] R. I. Dass and J. B. Goodenough, *Multiple Magnetic Phases of $La_2CoMnO_{6-\delta}$ ($0 \leq \delta \leq 0.05$)*, Phys Rev B **67**, 0144011 (2003).

[32] M. Sharma, J. Gazquez, M. Varela, J. Schmitt, and C. Leighton, *Growth Temperature Control of the Epitaxy, Magnetism, and Transport in $SrTiO_3(001)/La_{0.5}Sr_{0.5}CoO_3$ Thin Films*, Journal of Vacuum Science & Technology A **29**, 051511 (2011).

[33] C. Sun, R. Hui, and J. Roller, *Cathode Materials for Solid Oxide Fuel Cells: A Review*, Journal of Solid State Electrochemistry **14**, 1125 (2010).

[34] A. Pérez-Tomás, A. Mingorance, D. Tanenbaum, and M. Lira-Cantú, *Metal Oxides in Photovoltaics: All-Oxide, Ferroic, and Perovskite Solar Cells*, in *The Future of Semiconductor Oxides in Next-Generation Solar Cells* (Elsevier, 2018), pp. 267–356.

[35] J. P. Byers, B. Li, R. V Chopdekar, J. Ditto, D. C. Johnson, Y. Takamura, and N. D. Browning, *Correlation between Epitaxial Strain and Magnetic Properties in $La_{0.7}Sr_{0.3}CoO_3$/ $La_{0.7}Sr_{0.3}MnO_3$ Bilayers*, J Appl Phys **125**, 082518 (2019).

[36] J. E. Davies, J. Wu, C. Leighton, and K. Liu, *Magnetization Reversal and Nanoscopic Magnetic-Phase Separation in $La_{1-x}Sr_xCoO_3$*, Phys Rev B **72**, 134419 (2005).

[37] P. L. Kuhns, M. J. R. Hoch, W. G. Moulton, A. P. Reyes, J. Wu, and C. Leighton, *Magnetic Phase Separation in $La_{1-x}Sr_xCoO_3$ by ^{59}Co Nuclear Magnetic Resonance*, Phys Rev Lett **91**, 127202 (2003).

[38] M. A. Torija, M. Sharma, J. Gazquez, M. Varela, C. He, J. Schmitt, J. A. Borchers, M. Laver, S. El-Khatib, and C. Leighton, *Chemically Driven Nanoscopic Magnetic Phase Separation at the $SrTiO_3(001)/La_{1-x}Sr_xCoO_3$ Interface*, Advanced Materials **23**, 2711 (2011).

[39] N. P. Bansal, R. A. Varin, T. Czujko, and Z. S. Wronski, *Perovskite Oxide for Solid Oxide Fuel Cells* (Springer, Boston, MA, 2009).

[40] D. A. Gilbert et al., *Ionic Tuning of Cobaltites at the Nanoscale*, Phys Rev Mater **2**, 104402 (2018).

[41] I. T. Chiu et al., *Cation and Anion Topotactic Transformations in Cobaltite Thin Films Leading to Ruddlesden-Popper Phases*, Phys Rev Mater **5**, 064416 (2021).

[42] J. Hemberger, A. Krimmel, T. Kurz, H. A. Krug von Nidda, V. Y. Ivanov, A. A. Mukhin, A. M. Balbashov, and A. Loidl, *Structural, Magnetic, and Electrical Properties of Single-Crystalline $La_{1-x}Sr_xMnO_3$ $(0.4<x<0.85)$*, Phys Rev B **66**, 094410 (2002).

[43] W. C. Koehler and E. 0 Wollan, *NEUTRON-DIFFRACTION STUDY OF THE MAGNETIC PROPERTIES OF PEROVSKITE-LIKE COMPOUNDS $LaBO_3$*, J. Phys. Chem. Sotids **2**, 100 (1957).

[44] Y. J. Xie, M. D. Scafetta, E. J. Moon, A. L. Krick, R. J. Sichel-Tissot, and S. J. May, *Electronic Phase Diagram of Epitaxial $La_{1-x}Sr_xFeO_3$ Films*, Appl Phys Lett **105**, 062110 (2014).

[45] M. Abbate et al., *Controlled-Valence Properties of $La_{1-x}Sr_xFeO_3$ and $La_{1-x}Sr_xMnO_3$ Studied by Soft-x-Ray Absorption Spectroscopy*, Phys Rev B **46**, 4511 (1991).

[46] J. Matsuno, T. Mizokawa, A. Fujimori, K. Mamiya, Y. Takeda, S. Kawasaki, and M. Takano, *Photoemission and Hartree-Fock Studies of Oxygen-Hole Ordering in Charge-Disproportionated $La_{1-x}Sr_xFeO_3$*, Phys Rev B **60**, 4605 (1999).

[47] T. Maeder and J. G. Bednorz, *Influence of Oxygen Stoichiometry on Electrical Transport and Magnetic Properties of Doped Perovskite-Type Ferrate and Manganate Single Crystals*, J Eur Ceram Soc **19**, 1507 (1999).

[48] E. Folven, T. Tybell, A. Scholl, A. Young, S. T. Retterer, Y. Takamura, and J. K. Grepstad, *Antiferromagnetic Domain Reconfiguration in Embedded $LaFeO_3$ Thin Film Nanostructures*, Nano Lett **10**, 4578 (2010).

[49] Y. Jia, R. V Chopdekar, P. Shafer, E. Arenholz, Z. Liu, M. D. Biegalski, and Y. Takamura, *Antiferromagnetic Structure of Exchange-Coupled $La_{0.7}Sr_{0.3}FeO_3$ Thin Films Studied Using Angle-Dependent x-Ray Absorption Spectroscopy*, Phys Rev B **96**, 214411 (2017).

[50] Y. Jia, R. V Chopdekar, E. Arenholz, A. T. Young, M. A. Marcus, A. Mehta, and Y. Takamura, *Exchange Coupling in (111)-Oriented $La_{0.7}Sr_{0.3}MnO_3/La_{0.7}Sr_{0.3}FeO_3$ Superlattices*, Phys Rev B **92**, 094407 (2015).

[51] Y. Jia, R. V Chopdekar, E. Arenholz, Z. Liu, M. D. Biegalski, Z. D. Porter, A. Mehta, and Y. Takamura, *Thickness Dependence of Exchange Coupling in (111)-Oriented Perovskite Oxide Superlattices*, Phys Rev B **93**, 104403 (2016).

[52] S. Czekaj, F. Nolting, L. J. Heyderman, P. R. Willmott, and G. Van Der Laan, *Sign Dependence of the X-Ray Magnetic Linear Dichroism on the Antiferromagnetic Spin Axis in $LaFeO_3$ Thin Films*, Phys Rev B **73**, 020401 (2006).

[53] R. C. Devlin, A. L. Krick, R. J. Sichel, A. Phys Lett, R. J. Sichel-Tissot, Y. J. Xie, and S. J. May, *Electronic Transport and Conduction Mechanism Transition in $La_{1/3}Sr_{2/3}FeO_3$ Thin Films*, J Appl Phys **115**, 233704 (2014).

[54] Y. Zhu, J. Hoffman, C. E. Rowland, H. Park, D. A. Walko, J. W. Freeland, P. J. Ryan, R. D. Schaller, A. Bhattacharya, and H. Wen, *Unconventional Slowing down of Electronic Recovery in Photoexcited Charge-Ordered $La_{1/3}Sr_{2/3}FeO_3$*, Nat Commun **9**, 1799 (2018).

[55] A. L. Krick, C. W. Lee, R. J. Sichel-Tissot, A. M. Rappe, and S. J. May, *Interplay between Cation and Charge Ordering in $La_{1/3}Sr_{2/3}FeO_3$ Superlattices*, Adv Electron Mater **2**, 1500372 (2016).

[56] Y. Xie, M. D. Scafetta, R. J. Sichel-Tissot, E. J. Moon, R. C. Devlin, H. Wu, A. L. Krick, and S. J. May, *Control of Functional Responses via Reversible Oxygen Loss in $La_{1-x}Sr_xFeO_{3-\delta}$ Films*, Advanced Materials **26**, 1434 (2014).

[57] Z. Shen et al., *Increased Activity in the Oxygen Evolution Reaction by Fe^{4+}-Induced Hole States in Perovskite $La_{1-x}Sr_xFeO_3$*, J Mater Chem A Mater **8**, 4407 (2020).

[58] W. H. Meiklejohn and C. P. Bean, *New Magnetic Anisotropy*, Phys. Rev. **105**, 904 (1957).

[59] W. H. Meiklejohn and C. P. Bean, *New Magnetic Anisotropy*, Phys. Rev. **102**, 1413 (1956).

[60] J. Nogués and I. K. Schuller, *Exchange Bias*, J Magn Magn Mater **192**, 203 (1999).

[61] M. Tsunoda, Y. Tsuchiya, T. Hashimoto, and M. Takahashi, *Magnetic Anisotropy and Rotational Hysteresis Loss in Exchange Coupled Ni–Fe/Mn–Ir Films*, J Appl Phys **87**, 4375 (2000).

[62] E. E. Fullerton, J. Jiang, M. Grimsditch, C. Sowers, and S. Bader, *Exchange-Spring Behavior in Epitaxial Hard/Soft Magnetic Bilayers*, Phys Rev B **58**, 12193 (1998).

[63] E. E. Fullerton, J. S. Jiang, and S. D. Bader, *Hard/Soft Magnetic Heterostructures: Model Exchange-Spring Magnets*, J Magn Magn Mater **200**, 392 (1999).

[64] E. F. Kneller and R. Hawig, *The Exchange-Spring Magnet: A New Material Principle for Permanent Magnets*, IEEE Trans Magn **27**, 3588 (1991).

[65] Z. Wei, A. Sharma, A. S. Nunez, P. M. Haney, R. A. Duine, J. Bass, A. H. MacDonald, and M. Tsoi, *Changing Exchange Bias in Spin Valves with an Electric Current*, Phys Rev Lett **98**, 116603 (2007).

[66] J. U. Thiele, S. Maat, and E. E. Fullerton, *FeRh/FePt Exchange Spring Films for Thermally Assisted Magnetic Recording Media*, Appl Phys Lett **82**, 2859 (2003).

[67] J. U. Thiele, S. Maat, J. L. Robertson, and E. E. Fullerton, *Magnetic and Structural Properties of FePt-FeRh Exchange Spring Films for Thermally Assisted Magnetic Recording Media*, in *IEEE Transactions on Magnetics*, Vol. 40 (2004), pp. 2537–2542.

[68] R. Morales, A. C. Basaran, J. E. Villegas, D. Navas, N. Soriano, B. Mora, C. Redondo, X. Batlle, and I. K. Schuller, *Exchange-Bias Phenomenon: The Role of the Ferromagnetic Spin Structure*, Phys Rev Lett **114**, 097202 (2015).

[69] M. Y. Khan, C. Bin Wu, and W. Kuch, *Pinned Magnetic Moments in Exchange Bias: Role of the Antiferromagnetic Bulk Spin Structure*, Phys Rev B **89**, 094427 (2014).

[70] H. Ohldag, A. Scholl, F. Nolting, E. Arenholz, S. Maat, A. T. Young, M. Carey, and J. Stöhr, *Correlation between Exchange Bias and Pinned Interfacial Spins*, Phys Rev Lett **91**, 017203 (2003).

[71] J. Nogués, D. Lederman, T. J. Moran, and I. K. Schuller, *Positive Exchange Bias in FeF_2-Fe Bilayers*, Phys Rev Lett **76**, 4624 (1996).

[72] A. K. Suszka, O. Idigoras, E. Nikulina, A. Chuvilin, and A. Berger, *Crystallography-Driven Positive Exchange Bias in Co/CoO Bilayers*, Phys Rev Lett **109**, 177205 (2012).

[73] T. Hong, *Simple Mechanism for a Positive Exchange Bias*, Phys Rev B **58**, 97 (1998).

[74] D. A. Gilbert, J. Olamit, R. K. Dumas, B. J. Kirby, A. J. Grutter, B. B. Maranville, E. Arenholz, J. A. Borchers, and K. Liu, *Controllable Positive Exchange Bias via Redox-Driven Oxygen Migration*, Nat Commun **7**, 11050 (2016).

[75] B. Li, R. V Chopdekar, E. Arenholz, A. Mehta, and Y. Takamura, *Unconventional Switching Behavior in $La_{0.7}Sr_{0.3}MnO_3/La_{0.7}Sr_{0.3}CoO_3$ Exchange-Spring Bilayers*, Appl Phys Lett **105**, 202401 (2014).

[76] B. Li, R. V. Chopdekar, A. T. N'Diaye, A. Mehta, J. P. Byers, N. D. Browning, E. Arenholz, and Y. Takamura, *Tuning Interfacial Exchange Interactions via Electronic Reconstruction in Transition-Metal Oxide Heterostructures*, Appl Phys Lett **109**, 152401 (2016).

[77] E. Dagotto, T. Hotta, and A. Moreo, *Colossal Magnetoresistant Materials: The Key Role of Phase Separation*, Physics Report **344**, 1 (2001).

[78] M. Huijben, G. Koster, Z. L. Liao, and G. Rijnders, *Interface-Engineered Oxygen Octahedral Coupling in Manganite Heterostructures*, Appl Phys Rev **4**, 041103 (2017).

[79] P. Yu, Y. H. Chu, and R. Ramesh, *Oxide Interfaces: Pathways to Novel Phenomena*, Materials Today.

[80] A. M. Kane, R. V Chopdekar, A. T. N'Diaye, A. Scholl, E. Arenholz, A. Mehta, and Y. Takamura, *Decoupling Exchange Bias and Coercivity Enhancement in a Perovskite Oxide Exchange Spring Bilayer*, Phys Rev Mater **3**, 014413 (2019).

[81] A. M. Kane, I. T. Chiu, N. J. Ahlm, R. V. Chopdekar, A. T. N'diaye, E. Arenholz, A. Mehta, V. Lauter, and Y. Takamura, *Controlling Magnetization Vector Depth Profiles of $La_{0.7}Sr_{0.3}CoO_3/La_{0.7}Sr_{0.3}MnO_3$ Exchange Spring Bilayers via Interface Reconstruction*, ACS Appl Mater Interfaces **12**, 45437 (2020).

[82] B. Li, R. V Chopdekar, A. M. Kane, K. Hoke, A. T. N'Diaye, E. Arenholz, and Y. Takamura, *Thickness-Dependent Magnetic and Electrical Transport Properties of Epitaxial $La_{0.7}Sr_{0.3}CoO_3$ Films*, AIP Adv **7**, 045003 (2017).

[83] A. M. Haghiri-Gosnet, J. Wolfman, B. Mercey, C. Simon, P. Lecoeur, M. Korzenski, M. Hervieu, R. Desfeux, and G. Baldinozzi, *Microstructure and Magnetic Properties of Strained $La_{0.7}Sr_{0.3}MnO_3$ Thin Films*, J Appl Phys **88**, 4257 (2000).

[84] S. A. Chambers, *Epitaxial Growth and Properties of Doped Transition Metal and Complex Oxide Films*, Advanced Materials **22**, 219 (2010).

[85] *Pulsed Laser Deposition*, http://groups.ist.utl.pt/rschwarz/rschwarzgroup_files/PLD_files/PLD.htm.

[86] J. Ihlemann, A. Scholl, H. Schmidt, and B. Wolff-Rottke, *Nanosecond and Femtosecond Excimer-Laser Ablation of Oxide Ceramics*, Applied Physics A **60**, 411 (1995).

[87] L. M. Doeswijk, G. Rijnders, and D. H. A. Blank, *Pulsed Laser Deposition: Metal versus Oxide Ablation*, Applied Physics A **78**, 263 (2004).

[88] T. Ohnishi, T. Yamamoto, S. Meguro, H. Koinuma, and M. Lippmaa, *Pulsed Laser Ablation and Deposition of Complex Oxides*, J Phys Conf Ser **59**, 514 (2007).

[89] G. Koster, D. H. A. Blank, and G. A. J. H. M. Rijnders, *Oxygen in Complex Oxide Thin Films Grown by Pulsed Laser Deposition: A Perspective*, J Supercond Nov Magn **33**, 205 (2020).

[90] Z. G. Zhang, F. Zhou, X. Q. Wei, M. Liu, G. Sun, C. S. Chen, C. S. Xue, H. Z. Zhuang, and B. Y. Man, *Effects of Oxygen Pressures on Pulsed Laser Deposition of ZnO Films*, Physica E **39**, 253 (2007).

[91] R. Perez-Casero, J. Perrière, A. Gutierrez-Llorente, D. Defourneau, E. Millon, W. Seiler, and L. Soriano, *Thin Films of Oxygen-Deficient Perovskite Phases by Pulsed-Laser Ablation of Strontium Titanate*, Phys Rev B **75**, 165317 (2007).

[92] M. A. El Khakani, B. Le Drogoff, and M. Chaker, *Effect of the Deposition Temperature on the Properties of Iridium Thin Films Grown by Means of Pulsed Laser Deposition*, J Mater Res **14**, 3241 (1999).

[93] N. Kumar, S. Prasad, D. S. Misra, N. Venkataramani, M. Bohra, and R. Krishnan, *The Influence of Substrate Temperature and Annealing on the Properties of Pulsed Laser-Deposited YIG Films on Fused Quartz Substrate*, J Magn Magn Mater **320**, 2233 (2008).

[94] R. Kek, K. C. Tan, C. H. Nee, S. L. Yap, S. F. Koh, A. K. B. H. M. Arof, T. Y. Tou, and S. S. Yap, *Effects of Pressure and Substrate Temperature on the Growth of Al-Doped ZnO Films by Pulsed Laser Deposition*, Mater Res Express **7**, 016414 (2019).

[95] V. Gabriel, P. Kocán, S. Bauer, B. Nergis, A. Rodrigues, L. Horák, X. Jin, R. Schneider, T. Baumbach, and V. Holý, *Effect of Pulse Laser Frequency on PLD Growth of $LuFeO_3$ Explained by Kinetic Simulations of in-Situ Diffracted Intensities*, Sci Rep **12**, 5647 (2022).

[96] G. A. Govindassamy, J. J. Prentice, J. G. Lunney, R. W. Eason, and J. I. Mackenzie, *Effect of Laser Repetition Rate on the Growth of Sc_2O_3 via Pulsed Laser Deposition*, Applied Physics A **128**, 577 (2022).

[97] A. Rockett, *The Materials Science of Semiconductors* (Springer US, 2008).

[98] A. Rockett, *The Materials Science of Semiconductors* (Springer US, 2008).

[99] T. F. Kuech, *Integration of Dissimilar Materials* (Elsevier, Amsterdam, 2011).

[100] J. E. Prieto and I. Markov, *Stranski–Krastanov Mechanism of Growth and the Effect of Misfit Sign on Quantum Dots Nucleation*, Surf Sci **664**, 172 (2017).

[101] A. Gibaud, M. S. Chebil, and T. Beuvier, *X-Ray Reflectivity*, Springer Series in Surface Sciences **51**, 191 (2013).

[102] R. Feidenhans'l, *Surface Structure Determination by X-Ray Diffraction*, Surf Sci Rep **10**, 105 (1989).

[103] M. Björck and G. Andersson, *GenX: An Extensible X-Ray Reflectivity Refinement Program Utilizing Differential Evolution*, J Appl Crystallogr **40**, 1174 (2007).

[104] N. Kemik et al., *Resonant X-Ray Reflectivity Study of Perovskite Oxide Superlattices*, Appl Phys Lett **99**, 201908 (2011).

[105] *NIST X-Ray Form Factor, Attenuation and Scattering Tables Form Page*, https://physics.nist.gov/PhysRefData/FFast/html/form.html.

[106] *Scattering Length Density: GISAXS*, http://gisaxs.com/index.php/Scattering_Length_Density.

[107] D. D. Le Pevelen, *Small Molecule X-Ray Crystallography, Theory and Workflow*, in *Encyclopedia of Spectroscopy and Spectrometry, Second Edition*, edited by J. C. Lindon (Elsevier Ltd, 2010), pp. 2559–2576.

[108] D. Fuchs, E. Arac, C. Pinta, S. Schuppler, R. Schneider, and H. V. Löhneysen, *Tuning the Magnetic Properties of $LaCoO_3$ Thin Films by Epitaxial Strain*, Phys Rev B **77**, 014434 (2008).

[109] M. Losurdo, A. Sacchetti, P. Capezzuto, G. Bruno, L. Armelao, D. Barreca, G. Bottaro, A. Gasparotto, C. Maragno, and E. Tondello, *Optical and Electrical Properties of Nanostructured $LaCoO_3$ Thin Films*, Appl Phys Lett **87**, 061909 (2005).

[110] C. Adamo et al., *Effect of Biaxial Strain on the Electrical and Magnetic Properties of (001) $La_{0.7}Sr_{0.3}MnO_3$ Thin Films*, Appl Phys Lett **95**, 112504 (2009).

[111] T. Konya, *X-Ray Thin-Film Measurement Techniques III. High Resolution X-Ray Diffractometry*, The Rigaku Journal **25**, 1 (2009).

[112] B. D. Cullity and C. D. Graham, *Introduction to Magnetic Materials* (Wiley-IEEE Press, 2011).

[113] N. J. Jones, A Study of the Oxidation of $Fe_{1-x}Co_x$ Alloys and Their Resulting Magnetic Properties, Doctoral thesis, Doctoral thesis, Carnegie Mellon University, Pittsburgh, Pennsylvania, 2011.

[114] A. A. Ramadan, R. D. Gould, and A. Ashour, *On the Van Der Pauw Method of Resistivity Measurements*, Thin Solid Films **239**, 272 (1994).

[115] M. Merz, P. Nagel, C. Pinta, A. Samartsev, H. V. Löhneysen, M. Wissinger, S. Uebe, A. Assmann, D. Fuchs, and S. Schuppler, *X-Ray Absorption and Magnetic Circular Dichroism of $LaCoO_3$, $La_{0.7}Ce_{0.3}CoO_3$, and $La_{0.7}Co_{0.3}CoO_3$ Films: Evidence for Cobalt-Valence-Dependent Magnetism*, Phys Rev B **82**, 174416 (2010).

[116] A. Ruosi, C. Raisch, A. Verna, R. Werner, B. A. Davidson, J. Fujii, R. Kleiner, and D. Koelle, *Electron Sampling Depth and Saturation Effects in Perovskite Films Investigated by Soft X-Ray Absorption Spectroscopy*, Phys Rev B **90**, 125120 (2014).

[117] A. Bianconi, D. Jackson, and K. Monahan, *Intrinsic Luminescence Excitation Spectrum and Extended X-Ray Absorption Fine Structure above the K Edge in CaF_2*, Phys Rev B **17**, 2021 (1978).

[118] Atenderholt, *XASEdges*, https://en.wikipedia.org/wiki/X-ray_absorption_spectroscopy#/media/File:XASEdges.svg.

[119] G. van der Laan and A. I. Figueroa, *X-Ray Magnetic Circular Dichroism - A Versatile Tool to Study Magnetism*, Coord Chem Rev **277–278**, 95 (2014).

[120] C. Aruta, G. Ghiringhelli, V. Bisogni, L. Braicovich, N. B. Brookes, A. Tebano, and G. Balestrino, *Orbital Occupation, Atomic Moments, and Magnetic Ordering at Interfaces of Manganite Thin Films*, Phys Rev B **80**, 014431 (2009).

[121] D. Pesquera, G. Herranz, A. Barla, E. Pellegrin, F. Bondino, E. Magnano, F. Sánchez, and J. Fontcuberta, *Surface Symmetry-Breaking and Strain Effects on Orbital Occupancy in Transition Metal Perovskite Epitaxial Films*, Nat Commun **3**, 1189 (2012).

[122] B. Cui, C. Song, G. A. Gehring, F. Li, G. Wang, C. Chen, J. Peng, H. Mao, F. Zeng, and F. Pan, *Electrical Manipulation of Orbital Occupancy and Magnetic Anisotropy in Manganites*, Adv Funct Mater **25**, 864 (2015).

[123] S. Gariglio, M. Gabay, and J. M. Triscone, *Research Update: Conductivity and beyond at the $LaAlO_3/SrTiO_3$ Interface*, APL Materials.

[124] A. J. Millis, T. Darling, and A. Migliori, *Quantifying Strain Dependence in "Colossal" Magnetoresistance Manganites*, J Appl Phys **83**, 1588 (1998).

[125] M. Imada, A. Fujimori, and Y. Tokura, *Metal-Insulator Transitions*, Rev Mod Phys **70**, 1039 (1998).

[126] P. Zubko, S. Gariglio, M. Gabay, P. Ghosez, and J.-M. Triscone, *Interface Physics in Complex Oxide Heterostructures*, Annu Rev Condens Matter Phys **2**, 141 (2011).

[127] M. D. Biegalski et al., *Interrelation between Structure - Magnetic Properties in $La_{0.5}Sr_{0.5}CoO_3$*, Adv Mater Interfaces 1400203 (2014).

[128] J. Walter, S. Bose, M. Cabero, G. Yu, M. Greven, M. Varela, and C. Leighton, *Perpendicular Magnetic Anisotropy via Strain-Engineered Oxygen Vacancy Ordering in Epitaxial $La_{1-x}Sr_xCoO_{3-\delta}$*, Phys Rev Mater **2**, 111404(R) (2018).

[129] D. Kan, R. Aso, R. Sato, M. Haruta, H. Kurata, and Y. Shimakawa, *Tuning Magnetic Anisotropy by Interfacially Engineering the Oxygen Coordination Environment in a Transition Metal Oxide*, Nat Mater **15**, 432 (2016).

[130] A. M. Glazer, *The Classification of Tilted Octahedra in Perovskites*, Acta Crystallogr **28**, 3384 (1972).

[131] C. Xie, J. I. Budnick, B. O. Wells, and J. C. Woicik, *Separation of the Strain and Finite Size Effect on the Ferromagnetic Properties of $La_{0.5}Sr_{0.5}CoO_3$ Thin Films*, Appl Phys Lett **91**, 172509 (2007).

[132] L. Vasylechko, L. Akselrud, W. Morgenroth, U. Bismayer, A. Matkovskii, and D. Savytskii, *Crystal Structure of $NdGaO_3$ at 100 K and 293 K Based on Synchrotron Data*, J Alloys Compd **297**, 46 (2000).

[133] T. T. Fister et al., *Octahedral Rotations in Strained $LaAlO_3/SrTiO_3$ (001) Heterostructures*, APL Mater **2**, 021102 (2014).

[134] I. Hallsteinsen et al., *Concurrent Magnetic and Structural Reconstructions at the Interface of (111)-Oriented $La_{0.7}Sr_{0.3}MnO_3/LaFeO_3$*, Phys Rev B **94**, 201115 (2016).

[135] A. Ulyanenkov, *LEPTOS: A Universal Software for x-Ray Reflectivity and Diffraction*, in *Proc. SPIE*, Vol. 5536 (SPIE, 2004).

[136] A. R. Dzhanoev, F. Spahn, V. Yaroshenko, H. Lühr, and J. Schmidt, *Secondary Electron Emission from Surfaces with Small Structure*, Phys Rev B **92**, 125430 (2015).

[137] E. Arenholz, Private Communication.

[138] C. H. Kim, J. W. Jang, S. Y. Cho, I. T. Kim, and K. S. Hong, *Ferroelastic Twins in $LaAlO_3$ Polycrystals*, Physica B **262**, 438 (1999).

[139] J. Z. Sun, D. W. Abraham, R. A. Rao, and C. B. Eom, *Thickness-Dependent Magnetotransport in Ultrathin Manganite Films*, Appl Phys Lett **74**, 3017 (1999).

[140] J. Z. Sun, D. W. Abraham, R. A. Rao, and C. B. Eom, *Thickness-Dependent Magnetotransport in Ultrathin Manganite Films*, Appl Phys Lett **74**, 3017 (1999).

[141] R. V. Chopdekar, V. K. Malik, A. M. Kane, A. Mehta, E. Arenholz, and Y. Takamura, *Engineered Superlattices with Crossover from Decoupled to Synthetic Ferromagnetic Behavior*, Journal of Physics Condensed Matter **30**, 015805 (2018).

[142] M. Korotin, S. Y. Ezhov, I. Solovyev, V. Anisimov, D. Khomskii, and G. Sawatzky, *Intermediate-Spin State and Properties of $LaCoO_3$*, Phys Rev B **54**, 5309 (1996).

[143] J. Gazquez, S. Bose, M. Sharma, M. A. Torija, S. J. Pennycook, C. Leighton, and M. Varela, *Lattice Mismatch Accommodation via Oxygen Vacancy Ordering in Epitaxial $La_{0.5}Sr_{0.5}CoO_{3-\delta}$ Thin Films*, APL Mater **1**, 012105 (2013).

[144] M. Sharma, J. Gazquez, M. Varela, J. Schmitt, and C. Leighton, *Coercivity Enhancement Driven by Interfacial Magnetic Phase Separation in $SrTiO_3(001)/Nd_{0.5}Sr_{0.5}CoO_3$*, Phys Rev B **84**, 024417 (2011).

[145] G. Shibata et al., *Thickness-Dependent Ferromagnetic Metal to Paramagnetic Insulator Transition in $La_{0.6}Sr_{0.4}MnO_3$ Thin Films Studied by x-Ray Magnetic Circular Dichroism*, Phys Rev B **89**, 235123 (2014).

[146] B. Cui, C. Song, F. Li, G. Y. Wang, H. J. Mao, J. J. Peng, F. Zeng, and F. Pan, *Tuning the Entanglement between Orbital Reconstruction and Charge Transfer at a Film Surface*, Sci Rep **4**, 4206 (2014).

[147] X. Rui and R. F. Klie, *Atomic-Resolution in-Situ Cooling Study of Oxygen Vacancy Ordering in $La_{0.5}Sr_{0.5}CoO_{3-\delta}$ Thin Films*, Appl Phys Lett **114**, 233101 (2019).

[148] E. E. Fullerton, J. Jiang, M. Grimsditch, C. Sowers, and S. Bader, *Exchange-Spring Behavior in Epitaxial Hard/Soft Magnetic Bilayers*, Phys Rev B **58**, 12193 (1998).

[149] J. Zhang et al., *Magnetic Anisotropy Controlled by Distinct Interfacial Lattice Distortions at the $La_{1-x}Sr_xCoO_3/La_{2/3}Sr_{1/3}MnO_3$ Interfaces*, ACS Appl Mater Interfaces **10**, 40951 (2018).

[150] P. Chen et al., *Enhanced Magnetic Anisotropy and Orbital Symmetry Breaking in Manganite Heterostructures*, Adv Funct Mater **30**, 1909536 (2020).

[151] J. Song et al., *Electric Tuning of Magnetic Anisotropy and Exchange Bias of $La_{0.8}Sr_{0.2}CoO_3/La_{0.67}Sr_{0.33}MnO_3$ Bilayer Films*, Phys Rev Appl **14**, 024062 (2020).

[152] H. Boschker, M. Mathews, E. P. Houwman, H. Nishikawa, A. Vailionis, G. Koster, G. Rijnders, and D. H. A. Blank, *Strong Uniaxial In-Plane Magnetic Anisotropy of (001)- and (011)-Oriented $La_{0.67}Sr_{0.33}MnO_3$ Thin Films on $NdGaO_3$ Substrates*, Phys Rev B **79**, 214425 (2009).

[153] M. Feng, N. J. Ahlm, A. M. Kane, I.-T. Chiu, D. Y. Sasaki, P. Shafer, A. T. N'Diaye, A. Mehta, and Y. Takamura, *Strain- and Thickness-Dependent Magnetic Properties of Epitaxial $La_{0.67}Sr_{0.33}CoO_3/La_{0.67}Sr_{0.33}MnO_3$ Bilayers*, J Appl Phys **132**, 195301 (2022).

[154] A. Y. Zuev and D. S. Tsvetkov, *Oxygen Nonstoichiometry, Defect Structure and Defect-Induced Expansion of Undoped Perovskite $LaMnO_{3\pm\delta}$*, Solid State Ion **181**, 557 (2010).

[155] A. Y. Zuev, A. I. Vylkov, A. N. Petrov, and D. S. Tsvetkov, *Defect Structure and Defect-Induced Expansion of Undoped Oxygen Deficient Perovskite $LaCoO_{3-\delta}$*, Solid State Ion **179**, 1876 (2008).

[156] C. T. Shannon, R. D.; Prewitt, *Effective Ionic Radii in Oxides and Fluorides*, Acta Cryst **B25**, 925 (1969).

[157] R. D. Shannon, *Revised Effective Ionic Radii and Systematic Studies of Interatomic Distances in Halides and Chalcogenides*, Acta Cryst. **A32**, 751 (1976).

[158] A. Vailionis, H. Boschker, W. Siemons, E. P. Houwman, D. H. A. Blank, G. Rijnders, and G. Koster, *Misfit Strain Accommodation in Epitaxial ABO_3 Perovskites: Lattice Rotations and Lattice Modulations*, Phys Rev B **83**, 064101 (2011).

[159] C. L. Jia, S. B. Mi, M. Faley, U. Poppe, J. Schubert, and K. Urban, *Oxygen Octahedron Reconstruction in the $SrTiO_3/LaAlO_3$ Heterointerfaces Investigated Using Aberration-Corrected Ultrahigh-Resolution Transmission Electron Microscopy*, Phys Rev B **79**, 081405(R) (2009).

[160] V. K. Malik, C. Hieu Vo, E. Arenholz, A. Scholl, A. T. Young, and Y. Takamura, *Magnetic Correlation between $La_{0.7}Sr_{0.3}MnO_3$ and $La_{0.7}Sr_{0.3}CoO_3$ Layers in Artificial Superlattices*, J Appl Phys **113**, 153907 (2013).

[161] A. C. Basaran, C. Monton, J. Trastoy, R. Bernard, K. Bouzehouane, J. E. Villegas, and I. K. Schuller, *Emergence of Exchange Bias and Giant Coercive Field Enhancement by Internal Magnetic Frustration in $La_{0.67}Sr_{0.33}MnO_3$ Thin Films*, J Magn Magn Mater **550**, 169077 (2022).

[162] L. Zhang et al., *Proximity-Coupling-Induced Significant Enhancement of Coercive Field and Curie Temperature in 2D van Der Waals Heterostructures*, Advanced Materials **32**, 2002032 (2020).

[163] Y. J. Shi, Y. Zhou, H. F. Ding, F. M. Zhang, L. Pi, Y. H. Zhang, and D. Wu, *Exchange Bias Coupling of Co with Ultrathin $La_{2/3}Sr_{1/3}MnO_3$ Films*, Appl Phys Lett **101**, 122409 (2012).

[164] C. L. Prajapat et al., *Interface-Induced Magnetization and Exchange Bias in LSMO/BFO Multiferroic Heterostructures*, ACS Appl Electron Mater **2**, 2629 (2020).

[165] C. Leighton, J. Nogués, B. J. Jönsson-Åkerman, and I. K. Schuller, *Coercivity Enhancement in Exchange Biased Systems Driven by Interfacial Magnetic Frustration*, Phys Rev Lett **84**, 3466 (2000).

[166] F. Han et al., *Spin Reorientation at (110)-$La_{2/3}Sr_{1/3}MnO_3/LaCoO_3$ Interfaces by Orbital/Charge Reconstruction*, APL Mater **8**, 021113 (2020).

[167] G. Van Der Laan, B. T. Thole, G. A. Sawatzky, J. B. Goedkoop, J. C. Fuggle, J. M. Esteva, R. Karnatak, J. P. Remeika, and H. A. Dabkowska, *Experimental Proof of Magnetic X-Ray Dichroism*, Phys Rev B **34**, 6529 (1986).

[168] V. R. Nallagatla et al., *Topotactic Phase Transition Driving Memristive Behavior*, Advanced Materials **31**, 1903391 (2019).

[169] S. Zhang and G. Galli, *Understanding the Metal-to-Insulator Transition in $La_{1-x}Sr_xCoO_{3-\delta}$ and Its Applications for Neuromorphic Computing*, NPJ Comput Mater **6**, 170 (2020).

[170] D. Yi et al., *Emergent Electric Field Control of Phase Transformation in Oxide Superlattices*, Nat Commun **11**, 902 (2020).

[171] M. H. Lee, Y. Kalcheim, J. Del Valle, and I. K. Schuller, *Controlling Metal-Insulator Transitions in Vanadium Oxide Thin Films by Modifying Oxygen Stoichiometry*, ACS Appl Mater Interfaces **13**, 887 (2021).

[172] T. G. Parsons, H. D'Hondt, J. Hadermann, and M. A. Hayward, *Synthesis and Structural Characterization of $La_{1-x}A_xMnO_{2.5}$(A = Ba, Sr, Ca) Phases: Mapping the Variants of the Brownmillerite Structure*, Chemistry of Materials **21**, 5527 (2009).

[173] J. Zhang et al., *Symmetry Mismatch-Driven Perpendicular Magnetic Anisotropy for Perovskite/Brownmillerite Heterostructures*, Nat Commun **9**, 1923 (2018).

[174] S. Madhukar, S. Aggarwal, A. M. Dhote, R. Ramesh, A. Krishnan, D. Keeble, and E. Poindexter, *Effect of Oxygen Stoichiometry on the Electrical Properties of $La_{0.5}Sr_{0.5}CoO_3$ Electrodes*, J Appl Phys **81**, 3543 (1997).

[175] H. Jeen, W. S. Choi, J. W. Freeland, H. Ohta, C. U. Jung, and H. N. Lee, *Topotactic Phase Transformation of the Brownmillerite $SrCoO_{2.5}$ to the Perovskite $SrCoO_{3-\delta}$*, Advanced Materials **25**, 3651 (2013).

[176] S. D. Taylor et al., *Resolving Diverse Oxygen Transport Pathways Across Sr-Doped Lanthanum Ferrite and Metal-Perovskite Heterostructures*, Adv Mater Interfaces **10**, 2202276 (2023).

[177] D. O. Klenov, W. Donner, B. Foran, and S. Stemmer, *Impact of Stress on Oxygen Vacancy Ordering in Epitaxial $(La_{0.5}Sr_{0.5})CoO_{3-\delta}$ Thin Films*, Appl Phys Lett **82**, 3427 (2003).

[178] L. Yao, S. Inkinen, and S. Van Dijken, *Direct Observation of Oxygen Vacancy-Driven Structural and Resistive Phase Transitions in $La_{2/3}Sr_{1/3}MnO_3$*, Nat Commun **8**, 14544 (2017).

[179] Q. Lu and B. Yildiz, *Voltage-Controlled Topotactic Phase Transition in Thin-Film $SrCoO_x$ Monitored by in Situ X-Ray Diffraction*, Nano Lett **16**, 1186 (2016).

[180] H. Han et al., *Control of Oxygen Vacancy Ordering in Brownmillerite Thin Films via Ionic Liquid Gating*, ACS Nano **16**, 6206 (2022).

[181] A. Adlie Shamsuri and D. Kuang Abdullah, *IONIC LIQUIDS: PREPARATIONS AND LIMITATIONS*, Makara J Sci **14**, 101 (2010).

[182] C. Leighton, T. Birol, and J. Walter, *What Controls Electrostatic vs Electrochemical Response in Electrolyte-Gated Materials? A Perspective on Critical Materials Factors*, APL Mater **10**, 040901 (2022).

[183] D. Kim, Y. Jeon, J. L. MacManus-Driscoll, and S. Lee, *Solid-State Catalytic Hydrogen Sponge Effects in $BaInO_{2.5}$ Epitaxial Films*, Adv Funct Mater **33**, 2300819 (2023).

[184] H. Jani et al., *Reversible Hydrogen Control of Antiferromagnetic Anisotropy in α-Fe_2O_3*, Nat Commun **12**, 1668 (2021).

[185] A. R. Mazza et al., *Reversible Hydrogen-Induced Phase Transformations in $La_{0.7}Sr_{0.3}MnO_3$ Thin Films Characterized by in Situ Neutron Reflectometry*, ACS Appl Mater Interfaces **14**, 10898 (2022).

[186] J. Lee, Y. Ha, and S. Lee, *Hydrogen Control of Double Exchange Interaction in $La_{0.67}Sr_{0.33}MnO_3$ for Ionic–Electric–Magnetic Coupled Applications*, Advanced Materials **33**, 2007606 (2021).

[187] M. A. Hayward, E. J. Cussen, J. B. Claridge, M. Bieringer, M. J. Rosseinsky, C. J. Kiely, S. J. Blundell, I. M. Marshall, and F. L. Pratt, *The Hydride Anion in an Extended Transition Metal Oxide Array: $LaSrCoO_3H_{0.7}$*, Science **295**, 1882 (2002).

[188] J. Shi, Y. Zhou, and S. Ramanathan, *Colossal Resistance Switching and Band Gap Modulation in a Perovskite Nickelate by Electron Doping*, Nat Commun **5**, 4860 (2014).

[189] Y. Bian, H. Li, F. Yan, H. Li, J. Wang, H. Zhang, Y. Jiang, N. Chen, and J. Chen, *Hydrogen Induced Electronic Transition within Correlated Perovskite Nickelates with Heavy Rare-Earth Composition*, Appl Phys Lett **120**, 092103 (2022).

[190] S. Chowdhury, R. J. Choudhary, and D. M. Phase, *Time Evolution of the Structural, Electronic, and Magnetic Phases in Relaxed $SrCoO_3$ Thin Films*, ACS Appl Electron Mater **3**, 5095 (2021).

[191] H. Jeen et al., *Reversible Redox Reactions in an Epitaxially Stabilized $SrCoO_x$ Oxygen Sponge*, Nat Mater **12**, 1057 (2013).

[192] G. Rippy et al., *X-Ray Nanodiffraction Studies of Ionically Controlled Nanoscale Phase Separation in Cobaltites*, Phys Rev Mater **3**, 082001 (2019).

[193] Y. P. Ivanov, M. Kubicek, M. Siebenhofer, A. Viernstein, H. Hutter, J. Fleig, A. Chuvilin, and Z. Zhang, *Strain-Induced Structure and Oxygen Transport Interactions in Epitaxial $La_{0.6}Sr_{0.4}CoO_{3-\delta}$ Thin Films*, Commun Mater **1**, 25 (2020).

[194] A. R. Dzhanoev, F. Spahn, V. Yaroshenko, H. Lühr, and J. Schmidt, *Secondary Electron Emission from Surfaces with Small Structure*, Phys Rev B **92**, 125430 (2015).

[195] A. Bianconi, D. Jackson, and K. Monahan, *Intrinsic Luminescence Excitation Spectrum and Extended X-Ray Absorption Fine Structure above the K Edge in CaF_2*, Phys Rev B **17**, 2021 (1978).

[196] S. Czekaj, F. Nolting, L. J. Heyderman, P. R. Willmott, and G. Van Der Laan, *Sign Dependence of the X-Ray Magnetic Linear Dichroism on the Antiferromagnetic Spin Axis in $LaFeO_3$ Thin Films*, Phys Rev B **73**, 020401 (2006).

[197] M. Merz, P. Nagel, C. Pinta, A. Samartsev, H. V. Löhneysen, M. Wissinger, S. Uebe, A. Assmann, D. Fuchs, and S. Schuppler, *X-Ray Absorption and Magnetic Circular Dichroism of $LaCoO_3$, $La_{0.7}Ce_{0.3}CoO_3$, and $La_{0.7}Co_{0.3}CoO_3$ Films: Evidence for Cobalt-Valence-Dependent Magnetism*, Phys Rev B **82**, 174416 (2010).

[198] S. Zhang et al., *Determining the Oxygen Stoichiometry of Cobaltite Thin Films*, Chemistry of Materials **34**, 2076 (2022).

[199] N. Lu et al., *Enhanced Low-Temperature Proton Conductivity in Hydrogen-Intercalated Brownmillerite Oxide*, Nat Energy **7**, 1208 (2022).

[200] C. J. Howard and H. T. Stokes, *Structures and Phase Transitions in Perovskites - a Group-Theoretical Approach*, Acta Crystallogr **A61**, 93 (2005).

[201] W. Zhang, J. Zhang, S. Cheng, C. M. Rouleau, K. Kisslinger, L. Zhang, Y. Zhu, T. Z. Ward, and G. Eres, *Exploring the Spatial Control of Topotactic Phase Transitions Using Vertically Oriented Epitaxial Interfaces*, Nanomicro Lett **14**, 2 (2022).

[202] V. V. Kharton, E. N. Naumovich, A. A. Vecher, and A. V. Nikolaev, *Oxide Ion Conduction in Solid Solutions $Ln_{1-x}Sr_xCoO_{3-\delta}$(Ln = La, Pr, Nd)*, J Solid State Chem **120**, 128 (1995).

[203] L. Cao, O. Petracic, P. Zakalek, A. Weber, U. Rücker, J. Schubert, A. Koutsioubas, S. Mattauch, and T. Brückel, *Reversible Control of Physical Properties via an Oxygen-Vacancy-Driven Topotactic Transition in Epitaxial $La_{0.7}Sr_{0.3}MnO_{3-\delta}$ Thin Films*, Advanced Materials **31**, 1806183 (2019).

[204] M. A. Islam, Y. Xie, M. D. Scafetta, S. J. May, and J. E. Spanier, *Raman Scattering in $La_{1-x}Sr_xFeO_{3-\delta}$ Thin Films: Annealing-Induced Reduction and Phase Transformation*, Journal of Physics Condensed Matter **27**, 155401 (2015).

[205] Y. Liu, S. Hu, B. Zhao, X. Shi, X. Zeng, C. W. Leung, and C. Huang, *Comparison of Topotactic and Magnetic Structures for Manganite Oxide Films*, Ceram Int **48**, 12515 (2022).

[206] V. V. Kharton, A. V. Kovalevsky, M. V. Patrakeev, E. V. Tsipis, A. P. Viskup, V. A. Kolotygin, A. A. Yaremchenko, A. L. Shaula, E. A. Kiselev, and J. C. Waerenborgh, *Oxygen Nonstoichiometry, Mixed Conductivity, and Mössbauer Spectra of $Ln_{0.5}A_{0.5}FeO_{3-\delta}$ (Ln = La-Sm, A = Sr, Ba): Effects of Cation Size*, Chemistry of Materials **20**, 6457 (2008).

[207] C. A. F. Vaz, J. A. C. Bland, and G. Lauhoff, *Magnetism in Ultrathin Film Structures*, Rep. Prog. Phys **71**, 056501 (2008).

[208] M. Huijben, L. W. Martin, Y.-H. Chu, M. B. Holcomb, P. Yu, G. Rijnders, D. H. A. Blank, and R. Ramesh, *Critical Thickness and Orbital Ordering in Ultrathin $La_{0.7}Sr_{0.3}MnO_3$ Films*, Phys Rev B **78**, 094413 (2008).

[209] R. V Chopdekar, J. Heidler, C. Piamonteze, Y. Takamura, A. Scholl, S. Rusponi, H. Brune, L. J. Heyderman, and F. Nolting, *Strain-Dependent Magnetic Configurations in Manganite-Titanate Heterostructures Probed with Soft X-Ray Techniques*, Eur. Phys. J. B **86**, 241 (2013).

[210] K. Tae Kang, B. Zhang, Y. Sharma, B. Paudel, H. Wang, P. Dowden, and A. Chen, *Substrate Oxygen Sponge Effect: A Parameter for Epitaxial Manganite Thin Film Growth*, Appl. Phys. Lett **117**, 151601 (2020).

[211] B. J. Sternlieb, J. P. Hill, U. C. Wildgruber, G. M. Luke, B. Nachumi, Y. Moritomo, and Y. Tokura, *Charge and Magnetic Order in $La_{0.5}Sr_{1.5}MnO_4$*, Phys. Rev. Lett. **76**, 2169 (1996).

[212] Y. Moritomo, Y. Tomioka, A. Asamitsu, Y. Tokura, and Y. Matsui, *Magnetic and Electronic Properties in Hole-Doped Manganese Oxides with Layered Structures: $La_{1-x}Sr_{1+x}MnO_4$*, Phys Rev B **51**, 3297 (1995).

[213] J. F. Mitchell, D. N. Argyriou, A. Berger, K. E. Gray, R. Osborn, and U. Welp, *Spin, Charge, and Lattice States in Layered Magnetoresistive Oxides*, Journal of Physical Chemistry B **105**, 10731 (2001).

[214] Y. Takamura, F. Yang, N. Kemik, E. Arenholz, M. D. Biegalski, and H. M. Christen, *Competing Interactions in Ferromagnetic/Antiferromagnetic Perovskite Superlattices*, Phys Rev B **80**, 180417(R) (2009).

[215] R. A. Gunasekaran, J. D. Pedarnig, and M. Dinescu, *Structural, Electrical, and Surface Characteristics of $La_{0.5}Sr_{0.5}CoO_3$ Thin Films Prepared by Pulsed-Laser Deposition*, Applied Physics A **69**, 621 (1999).

[216] X. Chen, S. Wang, Y. L. Yang, L. Smith, N. J. Wu, B. I. Kim, S. S. Perry, A. J. Jacobson, and A. Ignatiev, *Electrical Conductivity Relaxation Studies of an Epitaxial $La_{0.5}Sr_{0.5}CoO_{3-\delta}$ Thin Film*, Solid State Ion **146**, 405 (2002).

[217] C. Wang, J. Qi, J. Li, F. Wang, Y. Zhang, H. Xu, L. Hu, M. Feng, and W. Lü, *The Modulated Oxygen Evolution Reaction Performance in $La_{2/3}Sr_{1/3}CoO_3$ by a Design of Stoichiometry Offset*, Journal of Electroanalytical Chemistry **911**, 116235 (2022).

[218] H. Kersell, M. L. Weber, L. Falling, Q. Lu, C. Baeumer, N. Shirato, V. Rose, C. Lenser, F. Gunkel, and S. Nemšák, *Evolution of Surface and Sub-Surface Morphology and Chemical State of Exsolved Ni Nanoparticles*, Faraday Discuss **236**, 141 (2022).

[219] K. Hu, X. Zhang, P. Chen, R. Lin, J. Zhu, Z. Huang, H. Du, D. Song, and B. Ge, *Atomic-Scale Observation of Strain-Dependent Reversible Topotactic Transition in $La_{0.7}Sr_{0.3}MnO_x$ Films under an Ultra-High Vacuum Environment*, Materials Today Physics **29**, 100922 (2022).